International Committee for Future Accelerators

Sponsored by the Particles and Fields Commission of IUPAP

Beam Dynamics Newsletter

No. 61

Issue Editor:
T. Okugi

Editor in Chief:
W. Chou

August 2013

Contents

4

1   Foreword

1.1   From the Chairman

Weiren Chou, Fermilab
Mail to: chou@fnal.gov

Over the past several months, important mid- and long-term studies of the HEP program took place in each of the major HEP regions and countries around the world.

- On the 30th of May the CERN Council approved the *European Strategy for Particle Physics,* which listed four high priority projects: LHC, high-energy *pp* and e^+e colliders, ILC and long baseline neutrino experiments.
 (http://council.web.cern.ch/council/en/EuropeanStrategy/ESParticlePhysics.html)

- From the 29th of July to the 6th of August, the US HEP community carried out a Community Summer Study, *Snowmass2013,* a comprehensive discussion of the greatest unsolved mysteries of matter, energy, space and time as well as the facilities and experiments that would help solve them. However, the Snowmass meeting did not set priorities. This will be the job for the P5 Committee being formed by the DOE and NSF and which will be chaired by Professor Steve Ritz of UC Santa Cruz. The P5 report is expected in the spring of 2014. (http://www.snowmass2013.org/tiki-index.php)

- As Japan is a serious candidate (and the only one) to host the ILC, the Science Council of Japan was asked by the Japanese government to give advice on this project. According to a Nikkei report on the 12th of August: "*The committee under the Science Council of Japan, which discussed the significance of the ILC, framed their response on 12 August that the project should be examined further over a few years. The Ministry of Science, Education, Sports and Technology will take this recommendation into account, but retains the positive attitude toward invitation*."
 (http://www.nikkei.com/article/DGXNASGG1201O_S3A810C1TJM000/)

- On the 23rd of August a site selection panel in Japan announced the Kitakami mountain area in the Tohoku region in northeastern Japan has been chosen as a candidate site for hosting the ILC.

- From the 12th to 14th of June, the China HEP community had a Fragrant Hill Science Conference. It concluded that the next-generation electron-positron collider, a so-called "Higgs factory," would be a significant historical opportunity for the development of China's high-energy physics program. (http://newsline.linearcollider.org/2013/06/27/chinas-strategy-on-next-generation-high-energy-electron-positron-colliders-discussed/)

All these studies will have a profound impact on the world HEP program in the coming decades. In particular, Japan's decision on whether or not it will host the construction of the ILC will be significant, because this decision plays a big role in the strategic plans of Europe, the US and China.

The collaboration between the two international communities, ICFA (for accelerators) and ICUIL (for lasers) continues to make progress. A recent IZEST workshop (https://lasers.llnl.gov/workshops/izest/index.php) at the Lawrence Livermore

National Laboratory reported tremendous and rapid improvement in laser technology in order to meet the needs of particle accelerators. For example, a breakthrough in fiber laser technology showed that by using a coherent amplification network, the fiber laser can deliver a pulse with an energy of ~10 J at a repetition rate of ~10 kHz. Such a laser system can be directly applied to a $\gamma\gamma$ collider and bring this novel type of particle collider from fantasy to reality. Further discussions on applying this laser technology for colliders are in progress.

At the ICFA meeting on the 26th of June in San Francisco, the *54th ICFA Advanced Beam Dynamics Workshop on High Intensity High Brightness Hadron Beams* (HB2014) was approved. It will be hosted by Michigan State University, USA, November 10 – 14, 2014.

The application process for attending *The Eighth International Accelerator School for Linear Colliders* has begun. (http://www.linearcollider.org/school/2013/) The school will take place from December 4 to 15, at Hotel Rixos Downtown, Antalya, Turkey, and be hosted by the Institute of Accelerator Technologies (IAT) of Ankara University. The school program and a list of lecturers can be found in Section 5.1.

The Editor of this issue is Dr. Toshiyuki Okugi, a panel member and an accelerator scientist at KEK, Japan. Toshiyuki selected the theme of "*Final focus systems for linear colliders*" and has five topics on this theme. Each topic consists of several sub-topics and each sub-topic was authored by well-known experts in their respective field. These articles together give a comprehensive overview of this important accelerator field, which plays a critical role in both the ILC and CLIC, two major candidates for a future energy frontier collider.

In this issue there are three workshop reports (BB2013, SC2013, 5th Microbunching Instability), five workshop announcements (3rd Low Emittance Ring, FFAG2013, IBIC2013, NAPAC2013 and Commissioning of SuperKEKB and e^+e Colliders), and two doctoral thesis abstract (James Maloney, NIU, USA; Maja Olvegard, Uppsala U., Sweden). I thank Toshiyuki for editing and producing a newsletter of great value and high quality for our community.

1.2   From the Editor

Toshiyuki Okugi, KEK
Mail to: toshiyuki.okugi@kek.jp

There were two major activities for the Linear Colliders in 2013. The first activity was the completion by the Global Design Effort (GDE) of the Technical Design Report of ILC (TDR). The second activity was to start the new Linear Collider Collaboration (LCC) after the GDE completed the TDR. The LCC collaboration united ILC and CLIC. Therefore, I have selected the final focus system for the linear collider as a special theme topic for this 61st Issue of the Beam Dynamics Newsletter. This is related to ILC and CLIC, because both the final focus beamlines are based on the *local chromaticity correction scheme*. There are many interactions between the ILC and CLIC final focus systems through their optics design and the ATF2 experiment.

This edition of the newsletter reports the optics designs of ILC and CLIC final focus systems, the activity of ATF2, the intra–train feedback and the beam instrumentation for the final focus system.

The basic technique of the local chromaticity correction is reported by **Andrei Seryi**. The design of the final focus system for ILC and CLIC is reported by **Toshiaki Tauchi** and **Rogelio Tomas**. The ATF2 is a test facility for the ILC final focus beamline. The ATF2 beamline was constructed at the Accelerator Test Facility (ATF) in KEK. The ATF2 beam optics is also designed based on the local chromaticity correction scheme as are the ILC and CLIC final focus systems. The introduction of ATF is reported by **Shigeru Kuroda**. The optics design of the ATF2 final focus beamline is reported by **Glen White**. The optics parameters for the ILC and CLIC final focus systems are different, even though both designs are based on the local chromaticity correction scheme. The CLIC final focus aims at larger chromaticity and smaller β^* than in the ILC. The nominal parameters of the ATF2 final focus system are set to achieve almost the same chromaticity as the ILC final focus. However, we are investigating the possibility of testing the ultra-low β^* option as in the CLIC final focus system. This investigation is reported by **Eduardo Marin**. The demonstration of the final focus beamline at ATF2 is major importance not only to ILC, but also to CLIC.

We also report the beam tuning of the ATF2 beamline both for the injection to the final focus beamline and the beam size tuning at the virtual interaction point (IP). The present ATF2 activities of the injection to the final focus beamline is reported by **Mark Woodley**, and the IP beam size tuning is reported by **Toshiyuki Okugi**.

Furthermore, the wakefield effect at the ATF2 beamline is reported by **Kiyoshi Kubo**, **Alexey Lyapin** and **Jochem Snuverink**. The IP beam size growth was stronger than expected at the ATF2 beamline. One of the candidates for the beam size growth is the corrective effect by the kick of the transverse wakefield. Therefore, the effect of the wakefield is investigated at the ATF2 beamline. The wake field study has a possibility to affect the chamber design for the linear collider beamlines.

The intra-train IP position feedback is an important technique to achieve high luminosity at the linear colliders. The design and the present activities at the ATF2 beamline are reported by **Philip Burrows**. The beam instrumentation for the linear colliders also developed at the ATF2 beamline, the instrumentations are reported by **Stewart Boogert**, **Laurie Nevay** and **Angeles Faus-Golfe**.

I thank all the contributors for providing these excellent articles on the final focus system for linear colliders and hope they will communicate to you the present activities and problems for the final focus system of linear colliders.

2   Theme: Final Focus System for Linear Colliders

2.1   Beam Optics Design of the LC Final Focus System

Andrei Seryi

John Adams Institute for Accelerator Science, University of Oxford,
Royal Holloway University of London and Imperial College London, UK
Mail to: Andrei.Seryi@adams-instite.ac.uk

This review we will describe the recent experience of the beam size tuning at the ATF2 test facility, which is a prototype of the LC final focus system based on the principle of local chromaticity correction [1]. Recent operation resulted in achievement

of sufficiently small beam size demonstrating successful operation of the compact local chromaticity correction optics, and possibility for use of such optics for the International Linear Collider [2]. In this paper, after brief review of the ATF2 design, we will focus on description of the techniques and methods developed for tuning the beam size at the Interaction Point (IP) of ATF2.

2.1.1 Local Chromaticity Correction

The heart of the ATF2 optics is the final focus based on the principles of the local compensation of chromaticity [1] – the method which is adopted for the ILC FF design [2] and which is also the only practical method to focus multi-TeV beams – the CLIC Final Focus system is based on the same principle [3]. The block-scheme of the optics which is used for most of the recent designs of ILC FF as well as for the ATF2 design is shown in the Fig. 1 below. One need to note that this scheme is somewhat different than the initial design described in [1] and the difference will be described in the next paragraphs.
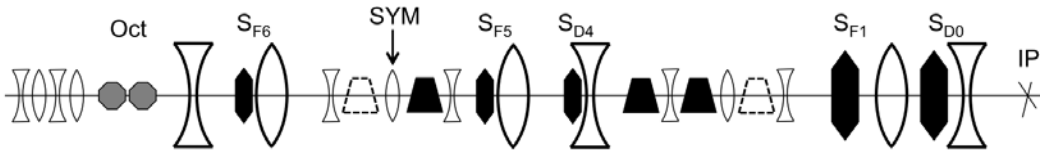
Figure 1: Schematics of a final focus system with local chromaticity correction. Part of the bends (shown by dashed line) as well as tail-folding octupoles (a pair of them is shown as gray octagons and denoted as "Oct" in the beginning of the line) were not included into the ATF2 optics implementation.

In the LC final focus system, the largest fraction of the chromaticity, produced in the final doublet, is compensated locally, by sextupoles placed in the FD (in Fig. 1 by sextupoles SD0 and SF1), in the region of nonzero dispersion, generated by the bends upstream of FD. The parasitic second order dispersion, which is unavoidably generated by the FD sextupoles, is cancelled together with x and y chromaticities by using a trick that an appropriate amount of horizontal chromaticity allowed to arrive from upstream of FD. The higher order aberrations are cancelled by additional sextupoles installed upstream of FD (in Fig. 1 by sextupoles SD4, SF5 and SF6). These design principles allowed to make the final focus system much shorter, and have much more beneficial scaling of its length with energy, which is especially important at close to TeV and multi-TeV energies. In details the principles of the local chromaticity correction and design of the ATF2 final focus system are described elsewhere (see in particular [1,4]). Here we would like to describe briefly the difference of this optics from the original one described in [1]. In the present version there is an additional functionality of the final focus, designed into the system – the so called tail-folding octupoles [6]. In order to create an optimal location for these octupoles, it was necessary to create a sufficient drift space with large beta-functions and in dispersion-free area, in-phase with the final doublet in both planes. Correspondingly, this condition resulted in some modification of the beginning part of the optics, with the geometric aberration correction section rearranged to be symmetrical with respect to the point denoted as "SYM" in Fig. 1. The

optimal drift for the tail-folding octupoles is then created upstream of the geometric aberration correction section.

We also would like to note that the design of ATF2 final focus was performed using the recipe and techniques described in [5] where iterative applications of linear and nonlinear knobs were used to gradually come to a well-performing optics design. As noted in [5], "in spite of the seeming tediousness of this approach to FF design, this method is almost directly applicable for tuning a real final focus during commissioning and operation". Below, we will review the methods of tuning the beam size the IP of ATF2 final focus, which involve iterative applications of linear and nonlinear knobs. This tuning cannot be performed without good diagnostics, which allowed to measure beam properties both at the IP and at key location along the beamline. Before describing the tuning procedure we therefore will follow in the next section with description of interferometer based beam-size monitor, as well as other diagnostic implemented in ATF2.

The principles of the local chromaticity correction were used in the design of final focus system for both ILC and CLIC. Detailed description of ILC and CLIC Beam Delivery and FF are given in the next sections.

2.1.1.1 *References*

1. P. Raimondi and A. Seryi, Phys. Rev. Lett., **86** 3779 (2001).
2. ILC Global Design Effort, "ILC Technical Design Report", http://www.linearcollider.org/ILC/Publications /Technical-Design-Report.
3. "CLIC Conceptual Design Report", CERN-2012-007.
4. ATF2 proposal, KEK-Report 2005- 2 (2005).
5. A.Seryi, M.Woodley and P.Raimondi, "A Recipe for Linear Collider Final Focus System Design", SLAC-PUB-9895, Presented at PAC-2003.
6. R.Brinkmann, (DESY), P. Raimondi, A. Seryi, (SLAC), "Halo Reduction by Means of Non Linear Optical Elements in the NLC Final Focus System", SLAC-PUB-8896, Presented at PAC-2001.

2.1.2 **ILC Beam Delivery System and Final Focus System**

Toshiaki Tauchi
High Energy Accelerator Research Organization (KEK), Japan
Mail to: toshiaki.tauchi@kek.jp

The International Linear Collider (ILC) is a 31km long e^+e^- collider with acceleration in superconducting cavities at the center of mass energy of 500 to 1000 GeV. The ILC Global Design Effort (GDE) has been established in order to design the ILC with international collaboration in 2005. The GDE published the technical design report (TDR) in June 2013[1]. Basic designs of all systems are described in details with the cost estimation in TDR. Bean delivery system (BDS) is the last part of ILC at the top energy, focusing to nanometer sizes for collisions with high luminosity. Final focus system is the main accelerator system in BDS. The key parameters of the BDS are listed in Table 1.

Table 1: Key parameters of the BDS [1]

Parameter	*Value*	**Unit**
Length (start to IP distance) per side	2254	m
Length of main (tune-up) extraction line	300(467)	m
Max. Energy/beam (with more magnets)	250(500)	GeV
Distance from IP to first quad, L* for SiD/ILD	3.51/4.5	m
Crossing angle at the IP	14	mrad
Normalized emittance $\gamma \varepsilon_x / \gamma \varepsilon_y$	10000/35	nm
Normal bunch length, σ_z	300	μ m
Preferred entrance train to train jitter	<0.2-0.5	σ_y
Preferred entrance bunch to bunch jitter	<0.1	σ_y
Typical nominal collimation aperture, x/y	6-10/30-60	beam sigma
Vacuum pressure level, near/far from IP	0.1/5	μ Pa

The BDS has total length of 4.5 km for electron and positron beams. It has been designed for a single interaction region (IR) allowing two experiments with push-pull scheme and also for upgradable to 1TeV center-of-mass (CM) energy in the same layout. Basic parameters are a distance from interaction point (IP) to first quadrupole magnet, L* of 3.51/4.5m for SiD/ILD detector concepts, horizontal crossing angle between two beams of 14mradian at IP, beam sizes at IP and the energy spread, σ_x/σ_y of 474/5.9nm and δ E/E (e-/e+) of 0.124/0.070%, respectively, for the nominal beam energy of 250GeV and the maximum beam power of 18 MW at 1 TeV CM.
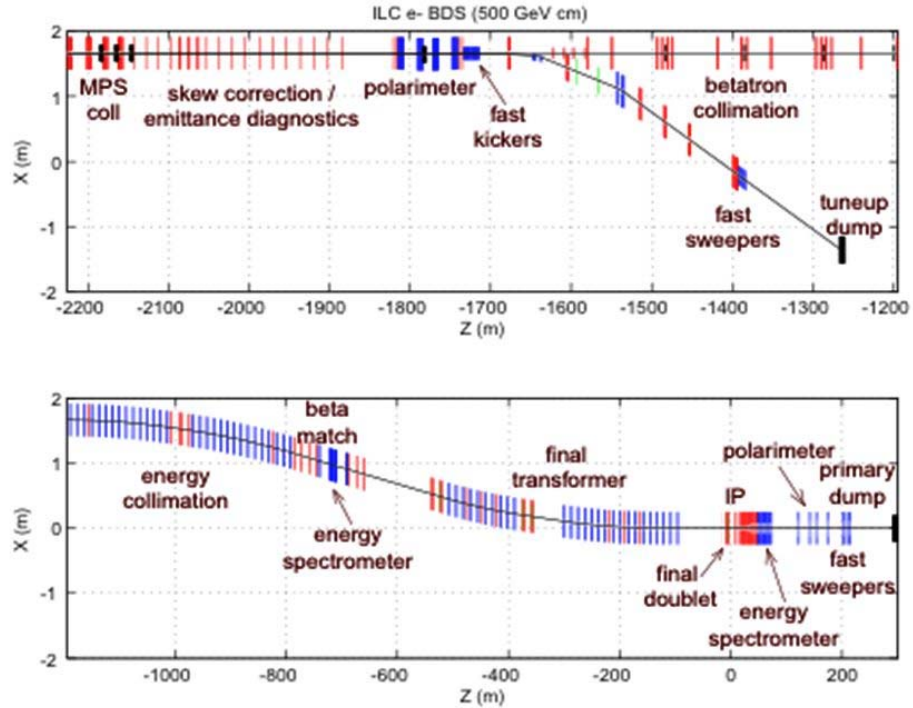
Figure 2 : Layout of BDS functional systems, X - horizontal position of elements and Z - distance measured from IP [1].

As shown in Fig. 2, the BDS consists of diagnostic section, polarimeter, fast kickers to extract beam to a tuneup dump, collimation section, final focus section and 300m long extraction line to the primary dump. First from the main LINAC, emittance and polarization of beam are measured and horizontal and vertical coupling is also corrected with so-called skew correction in the diagnostic section. The collimation section consists of betatron collimation in phase space and energy collimation, where typical collimation depths in beam halo are 8-10σ_x and 60σ_y , and the downstream energy collimator can remove the degrade energy particles originating from the betatron collimation. The depths can be changed by adjustable gaps. The collimation section is important to control synchrotron radiations in IR. During the collimation, many muons could be generated. In order to prevent muons from penetrating the detector, a muon wall is installed at 330m upstream from IP, which is a 5m long magnetized iron at 1.5T. In this scheme, the halo can be tolerable up to 10^{-3} of beam intensity. Crab cavity system is installed at ~14m upstream from IP to recover luminosity loss due to the beam crossing.

Major issues for the BDS design are summarized as follow.

- Chromaticity (ξ) correction of final doublet, where the beam size increase ($\Delta\sigma/\sigma$) is proportional to the energy spread ($\delta E /E$) with a coefficient of ξ . The ξ exceeds 10,000 at ILC.
- Beam diagnostic and tuning with precise measurement of micron size beam, energy and polarization.
- Beam-beam effect at IP producing $\mathbf{e^+ e^-}$ pair background and disrupted beam at IR and extraction line to the beam dump, respectively.
- Beam halo originating from the main LINAC requiring robust collimation for synchrotron radiations and muon wall for resulting muons.

As listed above, the primary role of the final focus system is to demagnify the beam to the design value of 474nm horizontal and 5.9nm vertical at the IP. As shown in Figure 3, the FF optics creates a large and almost parallel beam at the entrance to the final doublet (FD) of strong quadrupoles. Since particles of different energies have different focal points, the FD creates large chromaticity so that the beam size inreases even with the small energy spread of ~0.1% if no correction is applied. This large chromaticity is compensated by two sexupoles interleaved with the FD, utilizing dispersions generated at upstream bending magnets. The second order dispersion generated in the FD is locally cancelled in the same way. Half of horizontal chromaticity is produced upstream of a bend. The second order geometric aberrations are cancelled by pairing two sextupoles upstream of the bend. The third order aberrations are cancelled by optimizing transfer matrixes between the sextupoles.
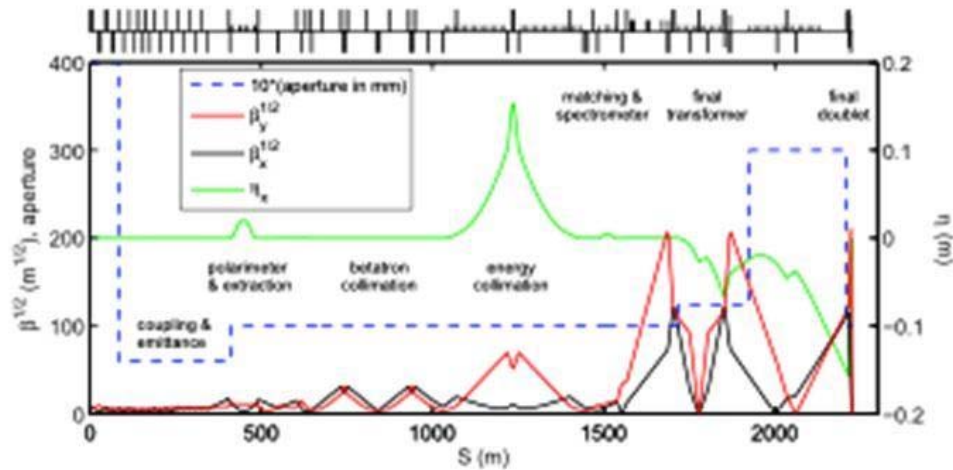
Figure 3: BDS optics, subsystem and vacuum chamber aperture; S is the distance measured from the entrance [1].

The emittance is diluted in the bending magnets so that the bending radius is maximized to keep the dilution of less than 0.5% at the beam energy of 250GeV. Since the FF can be upgraded for higher beam energy of 500GeV where the emittance dilution will be controlled to be less than 1%, there is space for additional bending magnets. At lower energy, every fifth bending magnet is installed.

2.1.2.1 *References*

1. ILC Global Design Effort, "ILC Technical Design Report", Vol. 1-4, (Volume 3 - Accelerator), 12 June 2013, http://www.linearcollider.org/ILC/Publications /Technical-Design-Report.

2.1.3 **CLIC Final Focus Optics**

R. Tomas, H. Garcia, Y.I. Levinsen and M. Modena
European Organization for Nuclear Research (CERN)
Mail to: Rogelio.Tomas@cern.ch, Hector.Garcia.Morales@cern.ch,
Yngve.Inntjore.Levinsen@cern.ch, Michele.Modena@cern.ch

2.1.3.1 *Introduction*

The CLIC Conceptual Design Report [1] presents the machine aspects for a collider with an energy in the center of mass of 3 TeV. Parameters for this option are shown in Table 2. The lower energy machine at 500 GeV was conceived to be operated in a staged approach having a layout fully compatible with that at 3 TeV and at the cost of a compromised performance at the lower energy. In the post-CDR phase the CLIC parameters are under review (including energy stages) with extra emphasis in the performance optimization at lower energies. This article presents the status of the 3 TeV Final Focus System (as it is in the CDR) and the plans to reach an optimum parameter set for the low energy range between 350 and 500 GeV.

**Table 2:** CLIC Beam Delivery System main parameters at 3 TeV CM.

Parameter	Units	Value
Length (linac exit to IP distance)/side	m	2750
Maximum Energy/beam	TeV	1.5
Distance from IP to first quad, L*	m	3.5-6
Crossing angle at the IP	mrad	20
Nominal core beam size at IP, σ^*, x/y	nm	45/1
Nominal beam divergence at IP, θ^*, x/y	μrad	7.7/10.3
Nominal beta-function at IP, β^*, x/y	mm	10/0.07
Nominal bunch length, σ_z	μm	44
Nominal disruption parameters, x/y		0.15/8.4
Nominal bunch population, N		3.7×10^9
Beam power in each beam	MW	14
Preferred entrance train to train jitter	σ	< 0.2
Preferred entrance bunch to bunch jitter	σ	< 0.05
Typical nominal collimation aperture, x/y	σ_x/σ_y	15/55
Vacuum pressure level, near/far from IP	nTorr	1000/1

2.1.3.2 *3 TeV FF*

The role of the Final Focus System (FFS) is to demagnify the beam to the required size (σ_x=45 nm and σ_y=1 nm) at the IP. The FFS optics creates a large and almost parallel beam at the entrance to the Final Doublet (FD) of strong quadrupoles. Since particles of different energies have different focal points, even a relatively small energy spread of 0.1% significantly dilutes the beam size, unless adequate corrections are applied. The design of the FFS is thus mainly driven by the need to cancel the chromaticity of the final doublet. The CLIC FFS has a baseline local chromaticity correction [2] using sextupoles next to the final doublets. A bend upstream generates dispersion across the final doublet, which is required for the sextupoles and non-linear elements to cancel the chromaticity. The dispersion at the IP is zero and the angular dispersion is about 1.4 mrad, i.e. small enough that it does not significantly increase the beam divergence. Half of the total horizontal chromaticity of the final focus is generated upstream of the bend in order for the sextupoles to simultaneously cancel the chromaticity and the second-order dispersion. The horizontal and the vertical sextupoles are interleaved in this design, so they generate third-order geometric aberrations. Additional sextupoles upstream and in proper phases with the final doublet sextupoles partially cancel these third order aberrations. The residual higher order aberrations are further minimized with octupoles and decapoles, see reference [3]. The final focus optics is shown in Fig. 4.
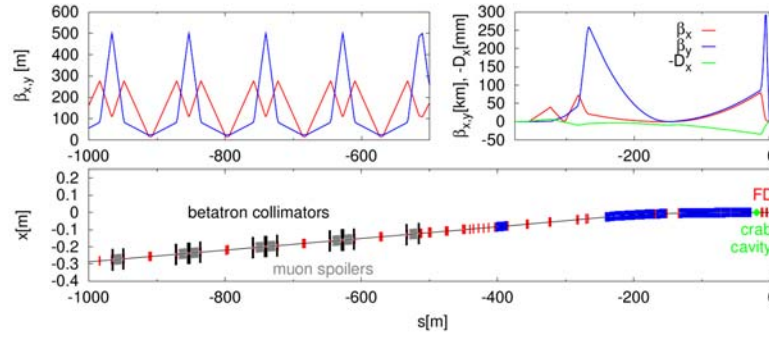
Figure 4: Optics (top) and layout (bottom) of the CLIC betatron collimation and final focus sections.
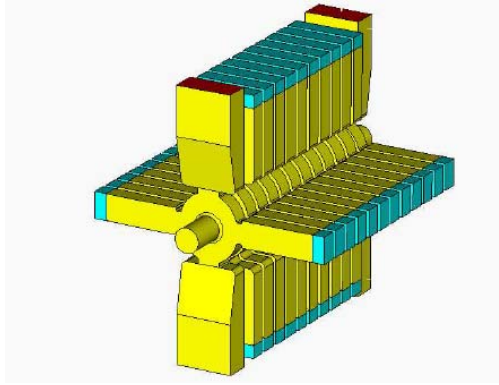
Figure 5: 12 cell crab cavity design including wakefield dampers (length of 300 mm).

With a 20 mrad crossing angle, crab cavities are required to rotate the bunches so they collide head on. A design of the 12 cell crab cavity is shown in Fig. 5. They apply a z-dependent horizontal deflection to the bunch that zeroes at the center of the bunch. The crab cavity is located prior to the final doublet (FD) as shown in Fig. 4 but sufficiently close to be at 90 degrees phase advance from the IP. In reference [4] it is shown that the small deviation from 90 degrees plus the interference with sextupoles produces a travelling waist at the IP. Therefore the sign of the crossing angle determines the direction of the travelling waist setting a preferred orientation to avoid luminosity loss (travelling waist, unfortunately, cannot significantly increase the luminosity given the CLIC parameters). The baseline crab cavities operate at 12 GHz and require a phase stability of 0.02 deg and an amplitude stability of 2% for a luminosity loss of 2%. Crab cavities also need strong high order mode damping.

Synchrotron radiation from all the Beam Delivery System (BDS) magnets causes a 22% luminosity loss. About 10% comes from the final focus bending magnets and another 10% originates at the final doublet quadrupoles. The CLIC vertical IP beta function is slightly below the theoretical beta function that minimizes the Oide effect [5, 6]. These numbers do not take into account the effect of the detector solenoid as this strongly depends on the final configuration of the interaction region. Recent simulations show that the theoretical minimum luminosity loss due to the current solenoid with anti-solenoid configuration should be 4%. Nevertheless the realization of a lattice actually achieving the 4% loss has not yet been demonstrated. A luminosity loss of about 6-7%

has been reached so far in tuning studies. The right adjustments of the length of the anti-solenoid, the L*, the detector solenoid field, the crossing angle together with appropriate coupling corrections should be explored to minimize this luminosity loss.

Table 3: Total luminosity and luminosity in the 1% energy peak for the various L* under consideration

L* [m]	total luminosity [10^{34}cm^{-2}s^{-1}]	peak luminosity [10^{34}cm^{-2}s^{-1}]
3.5	6.9	2.5
4.3	6.4	2.4
6	5.0	2.1
8	4.0	1.7

In the nominal configuration with L*=3.5 m the last quadrupole of the final doublet, QD0, sits inside the detector. In order to alleviate the engineering and the stabilization of this set-up it has been proposed, as a possible fallback solution, to move QD0 from the detector to the tunnel, consequently increasing L*. A collection of final focus systems with L* values between 3.5 and 8 m has been studied for CLIC. The performance of these FFS is shown in Table 3. Both the total luminosity and the luminosity in the energy peak degrade as the L* increases. Only the cases with L* of 3.5 and 4.3 m meet the CLIC requirement of a peak luminosity of 2×10^{34} cm^{-2}s^{-1} with a 20% margin for static and dynamic imperfections. The shortest L* that allows removing QD0 from the detector is 6 m. The FFS with L* =6 m meets the CLIC requirements with a tight margin of 5% for the imperfections. The last case with L* =8 m does not provide sufficient luminosity.

The biggest challenge faced by the beam delivery system is the demonstration of the performance assuming realistic static and dynamic imperfections. The diagnostics and the collimation sections have demonstrated to be robust against misalignments (prealignment of 10 μm over 500 m). Standard orbit correction techniques, such as the dispersion free steering, guarantee the beam transport without blow-up in these regions. However these techniques fail in the Final Focus System. The CLIC FFS is a very non-linear system with a β_y pushed down to 0.07 mm. Many different approaches have been investigated to tune the FFS in presence of realistic misalignments. Currently the two most successful approaches are:

- **Luminosity optimization:** Maximizes the luminosity using all the available parameters in the FFS applying the Simplex algorithm.
- **Orthogonal knobs:** Maximizes the luminosity by scanning pre-computed arrangements of sextupole displacements (knobs) which target the IP beam correlations in an orthogonal fashion.

These approaches are simulated for 100 statistical realizations of the CLIC FFS with misalignments. The final luminosity distribution and the number of iterations are shown in Fig. 6 for these two approaches in black and blue. The number of iterations corresponds to the number of luminosity measurements. A random error up to 3% has been assumed for the luminosity measurement. Neither the Simplex approach, nor the orthogonal knobs reach a satisfactory result in terms of luminosity. However since the orthogonal knobs are much faster it is possible to apply them after the Simplex

approach. This corresponds to the magenta curves in Fig. 3, showing 90% probability of reaching 90% of the design luminosity and requiring a maximum of 18000 iterations. The achieved luminosity performance is close enough to the desired 90% probability of reaching 110% of the design luminosity since new approaches or extensions will further improve the final luminosity, e.g., non-linear knobs.

To convert the number of iterations into time it is required to know how long a luminosity measurement will take. A conventional measurement of luminosity takes between 7 and 70 minutes, however faster indicators exist utilising different combinations of beamstrahlung signals and hadronic events [7]. These studies suggest that less than 10 bunch crossings should be enough to obtain accurate signals for tuning. Therefore 18000 iterations would take about an hour, which is reasonable for tuning the BDS from scratch.

During the CLIC technical design phase special focus needs to be put in improved tuning algorithms taking into account realistic errors in all BDS elements (e.g. the solenoid and the crab cavity were excluded in this study). The e− and e+ BDS lines should be optimized simultaneously and more robust final focus designs could be considered.
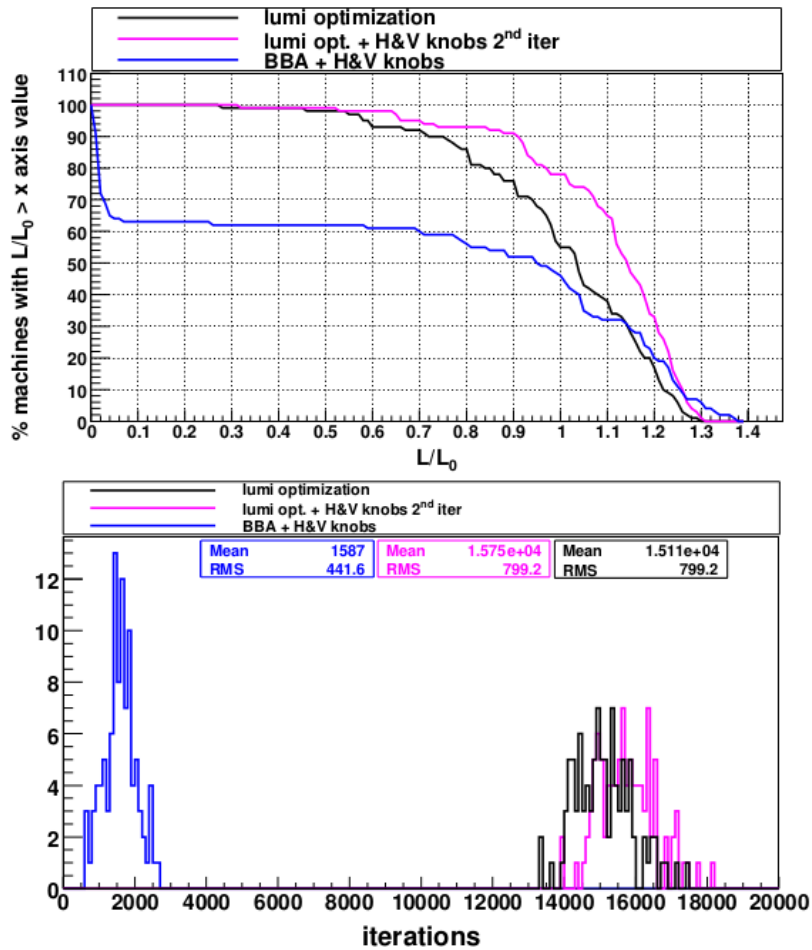
Figure 6: Top: Luminosity performance for 100 statistical realizations of the CLIC FFS after tuning using 3 differentapproaches. Bottom: Required number of luminosity measurements for the 3 different approaches.

2.1.3.2.1 Final Doublet

Figure 7 shows the tight integration of the QD0 quadrupole with the vacuum pipe of the incoming beam (smaller diameter) and the vacuum pipe of the outgoing beam (larger diameter). The incoming and outgoing beam-lines cross at an angle of 20 mrad and the outgoing (post-collision) vacuum pipe has a conical shape with a half opening angle of 10 mrad.
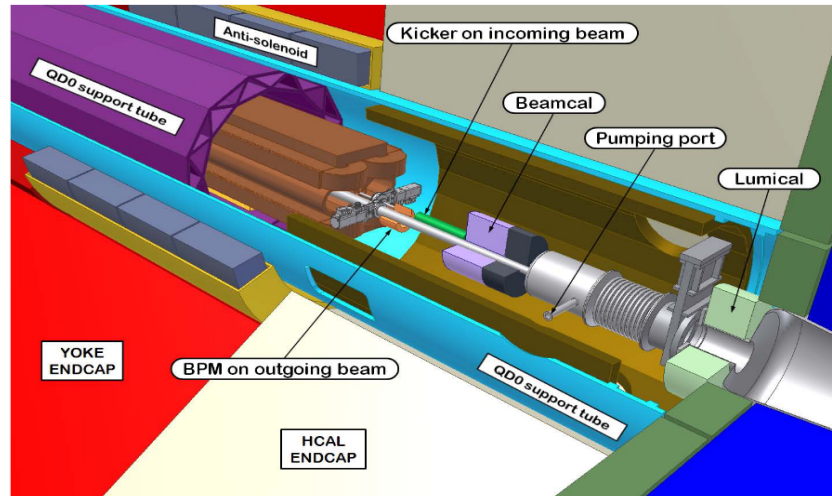
Figure 7: Interaction region showing the QD0 support tube surrounded by the anti-solenoid and all the other elements down to the Lumical.

QD0 is a compact 'hybrid' magnet with permanent magnet inserts and classical electro-magnetic coils. This choice was motivated by: the need for a compact magnet with very high gradient (575 T/m with an aperture radius of 4 mm), the need to tune the gradient (-20% estimation), the mentioned presence of the post-collision beam pipe, and the engineering difficulties in winding superconducting coils with such a small aperture and the impossibility to devise stabilisation techniques of the coils to the subnanometer level. Since the QD0 uses permendur and permanent magnet material, the QD0 must be shielded from external field. In order to both shield the QD0 magnet and reduce the beam distortions, an anti-solenoid design was also developed [8].

The magnets in the final doublet have the tightest tolerances in terms of field quality. Table 4 summarizes the tolerances of the QF1 and QD0 multipolar components at a radius of 1mm for a luminosity loss of 2%. QF1 features tighter tolerances than QD0 reaching 10^{-5} relative field accuracy for the low order skew components.

Table 4: QF1 (left) and QD0 (right) multipolar tolerances in 10^{-4} relative units at a radius of 1 mm for a 2% luminosity loss.

	min	max
b3	-0.4	2.2
b4	-2.5	3.3
b5	-4	18
b6	-15	32
a3	±0.2	
a4	±0.5	
a5	±1.7	
a6	±4.8	

	min	max
b3	-1.8	0.5
b4	-27	6
b5	-220	80
a3	±0.7	
a4	±8	
a5	±130	
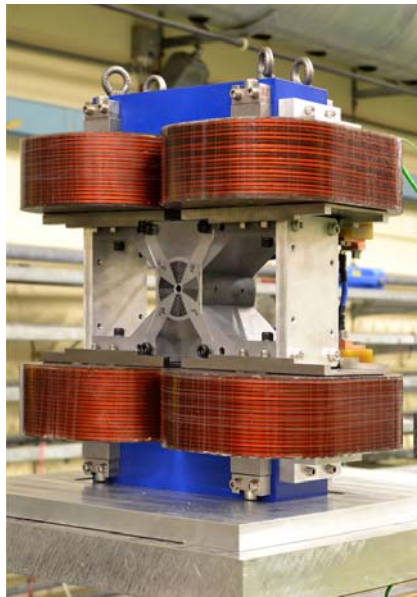
Figure 8: CLIC QD0 prototype.

A CLIC QD0 short prototype has been successfully built [9], see Figure 8. It has achieved 90% of the design gradient with an excellent field quality. Table 5 shows the measured multipolar components at 1 mm. Only the a3 component is out of specification. The origin of this unexpected out of specification and methods to further improve this field quality are under investigation. Nevertheless the adverse effects of the a3 component are easy to mitigate thanks to the nearby SD0 sextupole.

SD0 features similar difficulties in terms of magnet design as QD0. As a matter of fact a similar conceptual design [10] has been proposed as shown in Fig. 9.

Table 5: Measured multipolar components of the QD0 prototype in the usual 10^{-4} relative units and at a radius of 1 mm.

b3	0.71	a3	4
b4	3.36	a4	-0.4
b5	-0.31	a5	-0.41
b6	-0.72	a6	0.16
b7	0.02	a7	-0.01
b8	0.00	a8	0.00
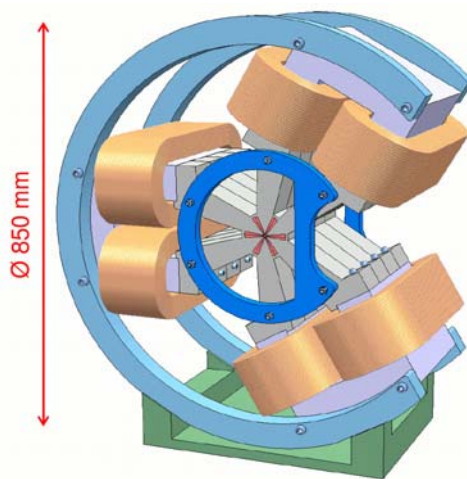
Figure 9: CLIC SD0 design as proposed in [9].

2.1.3.3   *Lower Energies between 350 and 500 GeV*

The CLIC IP beta functions at low energies are being explored in order to probe the entire machine parameter phase space. Traditional values of the horizontal beta function range between 8 and 10 mm. Lower values give larger total luminosity at the cost of a degradation of the collision energy spectrum. Nevertheless this can be used to reduce the charges per bunch easing the design and operation of the linac and the damping ring. The current final focus conceptual design with a doublet as a final lens assumes an IP horizontal beta function considerably larger than the vertical one. However limits in the ratio or in the absolute value of the horizontal beta function are not well understood. Three lattices have been designed with the vertical beta function pushed to the hourglass effect limit (0.065 mm) and for horizontal betas of 8, 6, and 4 mm. The dispersion throughout the final focus system has been optimized case-by-case without considering any constraints from the higher energy layout. Figures 10 and 11 show the total and peak luminosities for these lattices together with luminosities from ideal distributions versus number of particles. A clear sign of strong aberrations appears at 4 mm, where the luminosity of the corresponding final focus design only reaches 83% of that from ideal distributions.
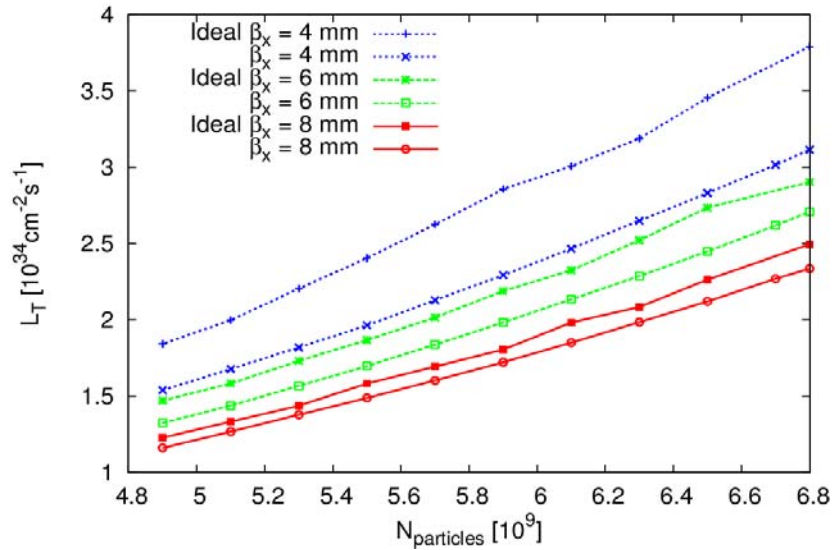
Figure 10: Total luminosity versus number of particles per bunch and for 3 different IP horizontal beta functions using ideal distributions and new FFS designs. The vertical beta function has been set to the minimum value allowed by the hourglass effect (0.065mm).
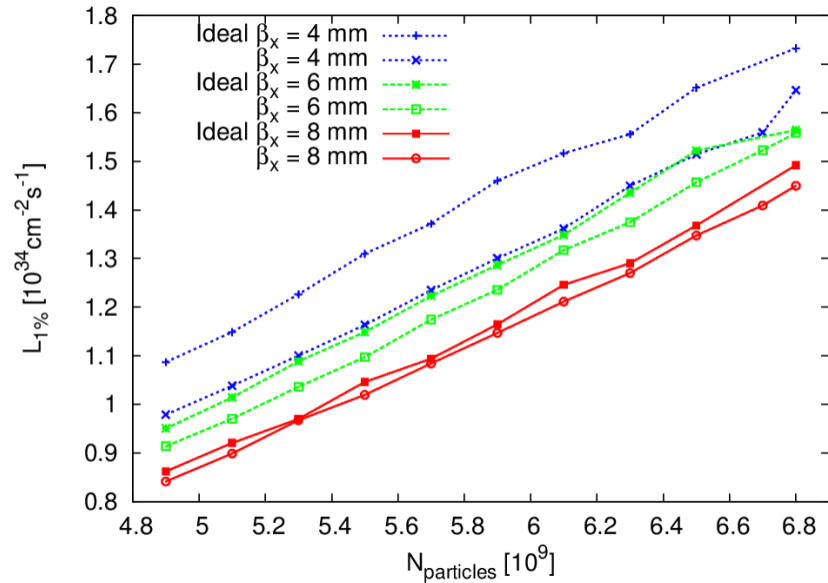
Figure 11: Peak luminosity versus number of particles per bunch and for 3 different IP horizontal beta functions using ideal distributions and new FFS designs. The vertical beta function has been set to the minimum value allowed by the hourglass effect (0.065mm).

Further studies are being carried out to fully understand the limitations and the sources of the higher order aberrations at 4 mm which might lead to cures and even lower beta functions or to establishing lower boundaries for the beta functions.

2.1.3.4   *A CLIC-based FFS for ILC*

The CLIC and ILC Final Focus Systems are both based in the local chromaticity correction scheme [2]. The optimization procedure is very similar in both schemes in order to correct the nonlinear aberrations and to achieve the maximum luminosity.

Table 6 shows a comparison of CLIC 500 GeV and ILC 500 GeV beam and machine parameters at the Final Focus System. There are no parameters deviating more than a factor of four between CLIC and ILC. It is conceivable that a single FFS lattice design could serve both projects. To illustrate this point the CLIC FFS has been used to reproduce the ILC parameters.

Table 6: CLIC and ILC BDS parameters comparison.

Parameter	Unit	CLIC500	ILC500
Beam energy	GeV	250	250
Bunches per train		354	1314
Bunch population	10^9	6.8	20
Repetition rate	Hz	50	5
Hor. Norm. emittance	μm	2.4	10.0
Vert. Norm. emittance	nm	25	35
Hor. Beta at IP	mm	8.0	11.0
Vert. Beta at IP	mm	0.1	0.48
Hor. beam size at IP	nm	200	474
Ver. Beam size at IP	nm	2.26	6.0
Bunch length	μm	72	300
Energy spread (rms)	%	0.3	0.125
Luminosity	$10^{34}\text{cm}^{-2}\text{s}^{-1}$	2.3	1.47

As one can see in Table 7, the CLIC-based FFS lattice and ILC FFS lattice present similar performances in terms of IP beam sizes and luminosity. There are many more aspects to consider before claiming a CLIC-based FFS for ILC but this certainly represents a first step towards a common study framework between the two linear collider projects. Having a common FFS lattice would have immediate benefits in the resources needed to maintain the lattice and carry out simulations. Some overhead and compromises might be needed to take into account the particularities of both systems.

Table 7: Performance comparison for ILC and CLIC-based FFS.

Parameter	ILC	CLIC-based
Length [m]	735	553
βx / βy [mm]	11/0.48	11/0.48
σx [nm]	499.3	483.7
σy [nm]	6.03	5.89
Total Luminosity [10^{34} $cm^{-2}s^{-1}$]	1.39	1.47
Peak Luminosity [10^{34} $cm^{-2}s^{-1}$]	0.86	0.89

Independently of the lattice design option the technology choice can also be harmonized between CLIC and ILC. For example ILC features a superconducting final doublet while CLIC resorts to hybrid technology as described above. Since a CLIC short prototype has already been successfully built it is natural to explore the possibility of using this hybrid technology for ILC. In [10] a design of a CLIC-like QD0 for ILC is presented. Figure 12 shows the proposed design together with the field lines in a region containing the beam pipe and the aperture for the extracted beam (indicated by the blue circle). The design meets the ILC specifications with some margin that might be used for further optimizations.
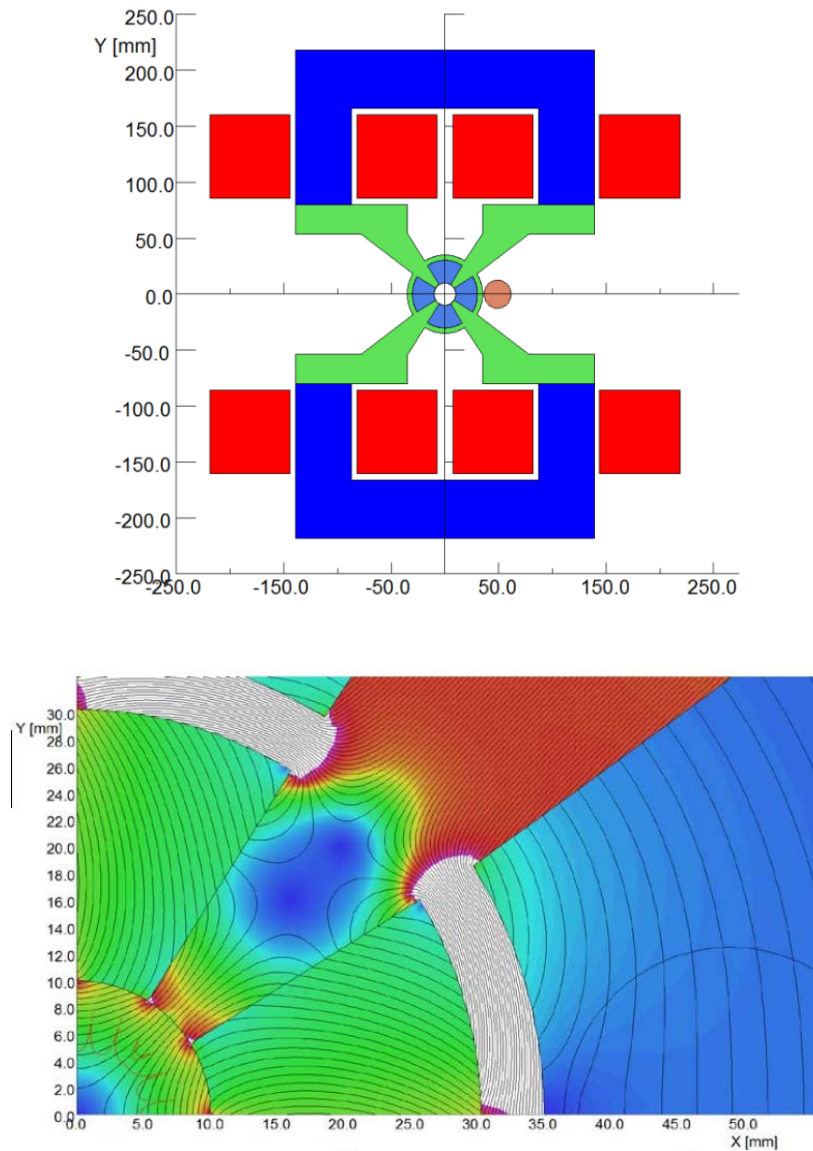
Figure 12: QDO design based on hybrid technology proposed for the ILC FFS [10]. The top figure shows a transverse section of the design and the bottom plot shows the field lines in the main beam pipe and the aperture for the extracted beam.

2.1.3.5 *References*

1. "CLIC Conceptual Design Report", CERN-2012-007.
2. P. Raimondi and A. Seryi, Phys. Rev. Lett. 86, 3779-3782.
3. R. Tomás, ``Nonlinear optimization of beam lines'', Phys. Rev. ST Accel. Beams 9, 081001 (2006).
4. J. Barranco, E. Marin, and R. Tomas, "Luminosity studies in a traveling waist regime in the Compact Linear Collider", Phys. Rev. ST Accel. Beams 16, 041001, Published 4 April 2013
5. K. Oide, Phys. Rev. Lett. 61, 1713 - 1715 (1988).

6. R. Tomás et al, "Summary of the BDS and MDI CLIC08 Working Group", CLIC-Note-776.
7. B. Dalena, J. Barranco, A. Latina, E. Marin, J. Pfingstner, D. Schulte, J. Snuverink, R. Tomas, and G. Zamudio, ``Beam delivery system tuning and luminosity monitoring in the Compact Linear Collider'',
   Phys. Rev. ST Accel. Beams 15, 051006, Published 30 May 2012.
8. A. Bartalesi, M. Modena, "Design of the anti-solenoid system for the CLIC SiD experiment" TE-MSC Note 2012-11, EDMS N. 1214775
9. M. Modena et al. "Design, assembly and first measurements of a short model for CLIC final focus hybrid quadrupole QD0" Proceedings of IPAC 2012, New Orleans, Louisiana, USA.
10. M. Modena et al, "CLIC QD0 and other BDS and Post-collision line magnets", ECFA LC2013, Hamburg, Germany.

2.2 Lessons from the LC Final Focus System at ATF2

2.2.1 Accelerator Test Facility (ATF) Overview

Shigeru Kuroda
High Energy Accelerator Research Organization (KEK), Japan
Mail to: shigeru.kuroda@kek.jp

KEK Accelerator Test Facility (ATF) [1] has been built for accelerator R&D, especially for linear collider(LC) issues. The purpose of the ATF is to produce low emittance beam and to supply the beam to the other studies. Fig 1 shows the schematic view of the ATF accelerator complex. It consist of injector linac, damping ring (DR) and extraction(EXT)/final focus(FF).
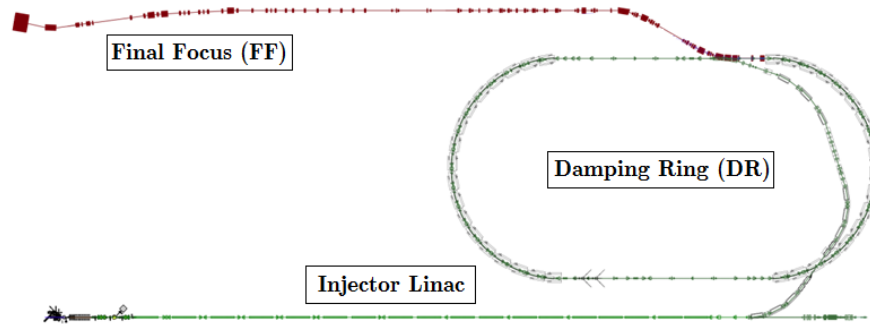
Figure 1: Schematic View of ATF Accelerator Complex

Table 1: ATF Operation Parameters

Energy	1.3 GeV
# of electrons per bunch	< 2e10
Repetition rate	3.56 Hz
# of bunch in a pulse	≤ 10
# of bunch train in DR	≤ 3

Some parameters in operation are in Table.1. DR energy is 1.3GeV. Electron beam intensity is variable below 2e10. Some R&Ds require multi-bunch and/or multi-train operation.

A photo-cathode RF gun system is a source of the ATF electron beam. It is 3.5-cell RF cavity and the photo-cathode is made of thin film of Cs-Ta alloy formed on molybdenum surface. The electron beam is accelerated to 1.3GeV by S-band (2856MHz) linac. Length of the linac is about 70m. 8 units of RF system are used for regular acceleration. There are 2 more units for energy compensation in multi-bunch operation. In the regular acceleration unit, pulses from a klystron are compressed to high peak power in SLED, and delivered to two 3m accelerating tubes. 1.3Gev electron beam is then transported to the DR.

The damping ring (DR) is a race-track type storage ring. It has superperiod of 2. Circumference is about 140m. One of the straight sections is for injection and extraction and the other is for RF section. Some parameters of the ring are tabulated in Table 2.

Table 2: Damping Ring Parameters

Circumference	138.6m
RF frequency	714MHz
Momentum Compaction Factor	0.00214
Equilibrium Emittance	1.1nm
Equilibrium Momentum Spread	6e-4
Tunes(x/y)	15.17/8.56
Damping Time(x/y/z)	17/27/20 ms
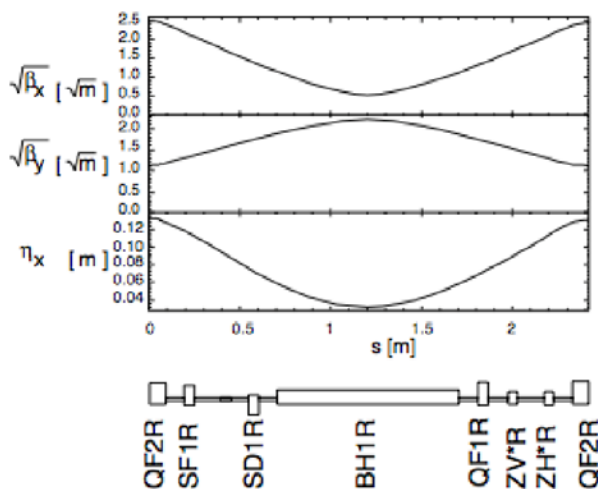
Figure 2: Optics of Arc cell

Arc cell is so-called FOBO type, where B stands for combined functioned bending magnet. Optics there is shown in Fig.2. Dispersion function is minimized in this bending magnet for small equilibrium emittance. Production of very low vertical emittance is one of the goal of ATF. It is done and the vertical emittance less than 10pm is measured [2,3]. Emittance tuning is basically by dispersion and coupling correction. The tuning techniques are so matured that the low emittance is successfully kept in these days [4].

The damped beam is delivered to EXT/FF section. The detail there is described in the following sections.

2.2.1.1 *Reference*

1. Edited by F.Hinode *et al.*, "ATF design and study report"; KEK Internal 95-4 (1995).
2. K.Kubo *et al.*, Phys. Rev. Lett. **88** (2002) 194801.
3. Y.Honda *et al.*, Phys. Rev. Lett. **92** (2004) 054802.
4. S.Kuroda, talk in ATF2 topical meeting, July 8, 2013.

2.2.2 ATF2 Optics Design

Glen White
SLAC National Accelerator Laboratory, USA
Mail to: whitegr@slac.stanford.edu

2.2.2.1 *Introduction*

The purpose behind the construction of the ATF2 final focus system (FFS) is to test the novel local-style chromatic correction system envisioned for future linear colliders, as described within the beam optics design section of this newsletter [1]. The optics design implemented at ATF2 was chosen to closely resemble that required for ILC (see Figure 1). As at ILC, the upstream optics (the extraction line (EXT) from the damping ring in the case of ATF2) is responsible for dispersion, coupling correction and betatron matching into the FFS [2]. The task of the FFS then is to take the delivered beam and de-magnify it to the desired interaction point (IP) horizontal and vertical spot sizes. It also needs to correct for the aberrations the FFS itself introduces. As detailed in [1], the predominant aberration is due to the chromaticity of the strong final doublet quadrupole magnets. The main other aberrations that have to be removed are due to imprecise incoming corrections from the EXT, static and dynamic misalignments of magnets, imprecise magnetic field settings and unwanted higher-order field components of magnets. The five sextupole magnets that provide for the correction of the chromaticity within the FFS are placed on mover systems (with horizontal, vertical and roll degrees of freedom) and are also used to correct for the linear static aberrations directly at the IP (as detailed in [3]). Four skew-sextupole magnets have also been introduced (not envisioned in the original ILC design) to increase the tolerance of the optics to magnet multipole field errors and to provide second-order aberration correction capability at the IP (also see [3] for more details). Altogether, the FFS then contains a total of 3 dipole, 28 quadrupole, 5 sextupole and 4 skew-sextupole magnets. Plus 4 dipole corrector magnets for orbit steering and slow feedback in the horizontal and vertical planes.

Table 1: Key FFS parameters for ILC, CLIC, ATF2 and FFTB (traditional style FFS test facility at SLAC). ^ = SiD/LCD ILC detector configuration. + = positron/electron side of ILC. * = Recent results and configuration of ATF2 with low charge (~0.2nC).

	ILC (TDR 500 GeV)	*ATF2*	*FFTB*	*ATF2 (pushed)*	*CLIC (CDR 3TeV)*
L^* (m)	3.5 / 4.5 ^	1	0.4	1	3.5
ε_y (pm.rad)	0.07	12	34	12	0.003
$\xi_y \sim (L^*/\beta^*_y)$	7,300/9,400 ^	10,000	4,000	33,000	50,000
σ_E	0.07/0.12 % +	0.08 (0.06*) %	0.3 %	0.08 %	0.3 %
$\Delta\sigma_y/\sigma_y \sim (\sigma_E.L^*/\beta^*_y)$	5/9 , 7/11 +,^	8 (6*)	12	26	150
σ_y (nm)	5.9	37	60	20	1
σ_y (nm) *Achieved*	---	65 +/- 5 *	77 +/- 7	---	---
β^*_x (mm)	11	4 (40*)	10	4 - 40	4
β^*_y (mm)	0.48	0.1	0.1	0.03	0.07

Figure 1: Betatron and dispersion functions within the ATF2 and ILC final focus systems.

2.2.2.2   *Optics Design Specifications*

The FFS of a future linear collider is arguably the most complex part of the accelerator facility to operationally tune to enable the delivery of the design luminosity at the IP. Most of the complexity in the operation of the FFS stems from the requirement to correct for the high chromaticity of the system using nonlinear (sextupole) magnets. A way of assessing the level of "difficulty" involved can be approximated by considering the magnitude of beam size growth due to the uncorrected chromaticity of the FFS. Also one should take into account geometric aberrations and the impact of errors on the tuning procedure itself to fully describe the relative difficulties of different lattices, requiring full simulations. A fully self-consistent and fair way of achieving this is currently under investigation. Here, this is approximated in table 1 by considering the product of the energy spread and final doublet chromaticity (highlighted row in table). The parameters for ATF2 were chosen to present us with a system of comparable tuning difficulty to the design parameters for the ILC. It can also be seen that through further reduction of the IP vertical beta function the tuning complexity of the system can be increased. This is useful to study where the practical limitations of such a FFS design may lie.

2.2.2.3   *FFS Matching*

The linear optics of the FFS are matched with the following constraints:
- IP horizontal and vertical beta functions
  - Nominal design 4mm x 0.1mm
- Zero alpha at IP (waist located at IP)
- Phase advance between FFS IP image point locations and IP of 90 degrees
  - MFB1FF and MFB2FF feedback BPM locations, or alternatively FFS laserwire IP waist
- Phase advance between FFS IP image points and upstream dipole correctors (90 degrees) for 2-phase FFS slow feedback system.

For small changes to the linear optics (e.g. changes to the IP beta functions), the higher-order optics functions can be matched using the FFS sextupole strengths and a simplex algorithm. For more fundamental changes and initial configuration, the full FFS design procedure referred to in [1] is followed. Examples of small-scale changes to the linear optics can be seen in figure 5.

2.2.2.4   *Rationale behind Beam Optics Tests at ATF2 for Verification of Operability at a Future Linear Collider*

To access the required physics at the highest energy scales and to keep costs to a minimum (beam power) are compelling reasons to push for FFS optics designs that de-magnify the beam to the smallest achievable sizes at the IP. To this end, the next generation of colliders require focusing optics designs that push design parameters into a new regime for beam operations: that in which the tolerances of the system are beyond the ability of existing or envisioned manufacturing and surveying techniques to achieve. Instead, part of the optics design of such a FFS must include correction systems to dynamically correct for installed and operational "defects" (excursions from the ideal design parameters of the system). As part of the design process, the ability for a given FFS design to correct for expected beamline component imperfections must be

evaluated. The steps of this evaluation process, performed using tracking simulations, can be summarised as:

1. Model effects where realistic error conditions destroy the properties of the FFS. Constructing a Monte Carlo simulation consisting of multiple possible "seeds" of error conditions does this.
2. The resulting aberrations present at the IP are analysed based on the modelled error conditions and correction "multi-knobs" such as those described in [3] are constructed.
3. The constructed multi-knobs are themselves limited by beamline imperfections and to dynamic drift effects. These limitations effect how orthogonal such knobs can be and the range of their applicability. This impacts the tuneability of the FFS in a non-trivial way that must be determined through a complete simulation of the FFS tuning procedure including all operational limitations expected.

By following the above procedure and specifying a complete set of expected beamline error sources, the tuning performance of the system is evaluated. This procedure is computationally complex, requiring many detailed simulation steps. The details of the simulation are important and require the correct treatment of tracking through non-linear accelerator elements. To reduce the possibility of errors (either internal errors to the simulation codes themselves, or due to the applied use of the simulation codes to model the tuning procedure), it is desirable to have multiple tuning simulations constructed using different simulation tools and by different people. The optics design is considered useable if the majority (usually 90% of seeds is the benchmark taken) of the considered simulation seeds tune to provide the desired beam conditions at the IP. More details of this procedure can be found in [4] and [5] for ILC and ATF2.

The ATF2 experiment provides a way to validate this design procedure and to give confidence that this novel FFS design can produce the desired luminosity in a future linear collider. The key parts of the experiment are to verify that the optics correctly removes the intrinsic chromaticity and that the builtin aberration countermeasures work as simulated in the presence of the considered error sources. By comparing experimental tuning results to the expectations from simulations, we learn about if we correctly describe all the pertinent error sources and about if we correctly model their effect on the tuning along with the multiknobs designed to remove these effects. We also hope to find ways to improve the design to help operationally with the tuning procedure at a future linear collider facility.

2.2.2.5   *Error Sensitivities and Tolerances*

In the context of evaluating the FFS tuneability, the terms sensitivity and tolerance are used to describe distinctly different properties related to the treatment of beamline errors. Error *sensitivities* are defined by the effect on the IP beamsize/luminosity a given error (e.g. vertical mechanical offset of magnet away from design) has. Examining the list of sensitivities is useful during the optics design to understand where the optics are most sensitive. These should not be considered to be the requirements on placement or mechanical construction *tolerance* however as they are often beyond that which is physically achievable. Instead, the error *tolerances* are given by how large a given error source can be and the total tuning procedure still converge to a satisfactory result given the complete dynamic error mitigation system (multi-knobs). Because the actual *tolerance* of the FFS tuning to a given error is so tightly correlated to the total tuning

procedure and other error sources, it is difficult to produce actual *tolerance* limits on an error source-by-error source case. Doing so would imply an impractical number of simulations. Instead, the *sensitivities* are listed for all error sources (the predominant ones are presented below) and the tuneability of the optics is demonstrated by varying all the error sources across an expected range and showing in a Monte Carlo simulation that the majority (at least 90%) of these cases are tuneable. The conclusion can then be drawn that as long as the errors of the deployed system fall within the studied ranges then the FFS is tuneable.

2.2.2.6 *Error Sources*

The list of error sources to consider for the FFS design can be considered in two categories: static sources and dynamic sources. Broadly speaking, one can consider the static sources as the errors that the tuning system removes during the optics commissioning; whilst the dynamic sources cause degradation in the FFS performance as a function of time after tuning. Of course, dynamic error sources also effect the efficiency of the tuning itself and must be considered as much as possible as part of the simulations of the tuning process.

2.2.2.6.1 Static Error Sources

- Transverse magnet alignment
  - RMS 200um random error assumed in addition to actual survey measurements (survey shows typically ~100um level of error)
- Magnet roll alignment
  - RMS 300urad random error plus measured survey values
- BPM -> magnet field centre initial alignment
  - 200um (operationally determined by BBA technique, the accuracy of which depends on other errors (lattice errors and BPM scale factors/resolutions)
- Magnet integrated strength errors (dK/K)
  - 0.1% RMS magnet-by-magnet random + 0.1% systematic offset
- Higher-order multipole fields (normal and skew components)
  - Use magnetic measurement data

2.2.2.6.2 Dynamic Error Sources

- BPM scale factor errors and resolutions
  - RMS 1% scale factor errors
  - 5um, 200nm, 2nm resolutions for stripline BPMs, cavity BPMs and IP cavity BPMs respectively
- Magnet mover accuracy
  - 2um (x/y), 10urad (roll)
- Magnet power supply regulation accuracy (setting accuracy)
  - 0.001% (FFS quads and sextupoles), 0.1% others
- Ground motion
  - Use direct measurements of relative ground motion and coherence from ATF2 floor [6]
- Mechanical magnet vibration

o   Assume vibration at 10nm RMS level. Measurements of the vibration of the outer part of the FD magnets with respect to the IP show performance below this [7].
- Statistical errors in IP beam size measurement system

2.2.2.7   *Static Error Sensitivities*
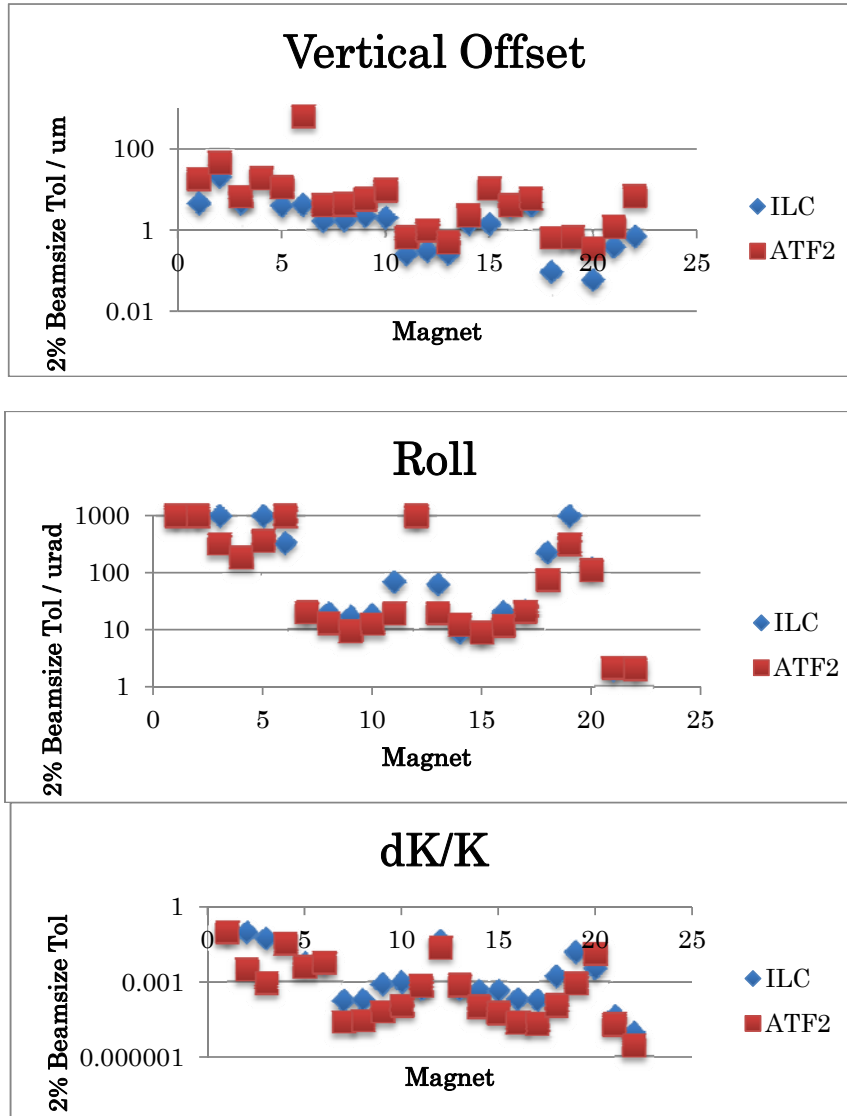
Figure 2(a,b,c): FFS sensitivities of IP vertical beam size to magnet placement and integrated field strength errors (magnitude of error required to grow IP beam size by 2% un-compensated by tuning knobs).

2.2.2.8   *Measurement and Mitigation of Magnetic Multipole Errors*

At the time of construction/refurbishment of the bend, quadrupole and sextupole magnets used in ATF2, magnetic measurements of all higher-order multipoles were taken. Figure 3 shows the sensitivities (magnitude of a given multipole component to

increase the vertical beam size at the IP by 1nm, or ~2 %) for sextupole and octupole (normal and skew) multipoles. It can be seen that a few magnets exceed the desired sensitivity requirements. In fact when considering all magnets, 6 sextupole, 12 skew-sextupole, 1 octupole, 4 skew-octupole, 2 skew-decupole, 1 12-pole and 2 skew-12-pole components are found to exceed the desired sensitivity requirements.

Figure 4a shows the simulated beam size including the effect of the measured magnet multipoles. For the nominal horizontal emittance, the vertical beam size is almost double that of the design value.

To compensate for this several steps can be, and have been taken. As described in [3], through the addition of 4 skew-sextupole magnets and multiknobs generated from adjusting the strength of these plus the original 5 sextupole magnets, the tolerances to the sextupole and skew-sextupole multipole components can be raised above the measured values. The majority of the remaining beam size growth was due to (mainly the skew-12 pole) QF1FF. A replacement magnet was sourced (previously used arc quadrupole from the PEPII LER) with improved field quality (see figs. 6 and 7). Following these steps, it is expected that the vertical beam size will be close to the design value (see figure 4b).

To further reduce the sensitivity to multipole field errors, different linear optics solutions were investigated to reduce the horizontal beam size in magnets with the largest multipole field errors (see figure 5). During recent runs, we operated with optics corresponding to 10 times the design IP horizontal beta function (4cm) with the goal of reducing this back to the design once the design vertical beam size has been achieved.

In order to enable operation at the most pushed vertical beta optics (as shown in table 1), we will need to take the additional steps of swapping QD0FF and swapping the locations of some of the other FFS quadrupole magnets.
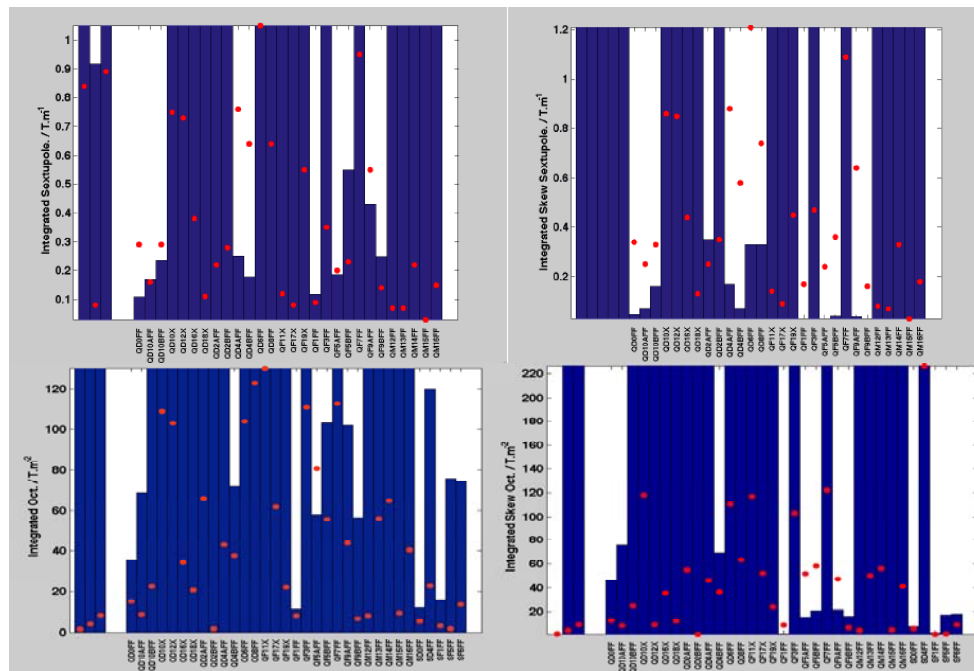
Figure 3: sensitivites of FFS magnets to multipole field errors (blue histogram) and measurements (red data points). Top left and right are sextupole, skew-sextupole terms. Bottom left and right are octupole, skew-octupole terms.
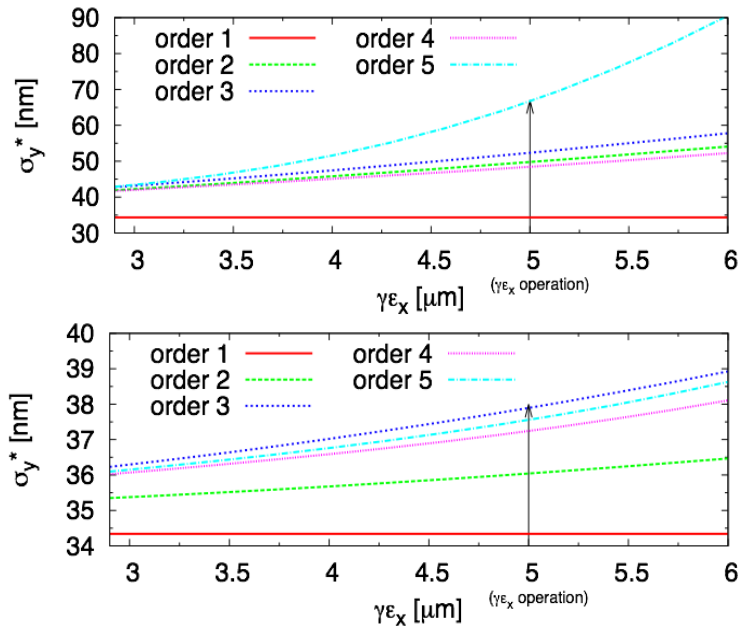
Figure 4: Vertical beam size as a function of horizontal emittance. (a), top inlcuding measured multipoles. (b), bottom including skew-sextupole mitigation and new QF1FF magnet.
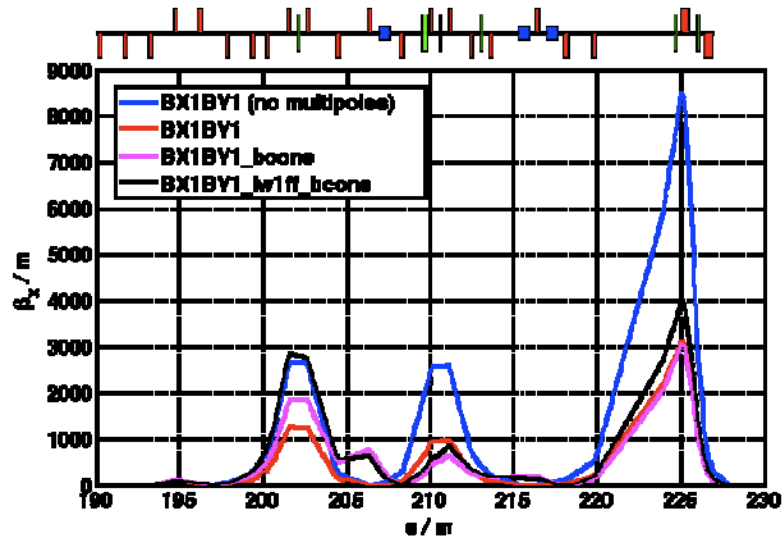
Figure 5: FFS horizontal beta functions for different match conditions.

Figure 6: Replacement QF1FF magnet installed at ATF2. Quadrupole magnet previously used as an arc quad in the LER ring at PEPII, SLAC.
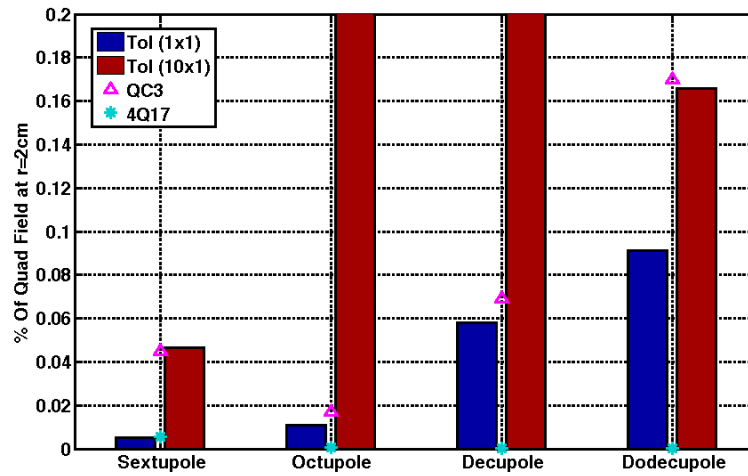
Figure 7: Multipole tolerances for QF1FF magnet for low and high IP-beta configurations. Measurements for new (4Q17) and old (QC3) magnets shown.

2.2.2.9   *Simulated Tuning Performance of ATF2 Optics Design*

A 100-seed Monte Carlo simulation (see [5] for some more detail of the simulation process) including the error sources listed here was performed to evaluate the performance capability of this optics. The results are summarised in figure 8. The initial BBA and tuning steps are simulated followed by 35 iterations of the IP multiknobs. At each stage, the next multiknob to be applied (to all seeds) is determined by the dominant aberration (averaged over all seeds) as shown for the final tuning step in the lower left plot in Figure 8.
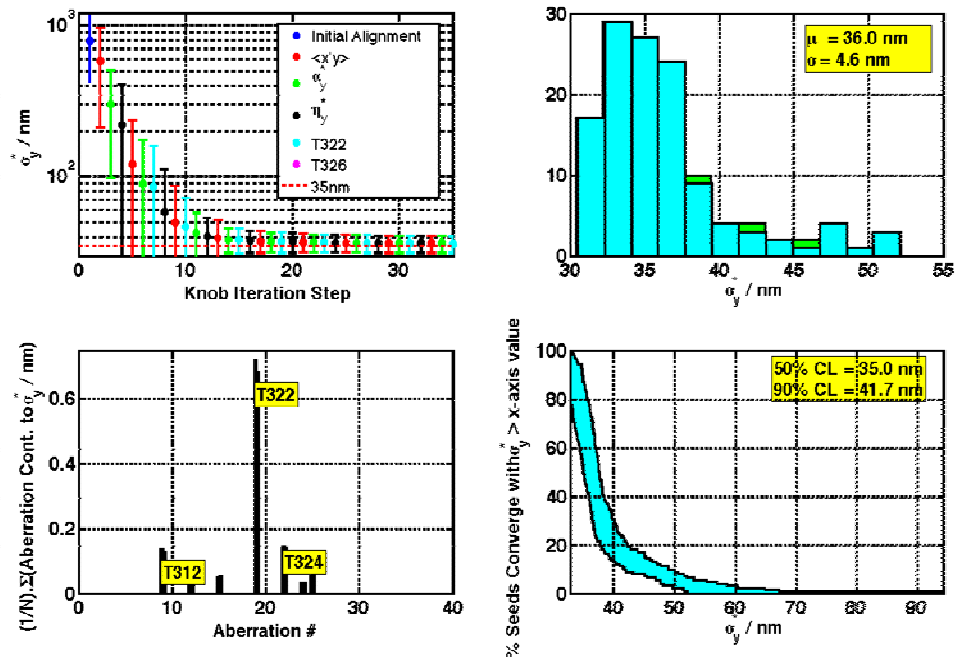
Figure 8: Monte Carlo simulation results for 35 iterations of IP multiknob tuning steps. The mean case tunes to the design 35nm, whilst 90% of seeds converge to <42nm.

2.2.2.10   *Simulated Impact of Dynamic Errors on ATF2 Optics Design*

Using a tuned simulation from the previous section and applying the dynamic error sources listed earlier plus applying orbit feedback, an expected beam size growth of 0.5nm per hour is found (see figure 9). To maintain the design vertical beam spot size at the IP over extended periods of time, linear and second-order tuning knobs (as discussed in [3]) need to be continuously applied. Simulations including ground motion on a timescale up to 2 weeks are shown in figure 10 along with the impact of continuous application of the tuning knobs.
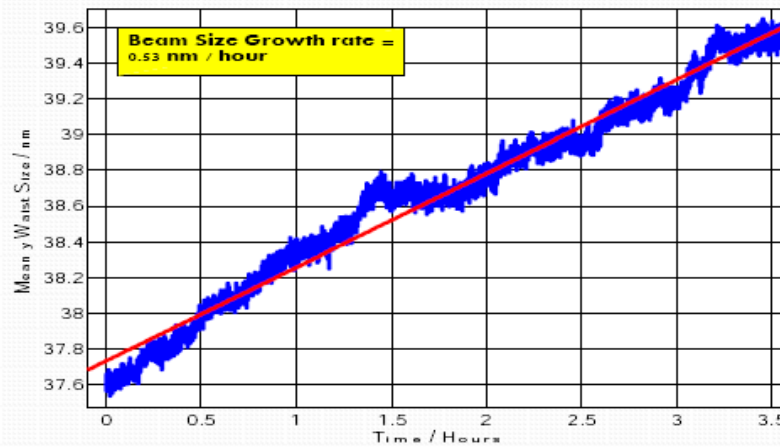
Figure 9: Beam size at IP as a function of time, including all dynamic error sources.
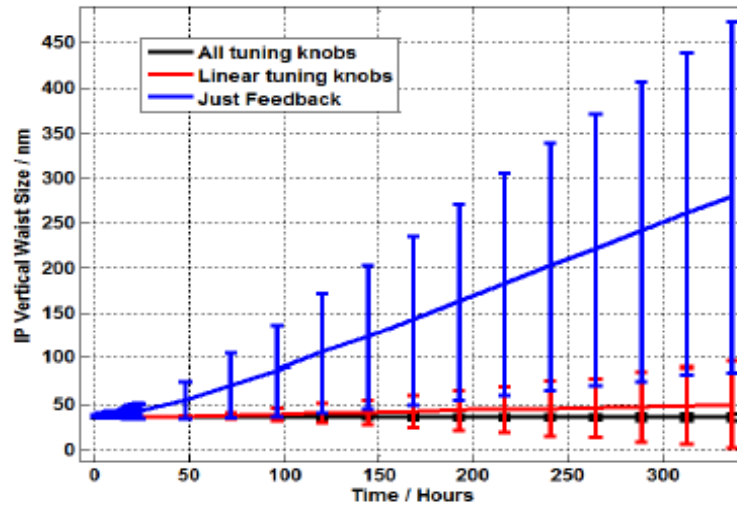
Figure 10: Beam size at IP as a function of time over a 2 week period. 100 seeds are simulated with the mean and RMS distributions shown.

2.2.2.11 *References*

1. Local chromaticity correction, this newsletter.
2. Extraction tuning and matching into the FFS, this newsletter.
3. IP beam size tuning, this newsletter.
4. Design of the Beam Delivery System for the ILC, A. Seryi et. al., PAC07-WEOCAB01.
5. Beam-Based Alignment, Tuning and Beam Dynamics Studies for the ATF2 Extraction Line and Final Focus System. G. White et al., EPAC08-MOPP039, SLAC-PUB-13303, Jul 25, 2008.
6. ATF2 proposal. Vol. 1 (sec. 7.3), B.I. Grishanov et. al. KEK-REPORT-2005-9
7. B. Bolzon et al. ATF-Report No. 09-01

2.2.3 **ATF2 Measurement: Extraction Tuning and Matching**

Mark Woodley
SLAC National Accelerator Laboratory, USA
Mail to: mdw@slac.stanford.edu

2.2.3.1 *Introduction*

The electron beam is extracted from the ATF Damping Ring (DR) in the horizontal plane using a pulsed kicker and a current-sheet septum magnet. The septum magnet (BS1X) is followed immediately by two additional strong, small cross-section dipole magnets (BS2X and BS3X), and together this system delivers the extracted beam to the ATF/ATF2 Extraction Line (EXT) at an angle of ~ 20°.

The EXT line proper begins with a "dogleg" inflector comprising two approximately 10° bends, separated such that the beamline exiting the inflector is offset from the North straight section of the DR by 6 m. Following this is an approximate mirror image of the kicker/septum system, consisting of a dipole magnet and a second pulsed kicker (more on the second kicker later), which brings the beamline parallel to the North straight section of the DR.

Following the inflector is a short ILC-style coupling correction system consisting of 4 skew quadrupole magnets in an optics which nominally allows for orthonormal correction of all four phases of transverse (*x-y*) coupling.

Next is an emittance diagnostic system, consisting (originally) of 5 wire scanners in an optics which provides measurements of the horizontal and vertical projected beam emittances and (uncoupled) Twiss parameters. This system was upgraded in 2005 with 4 OTR monitors, located near the original wire scanners, allowing for much faster measurements.

Finally, at the entrance to the ATF2 Final Focus (FF), is a group of six bipolar quadrupoles which provide for optics matching between the EXT and FF beamlines.

Figure 1 shows a schematic of the EXT line.
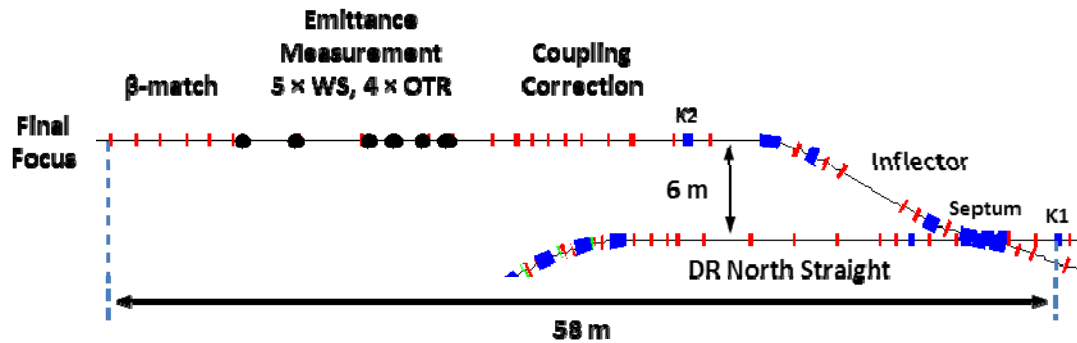
Figure 1: ATF/ATF2 Extraction Line schematic (beam direction is right to left).

2.2.3.2 *Functional Description*

2.2.3.2.1 Damping Ring Extraction

The DR extraction kicker is a SLAC epoxy-dielectric design [1], used in the SLC Damping Rings. The kicker provides a 5 mrad kick to the 1.2 GeV beam. The kicked beam passes off-axis through two DR quadrupoles (QM6R1 and QM7R1), arriving at the entrance of the septum with a total horizontal offset of 23 mm. The blade of the septum is 5.3 mm thick, and the septum further deflects the beam by 28 mrad.

The original DR quadrupole QM7R1 had a 32 mm bore. The extracting beam at the location of QM7R1 has a nominal horizontal offset of 22.5 mm. Thus, the extracting beam passed through QM7R1 in one of its coil pockets, 6.5 mm *outside* its nominal bore. PRIAM simulation [2] of the magnetic field at this location indicated the presence of an undesired sextupole component [$K_2L \approx$ -46.6 m^{-2}] which could generate *x-y* coupling and growth of the projected vertical emittance if the beam passed vertically off-axis through this magnet. Given the 100:1 emittance ratio ($\varepsilon_x : \varepsilon_y$) in the DR, the projected vertical emittance for a beam with a 1 mm vertical offset in this magnet would be increased by a factor of 2-3. To remove this potential source of vertical emittance growth, QM7R1 was replaced in early 2009 with a 42 mm bore quadrupole, for which the simulated sextupole component of its field at the location of the extracting beam is negligible.

Simulations of the electric and magnetic fields in the kicker [3] also predict undesired quadrupole and sextupole components. Beam-based measurements using vertical orbit bumps through the kicker have confirmed the presence of these higher-order fields, at magnitudes consistent with the simulation. While the quadrupole field

can be compensated by rematching in EXT, the sextupole field [$K_2L \approx$ -15.3 m^{-2}] will generate 60% relative projected vertical emittance growth ($\Delta\varepsilon_y/\varepsilon_y$) for a beam with a 1 mm vertical offset in the kicker.

2.2.3.2.2 Inflector

The original design of the inflector incorporated a double-kicker jitter compensation scheme[4]. In this scheme, two identical kicker magnets, powered by a common pulser, are separated by a ±I transport matrix. Angular kick errors from the first kicker, possibly due to timing jitter or pulse shape abnormalities, are canceled by the second kicker. The optics of the inflector were therefore designed to provide a "pseudo –I" transform ($\Delta\mu_x = 180°$, $R_{21} \neq 0$) between the DR extraction kicker and a second identical kicker located at the end of the inflector. In addition, the optics of the inflector were designed to be symmetric about its midpoint in order to minimize dispersion. Finally, the physical dimensions of the Assembly Hall in which the ATF2 is housed required that the inflector be as short as possible, leading to rather strong transverse focusing. Figure 2 shows the optics of the inflector.

Strong quadrupoles (QF1X and QF6X) keep the maximum horizontal dispersion in the inflector < 60 cm. These same quadrupoles are used to correct horizontal dispersion errors at the exit of the inflector (where η and η' should be zero). The midpoint-symmetric optics of the inflector allows weak skew quadrupoles to be placed in two locations (near QF1X and QF6X) where the dispersion is largest, equal in magnitude and opposite in sign, and where $\beta_x = \beta_y$. These conditions allow the two skew quadrupoles (whose locations are indicated by vertical red dashed lines in Fig. 2), when powered with equal amplitude and polarity (the "Σ-knob"), to generate almost pure vertical dispersion and no net x-y coupling. Alternatively, when powered with equal amplitude and opposite polarity (the "Δ-knob"), pure x-y coupling and no net vertical dispersion is generated. As can be observed in the lower plot of Fig. 2, the strong focusing in the inflector causes almost all quadrupoles to be at a common betatron phase (modulo 180°). Thus anomalous vertical dispersion generated by quadrupole rotational errors in the inflector itself can mostly be corrected using the Σ-knob. To correct anomalous vertical dispersion that originates at a different phase (*i.e.* coming from the DR), additional corrections are required.

The 10° bends at the center of the inflector (BH1X and BH2X) are known to have sextupole components to their fields [$K_2L \approx$ -0.7 m^{-2}], due to their finite pole widths.
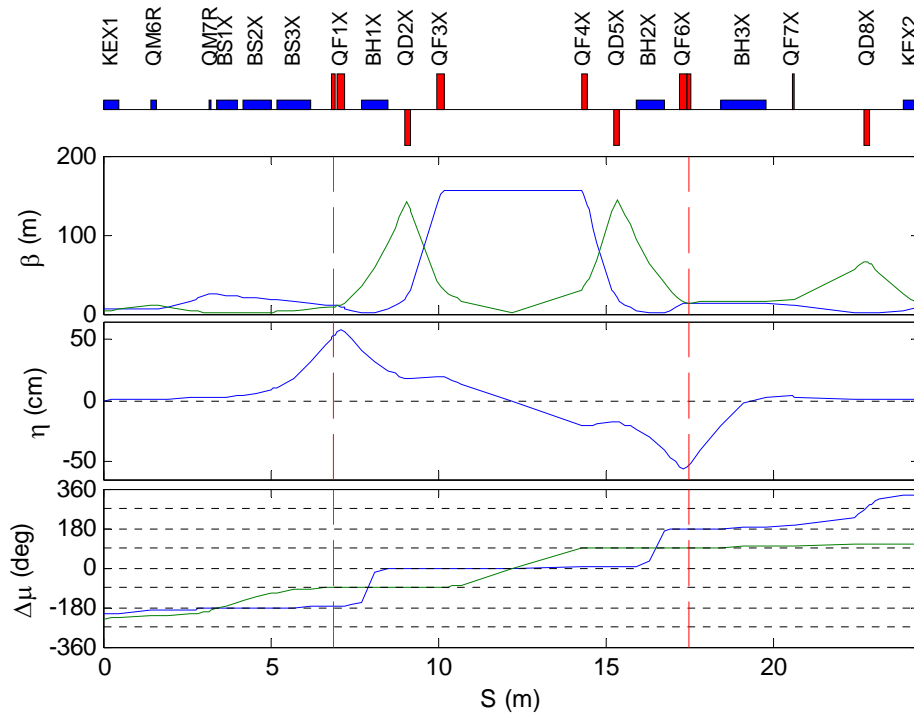
Figure 2: Optics of the inflector. Upper plot: Twiss β; middle plot: dispersion; lower plot: phase advance relative to the center of the inflector. (blue: *x*; green: *y*)

2.2.3.2.3 Coupling Correction Section

Immediately following the inflector is a short ILC-style *x*-*y* coupling correction section [5] containing four skew quadrupoles separated by appropriate betatron phase advance in each plane such that the effects of the skew quadrupoles are *orthonormal* (orthogonal and equally scaled). Orthogonality is achieved by separating the first and second and also the third and fourth skew quadrupoles by 90° of betatron phase advance in both planes, and separating the second and third skew quadrupoles by 180° in *x* and 90° in *y*. The first skew quadrupole controls the *x*-*y* phase (by definition here), the second controls the *x′*-*y′* phase, the third the *x′*-*y* phase, and the fourth the *x*-*y′* phase. The product $\beta_x\beta_y$ at each skew quadrupole is the same for all four skew quadrupoles, making their coupling effects equally scaled.

Figure 3 shows the optics of the coupling correction section.
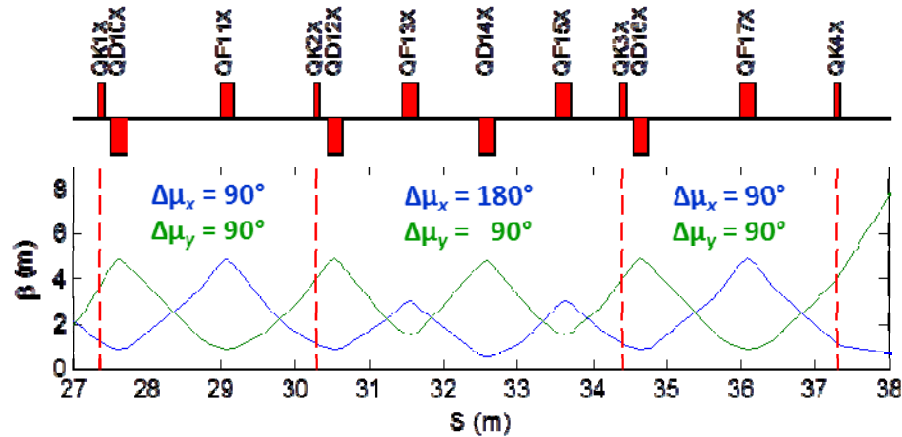
Figure 3: Optics of the coupling correction section. Skew quadrupole locations are indicated by vertical red dashed lines. (blue: *x*; green: *y*)

2.2.3.2.4 Emittance Diagnostic Section

Following the coupling correction section is the emittance diagnostic section. Because of tight space constraints, the optics for this system is a short, modified FODO array with 5 wire scanners [6] located at somewhat non-optimal positions. Each wire scanner is capable of measuring both *x* and *y* beam profiles, and each has "odd angle" wires (±10°) which in principle allow one to additionally determine the *x-y* correlation of the beam.

In addition to the wire scanners, four Optical Transition Radiation (OTR) monitors [7] provide fast single-shot beam spot measurements with full ellipse-fitting, allowing simultaneous measurement of the projected *x* and *y* spot sizes and the *x-y* tilt of the beam.

Beam sizes at the measurement locations for ATF2 emittances (ε_x = 2 nm, ε_y = 12 pm) in this nominally dispersion-free section range from 75 to 155 μm in *x*, and from 7 to 20 um in *y*.

Figure 4 shows the optics of the emittance diagnostic section.
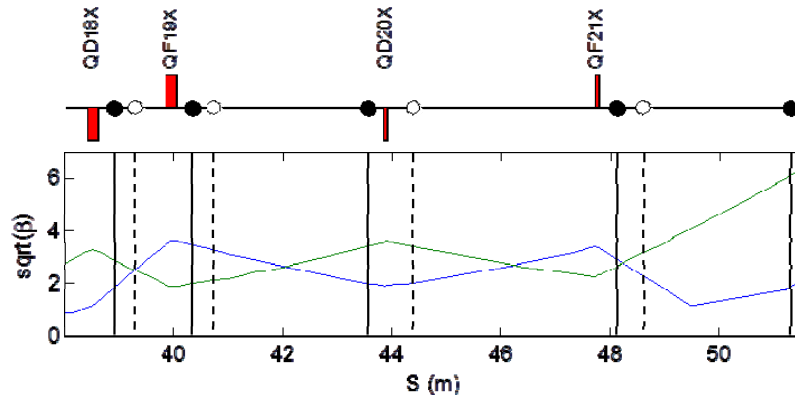
Figure 4: Optics of the emittance diagnostic section. Wire scanner locations are indicated by vertical solid lines; OTR locations are indicated by vertical dashed lines.

Figure 5 shows the "phase space coverage" of the wire scanners and the OTRs, showing that these measurement devices have sufficient betatron phase advance between them to allow for good reconstruction of the projected x and y phase space of the beam.
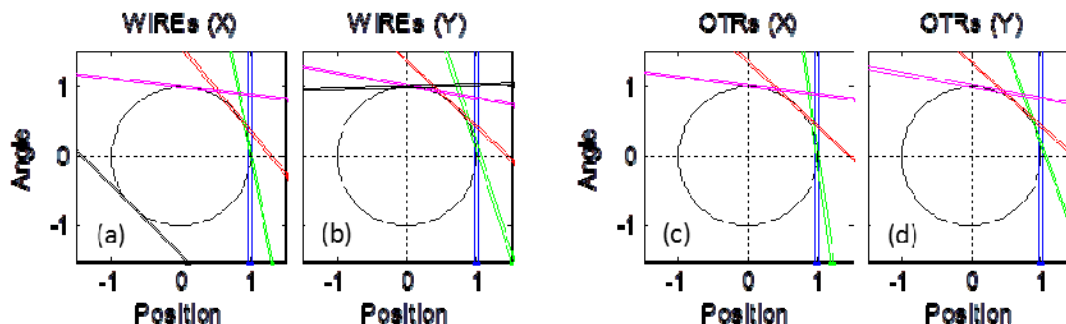
Figure 5: Normalized phase space coverage for wire scanners ((a) and (b)) and for OTRs ((c) and (d)). Colored lines represent measurement direction at each device mapped back to the first device of that type.

2.2.3.3 *Diagnostics*

2.2.3.3.1 BPMs

The EXT line has a total of 23 Beam Position Monitors (BPMs) installed. There are 12 stripline BPMs, located mainly in the inflector, with a single-shot resolution of ≈ 10 µm. LCLS-style readout electronics for these BPMs were installed in spring 2010 [8]. This style of readout electronics is insensitive to bunch charge. There are 9 C-band cavity BPMs [9], with sub-micron single-shot resolution. There are two button-type BPMs located near the septum, but for various reasons these have, in general, not been used.

2.2.3.3.2 Wire Scanners

The wire scanners use gold plated 10 µm tungsten wires. The estimated vertical measurement resolution is 1 µm. During a typical wire scan, a wire is stepped across the beam and a γ-ray detector measures the number of bremsstrahlung γs due to the interaction of the beam with the wire at each step. The beam size is determined by Gaussian fit to the measured beam profile, which normally consists of ≈ 50 points. At 1.5 Hz machine repetition rate, each scan takes ≈ 30 seconds. A minimal emittance measurement requires a scan at each of 3 locations; if statistical averaging is done (say 3 scans at each location), then a single plane emittance measurement can take 5 minutes or more (in practice, it takes much longer).

2.2.3.3.3 OTRs

Each of the OTRs uses a 1 cm diameter, 1 um thick Al target foil (or Al coated kapton). The minimum measurable spot size is ≈ 2 µm. The measurement resolution is on the order of a few percent of the measured spot size. Once the target is inserted into the beam, the OTR measures the projected x and y spot sizes and the beam tilt (x-y correlation) on every pulse. This single-shot measurement is insensitive to beam position jitter, and is very fast. Full emittance measurements (x and y, plus coupling

information), with statistical averaging can be made quickly. Since its installation and commissioning, the OTR system has become the beam size diagnostic of choice.

Figure 6 shows images from OTR0X during normal tuning.
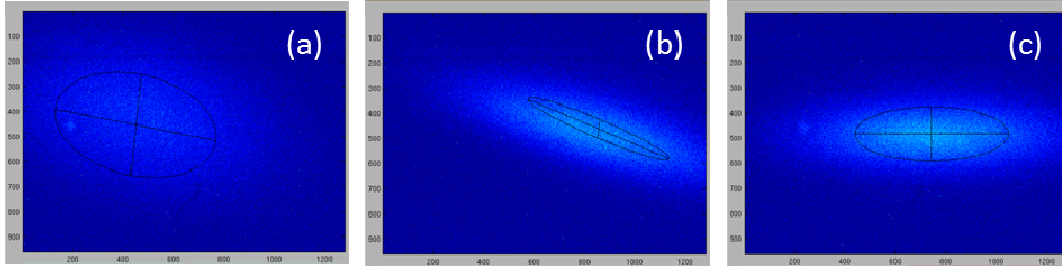
Figure 6: Images from OTR0X during normal tuning. (a): before any tuning; (b) after dispersion correction; (c) after coupling correction.

Figure 7 shows measured vertical spot sizes and vertical spot size predicted by an emittance measurement that combined data from both wire scanners and OTRs, illustrating the consistency of wire scanner and OTR measurements.
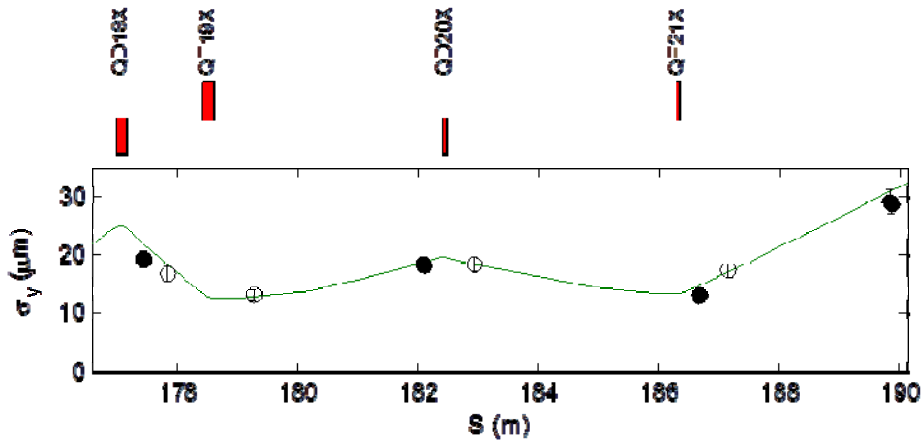
Figure 7: Vertical emittance reconstruction using both wire scanner and OTR data. Green line: vertical spot size predicted by emittance measurement; filled circles: wire

2.2.3.4 *Operational Experience*

2.2.3.4.1 Damping Ring Extraction

Vertical projected emittance growth between the DR and the EXT emittance diagnostic section has been observed since before the installation of ATF2, and has been studied extensively [10]. Vertically offset trajectories through anomalous sextupole fields generate x-y coupling and vertical dispersion. Some techniques that have been successfully used to minimize these effects are:

- keeping the beam vertically centered in the extraction kicker during DR tuning
- setting the kicker voltage to launch onto the proper trajectory through the septum (proximity to the septum blade is a suspected cause of emittance growth, and was a well known problem at the SLC Damping Rings)

- replacing DR quadrupole QM7R1 with a larger bore quadrupole
- correcting rotational errors of the strong bends just downstream of the septum

Lack of BPMs in the vicinity of the septum has made it difficult to find and maintain a "golden" trajectory through the extraction system. Back-propagation of observed anomalous coupling and vertical dispersion in the downstream systems to locate possible source(s) has been hampered by the (lack of) betatron phase advance in the inflector. Recent measurements [11] have suggested the possibility of a skew-sextupole field in the vicinity of BS3X as a source of anomalous vertical dispersion. Finally, the magnitude of the emittance growth is bunch charge dependent and much larger than would be expected from IBS effects in the DR.

2.2.3.4.2 Lattice Diagnostics

A Matlab GUI-based software package is used to measure the orbit response in the EXT line to the excitation of a selection of dipole correctors [12]. This Lattice Diagnostics measurement is performed at the start of each machine running period. The first-order optics of the EXT line is well understood, but this measurement allows us to quickly spot problems with the BPM readouts, such as sign flips in the BPM calibrations (rare). Given our understanding of the EXT line optics, automated model-based orbit correction is regularly used at the start of tuning.

Figure 8 shows a typical Lattice Diagnostics measurement.
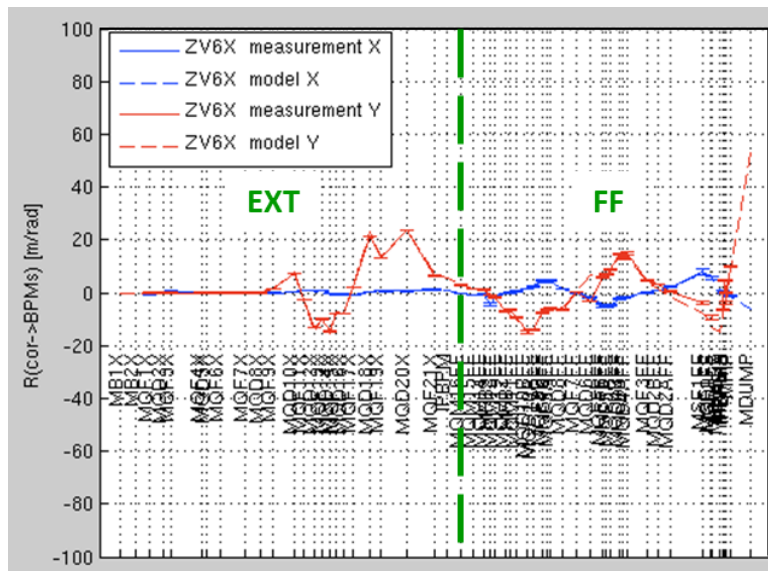
Figure 8: Vertical Lattice Diagnostics measurement (typical). Small x-y coupling effects in EXT from skew quadrupoles are amplified in FF (blue lines); the model prediction of these effects is spot-on.

2.2.3.4.3 Dispersion Correction

Dispersion measurement in the EXT line is performed by changing the energy of the beam in the DR and observing the response on BPMs in the EXT and FF lines. The energy change is accomplished by shifting the frequency of the DR RF. Typically the frequency is shifted by ±3 kHz (the nominal RF frequency is 714 MHz). The

momentum compaction of the DR (≈ 0.002) leads to a relative beam energy change of ±0.2 %.

The "leakage" dispersion in the nominally dispersion-free region downstream of the inflector is inferred by fitting a betatron oscillation to the observed BPM responses. This fit is then propagated backward to the DR and forward to the IP. Horizontal dispersion is corrected using a model-derived linear combination of the strengths of two inflector quadrupoles (QF1X and QF6X). Correction typically requires one or two iterations.

Figure 9 shows typical measured and fitted horizontal dispersion, before and after correction.
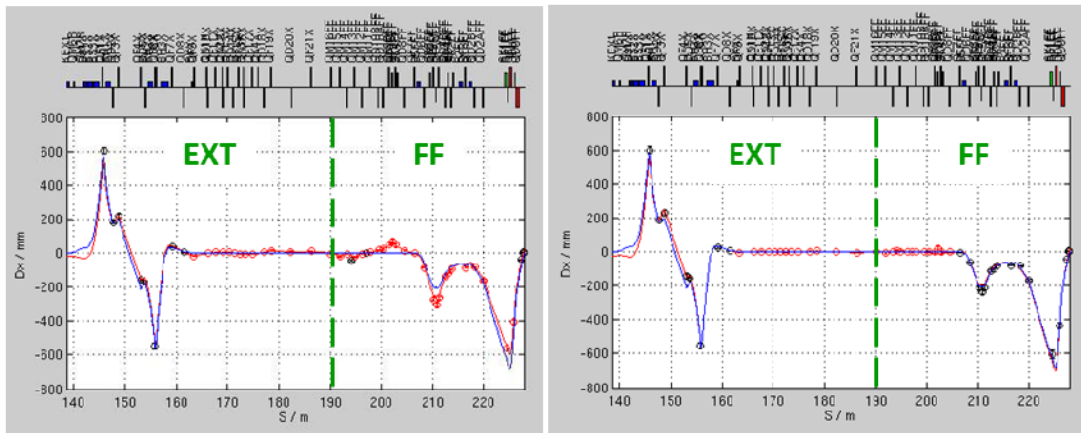
Figure 9: Horizontal dispersion measurements. Left: before correction; right: after correction.

The entire EXT line is nominally free of vertical dispersion, so any observed vertical dispersion is anomalous and is corrected to zero. Observed vertical dispersion comes in two "flavors": Final Doublet (FD) phase and IP phase.

Figure 10 shows simulated FD and IP phase vertical dispersion.

The original plan for vertical dispersion correction was to use the inflector skew quadrupole Σ-knob. Using this knob, one can correct either FD phase or IP phase dispersion, but not both. Since small vertical dispersion at the OTRs (IP phase) is necessary for accurate vertical emittance measurements, and small vertical dispersion through the Final Focus is necessary for making small spots at the IP, our normal tuning procedure involved using the Σ-knob to correct η_y at the OTRs, making emittance measurements and doing coupling correction, and then readjusting the Σ-knob to correct the FD phase η_y.

In order to alleviate this situation, we needed a vertical dispersion corrector which effectively acted out of phase with the Σ-knob. This can be accomplished by using a 3-corrector vertical orbit bump at the end of the inflector. Unfortunately, the presence of the second extraction kicker (with its strong sextpuole field) caused the orbit bump to introduce *x-y* coupling and blow up the vertical emittance of the beam. It was decided in early 2012 to remove the second kicker and replace it with a strong dipole corrector magnet. The measured increase in horizontal orbit jitter due to this was small, and was deemed acceptable from a cost-benefits standpoint. Once this was done, correction of both phases of vertical dispersion using a combination of Σ-knob and vertical bump became routine.

Figure 11 shows typical measured and fitted vertical dispersion before correction.

Figure 12 shows the results of sequential application of the Σ-knob and the vertical orbit bump to correct the vertical dispersion.
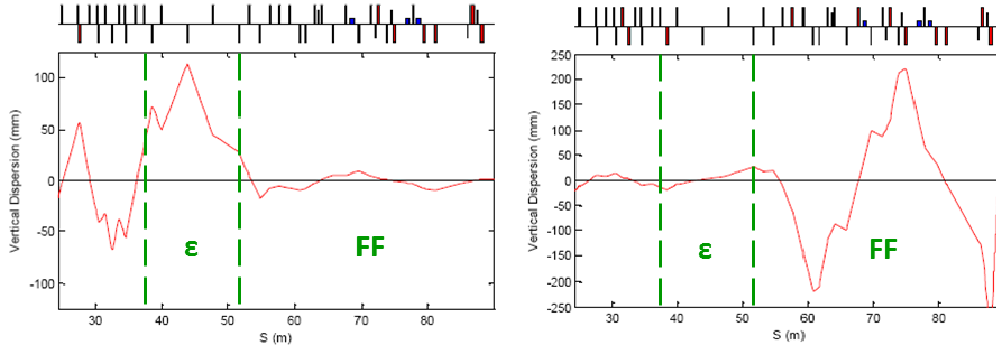
Figure 10: Simulated EXT/FF vertical dispersion. Left: "IP phase" ($\eta_y^* = 1$ mm, $\eta'_y^* = 0$); right: "FD phase" ($\eta_y^* = 0$, $\eta_y^* = 250$ mrad).
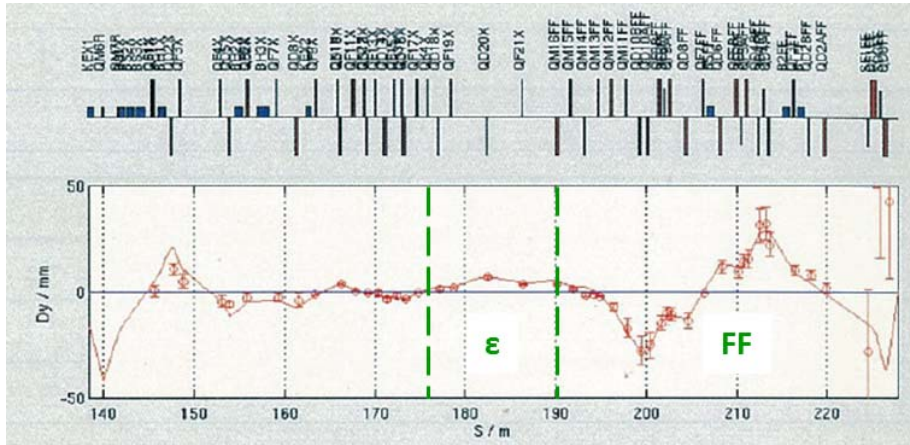
Figure 11: Typical measured vertical dispersion before correction (primarily FD phase). Red circles are measured data; red line is the fit to the data.
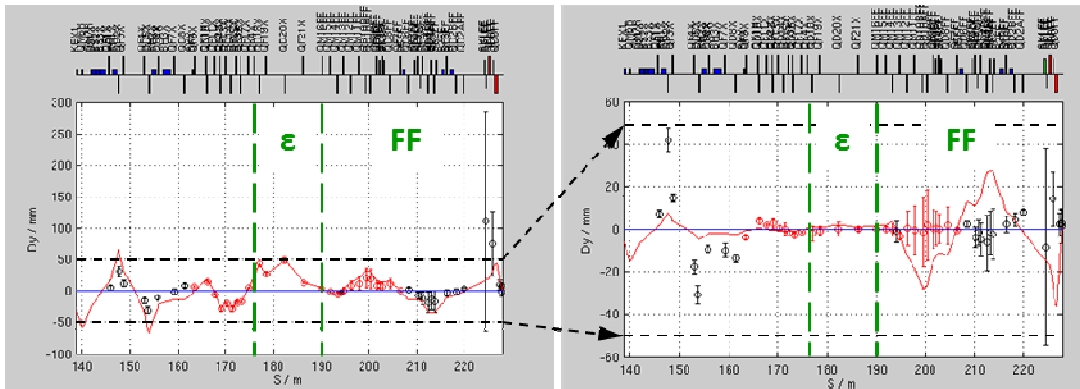
Figure 12: Vertical dispersion correction. Left: FD phase dispersion corrected with Σ-knob; right: IP phase dispersion corrected with vertical corrector bump.

2.2.3.4.4 Coupling Correction

The original plan for correction of any observed *x-y* coupling in the beam involved sequential minimization of the projected vertical emittance by scanning each of the four skew quadrupoles in the coupling correction section. Because of the designed orthonormality of the skew quadrupoles, each one would need to be scanned only once. Assuming 5-point scans, this process would require 20 emittance measurements. The amount of time needed to do this using the wire scanners was prohibitive. Fortunately, with the advent of the multi-OTR system, emittance measurements became fast enough that the sequential scan technique could be used. Additionally, it was quickly noted that the ellipse-fitting capability of the OTR beam measurement software provides a direct measurement of the *x-y* tilt of the beam at each OTR location. Given our ability to accurately model the optics of this system, it is possible to compute a simultaneous correction of the beam tilts at all four OTRs using the four skew quadrupoles; this became known as the "response-matrix" correction technique [13]. Theoretically, the betatron phase advance through the emittance diagnostic system is insufficient for measuring all four phases of coupling. However, simulations of response-matrix correction of arbitrary incoming coupling, with an initial uncorrected projected vertical emittance of 100 pm, predict that it will be successful in correcting almost all phases of incoming coupling [14].

A recent development has been the use of the inflector skew quadrupole Δ-knob for coupling correction. Although this is a single-phase correction (primarily *x'-y* at the IP), it has been effective at removing the observed beam tilt at the OTRs. One advantage of this technique is that the strengths of the inflector skew quadrupoles needed for a given coupling correction are only ≈ 10% of strengths of the coupling correction section skew quadrupoles needed for the same correction. Another advantage is that the coupling correction skew quadrupoles are then free to be used for IP tuning.

2.2.3.4.5 Matching

Beta-matching from the EXT line into the ATF2 Final Focus was originally intended to be accomplished using 6 bipolar quadrupoles at the beginning of the Final Focus. Some of these quadrupoles are quite strong by design, as they must blow up the beta functions from average values of < 10 m in the EXT emittance diagnostic section to several kilometers in the Final Focus system.

Because these quadrupoles are so strong, setting up the launch into the FF requires very careful steering through the matching section, and compensation of the steering downstream if the launch is less than perfect. Under these conditions, changing the strengths of the matching quadrupoles to compensate for incoming mismatches can lead to trajectory changes downstream that inevitably generate spot size growth at the IP.

Also, the settings of these quadrupoles are used to define each distinct *FF optics*, leaving the remainder of the FF magnets set to their nominal design values. For instance, the "BX10BY1" optics has $\beta_x^* = 4$ cm (10 times nominal), and $\beta_y^* = 0.1$ mm (1 times nominal). If, instead of matching from EXT to FF using the quadrupoles of the matching section, we matched *into* the matching section using EXT quadrupoles, then the strengths of the matching quadrupoles will remain constant for any given FF optics. This has distinct advantages when switching from one FF optics to another.

For these reasons we now use quadrupoles in the inflector to do beta-matching. With the removal of the second kicker, the pseudo –I constraint between the two kickers is also removed, which means we have enough quadrupoles in the inflector to do beta-

matching in both planes while holding the dispersion fixed. Additional advantages to using inflector quadrupoles for beta-matching are: the match into the coupling correction section is maintained, and we can use our emittance diagnostics to confirm the success of the matching.

Figure 13 shows beta-matching results. In normalized phase-space, a matched beam will be circular with BMAG = 1. Dashed unit circles represent matched beams with nominal emittance.

2.2.3.5 *Lessons Learned*

Experience to date operating and tuning the ATF/ATF2 EXT line has provided some (perhaps obvious) lessons for future systems such as this:

- tolerances on magnet field quality must be carefully evaluated and clearly specified before fabrication begins … tuning devices and schemes for using them must be quickly developed for sub-tolerance magnets and in place for commissioning
- diagnostic and correction devices with proper betatron phase advance between them must be included in the design … if needed, split magnets in order to place these devices optimally
- beam profile measurement devices (such as OTRs) which provide single-shot measurement of the entire x-y beam matrix are preferred
- the response-matrix method for correction of x-y coupling represents a big improvement in the efficiency of coupling correction
- orbit/dispersion/coupling devices and schemes must be capable of correcting arbitrary phases of incoming errors … not just errors in the systems which they were designed for
- diagnostic systems are best located downstream of correction devices/systems in order to allow verification of corrections
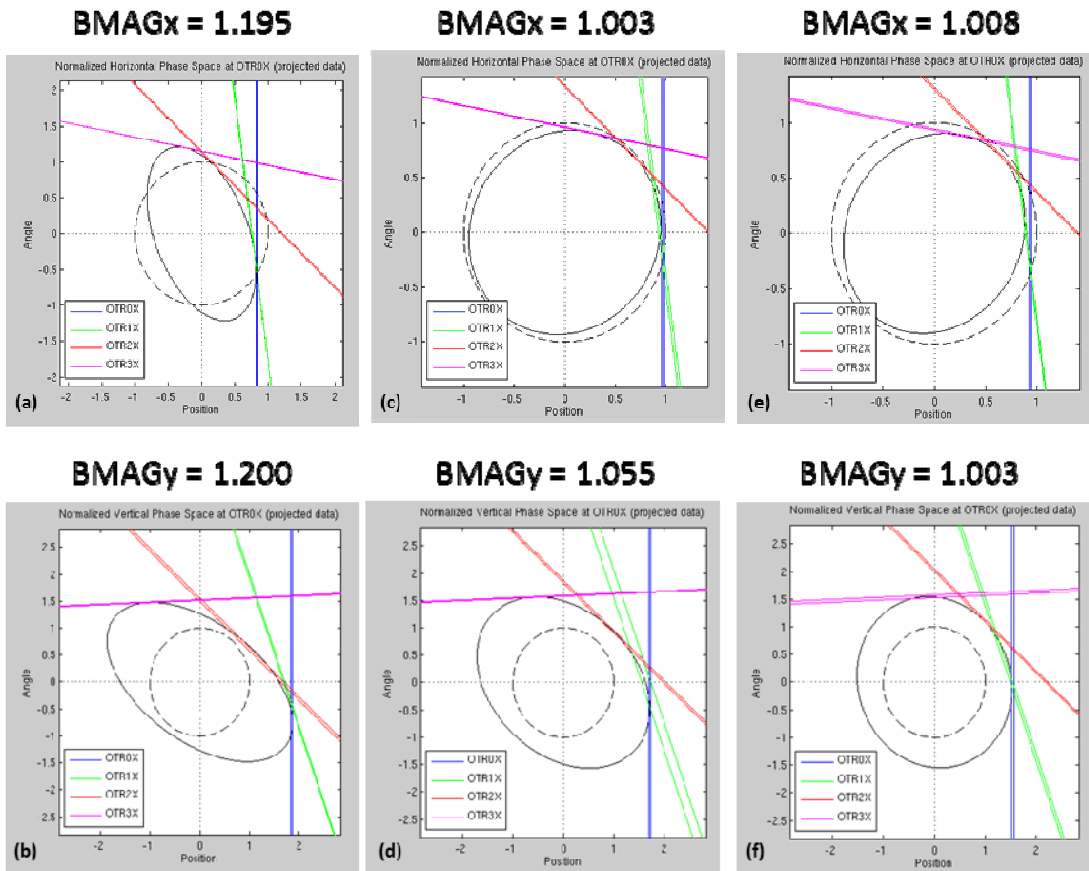
Figure 13: Normalized phase-space depiction of beta-matching results. (a)(b): before matching; (c)(d): after first matching iteration; (e)(f): after second iteration. (top: *x*; bottom: *y*)

2.2.3.6   *References*

1. T. Mattison, R. Cassel, A. Donaldson, and G. Gross, "Fast and reliable kicker magnets for the SLC damping rings", proceedings of the 1995 Particle Accelerator Conference, Piscataway, New Jersey (1995).
2. P. Bambade, G. Le Meur, F. Touze, and M. Masuzawa, "Proposed replacement of QM7 by TOKIN 3581", presented at the 7th ATF2 Project Meeting, Tsukuba, Japan (2008).
3. C. Pappas [SLAC] private communication (May 2005).
4. T. Imai, K. Nakai, H. Hayano, J. Urakawa, and N. Terunuma, "Double Kicker system in ATF", proceedings of the 2000 Linac Conference, Monterey, California (2000).
5. T. Raubenheimer, *et al*, "Zeroth order design report for the Next Linear Collider", SLAC-R-474 (May 1996).
6. H. Hayano, "Wire scanners for small emittance beam measurement in ATF", proceedings of the 2000 Linac Conference, Monterey, California (2000).
7. J. Alabau-Gonzalvo, C. Gutierrez, A. Faus-Golfe, J. Garcia-Garrigos, J. Cruz, D. McCormick, G. White, and M. Woodley, "Optical Transition Radiation System for ATF2", proceedings of the 2nd International Particle Accelerator Conference (IPAC 2011), San Sebastian, Spain (2011).
8. G. White, "Stripline BPM Electronics Upgrade Report", presented at the 10th ATF2 Project Meeting, Tsukuba, Japan (2010).
9. A. Aryshev, Y. Honda, N. Terunuma, J. Urakawa, F. Cullinan, N. Joshi, A. Lyapin, and

A. Heo, "Cavity Beam Position Monitor System for ATF2", proceedings of the 2nd International Particle Accelerator Conference (IPAC 2011), San Sebastian, Spain (2011).

10. M. Alabau, A. Faus-Golfe, P. Bambade, J. Brossard, G. Le Meur, C. Rimbault, and F. Touze, "Study of Abnormal Vertical Emittance Growth in ATF Extraction Line", proceedings of the 11th European Particle Accelerator Conference (EPAC 08), Genoa, Italy (2008).

11. M. Woodley, "Emittance Measurements and Related Experimental Results", presented at the 15th ATF2 Project Meeting, Tsukuba, Japan (2013).

12. Y. Renier, "Optics Modeling and BPM Status", presented at the 9th ATF2 Project Meeting, Tsukuba, Japan (2009).

13. J. Alabau-Gonzalvo, C. Blanch Gutierrez, A. Faus-Golfe, J. Garcia-Garrigos, J. Resta-Lopez, J. Cruz, D. McCormick, and G. White, "Optics and Emittance Studies using the ATF2 Multi-OTR System", proceedings of the 3rd International Particle Accelerator Conference (IPAC 2012), New Orleans, Louisiana (2012).

14. E. Marin Lacoma, "Study on Coupling Correction and Emittance measurements", presented at the 15th ATF2 Project Meeting, Tsukuba, Japan (2013).

2.2.4   Beam Size Tuning at ATF2 Virtual Interaction Point

Toshiyuki Okugi
High Energy Accelerator Research Organization (KEK), Japan
Mail to: toshiyuki.okugi@kek.jp

2.2.4.1   *Introduction*

I will explain the beam size tuning for ATF2 virtual interaction point (IP) in this session. The beam optics of ATF2 final focus beamline is based on the principle of local chromaticity correction [1,2]. The method which is adopted for the ILC FF design [3] and which is also the only practical method to focus multi-TeV beams – the CLIC final focus system is based on the same principle [4].

2.2.4.2   *Beam Size Monitor for ATF2 IP Beam Size Tuning (IP-BSM)*

In order to perform to make the electron beam less than 40nm, it is very important to realize the beam size monitor to be able to measure such a small beam size. The idea of the nanometer scale beam size monitor was proposal by T. Shintake [5], and the beam size monitor demonstrated a beam size measurement of 70nm at the SLAC FFTB beamline during the 1990s [6]. The beam size measurement system was modified and installed to ATF2 virtual collision point (IP) and used for the beam size measurement in ATF2 IP. The beam size monitor for ATF2 IP (IP-BSM) uses a fringe pattern formed by two interfering laser beams. The laser fringe pitch of the IP-BSM laser was defined by the laser wavelength and the collision angle of two laser paths as

$$d = \frac{\lambda}{2\sin(\theta/2)} \tag{1}$$

Here λ is the laser wavelength and θ is the collision angle. The fringe pattern transversely overlaps the electron beam. The resulting Compton scattered photons are measured downstream of the interaction point. The modulation depth of the signal is written as a function of laser collision angle and electron beam spot size as

$$M = C\left|\cos\theta\right|\exp\left[-2\left(k_y\sigma_y\right)^2\right] \quad , \quad k_y = \frac{\pi}{d} \tag{2}$$

Hence the C express the contrast reduction of the laser fringe pattern. The reduction of the laser fringe contrast is generated by the worse laser spatial coherency, mismatch of the two laser overlap and so on. Since the modulation depth of the Compton signal is also reduced by C, we called the factor C to the modulation reduction factor. From the Eq. (2), the beam size was written as a function of the modulation depth as

$$\sigma_y = \frac{1}{k_y}\sqrt{\frac{1}{2}\ln\left(\frac{C\left|\cos\theta\right|}{M}\right)} \quad , \tag{3}$$

and we can evaluate the electron beam spot size from the measured modulation depth by using Eq. (3). We can measure the modulation depth of the Compton signal by measuring the strength of the Compton signal for various relative beam positions with respect to the laser fringe. In ATF2, we change the relative beam positions by changing the laser phase of one laser path. Furthermore, since we can measure smaller beam size for smaller laser fringe pitch, the laser wavelength of ATF2 IP-BSM was changed from 1064nm of FFTB wavelength to 532nm. Furthermore, we prepared 3 laser collision modes (2-8degree mode, 30degree mode, 174degree mode) to make the dynamic range of ATF2 IP-BSM wide [7]. The dynamic ranges of FFTB and ATF2 are shown in Fig.1.
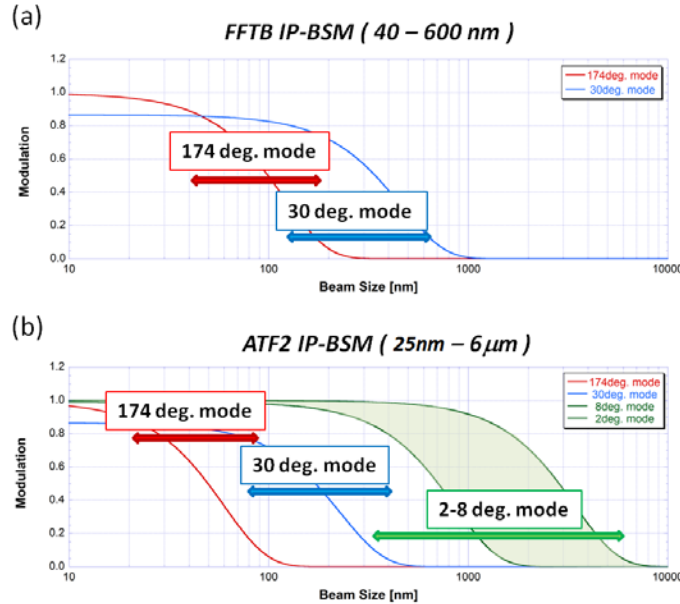
Figure 1: Comparison of the dynamic ranges of the IP beam size monitors (a) of FFTB and (b) of ATF2.

2.2.4.3 *Linear Knob Tuning Method in ATF2 Final Focus Beam Line*

The IP vertical beam size is sensitive to the IP beam waist offset, the IP vertical dispersion and the amount of xy coupling at IP. Therefore, the IP vertical beam size can be expressed as

$$\sigma_y^2 = \varepsilon_y\beta_y^* + C_{AY}^2 P_{AY}^2 + C_{EY}^2 P_{EY}^2 + C_{31}^2 P_{31}^2 + C_{32}^2 P_{32}^2 + \sigma_{y,nonlinear}^2 \tag{4}$$

Here P_{AY} is an amplitude of beam waist knob, and C_{AY} is the sensitivity. P_{EY} is an amplitude of vertical dispersion knob, and C_{EY} is the sensitivity. P_{31}, P_{32} are amplitudes of xy coupling knobs $\langle xy \rangle, \langle x'y \rangle$, and C_{31}, C_{32} are the sensitivities. The $\sigma_{y,nonlinear}$ is the IP beam size contribution by nonlinear field. By putting the Eq. (4) to Eq. (2),

$$M = C \left| \cos\theta \right| \exp\left[-2k_y^2 \left(\varepsilon_y \beta_y^* + \sigma_{y,nonlinear}^2 \right) \right]$$
$$\times \exp\left[-2\left(k_y C_{AY} \right)^2 P_{AY}^2 \right]$$
$$\times \exp\left[-2\left(k_y C_{EY} \right)^2 P_{EY}^2 \right]$$
$$\times \exp\left[-2\left(k_y C_{31} \right)^2 P_{31}^2 \right]$$
$$\times \exp\left[-2\left(k_y C_{32} \right)^2 P_{32}^2 \right] \quad . \tag{5}$$

The 1st line of Eq. (5) is the maximum amplitude of the modulation depth. The maximum modulation depth is determined by the minimum beam size to be able to focus by the linear knob tuning. The 2nd to 5th lines of Eq. (5) are the response of the linear knobs. We optimize P_{AY}, P_{EY} and P_{32} to make the modulation depth maximum at the IP beam size tuning [8].

We have 5 sextupole magnets ($SF6$, $SF5$, $SD4$, $SF1$, $SD0$) in ATF2 final focus beamline, and the positions of all the sextupole magnets can be controlled by using the magnet movers. When we change a position of sextupole magnet horizontally, a quadrupole field is generated. The generated quadrupole field is proportional to the horizontal offset, and the quadrupole fields change horizontal and vertical beam waist positions W_x, W_y, a horizontal dispersion η_x and the derivative η'_x at IP. When we choose the appropriate horizontal offsets of the sextupole magnets to be orthogonal to change only to W_x, W_y, η_x and η'_x, we can make the knobs to tune linear optics components of P_{AX} (W_x knob), P_{AY} (W_y knob), P_{EX} (η_x knob) and P_{EPX} (η'_x knob).

When we change a position of sextupole magnet vertically, a skew quadrupole field is generated. The generated skew quadrupole field is proportional to the vertical offset, and the field is changed a vertical dispersion η_y, the derivative η'_y and IP xy coupling components, especially $\langle x'y \rangle$. When we choose the appropriate vertical offsets of sextupole magnets to be orthogonal to change only to η_y, η'_y and $\langle x'y \rangle$, we can make the knobs to tune linear optics components of P_{EY} (η_y knob), P_{EPY} (η'_y knob) and P_{32} ($\langle x'y \rangle$ knob) .

The IP beam size contribution of P_{31} is difficult to change by the sextupole position changes for their small sensitivities of $\langle xy \rangle$. Therefore, the minimization of P_{31} is performed by changing the strength of the skew quadrupoles in the injection beamline. When we change a strength of skew quadrupole magnet, 4 IP xy coupling parameters $\langle xy \rangle, \langle x'y \rangle, \langle xy' \rangle$ and $\langle x'y' \rangle$ are changed. When we choose the appropriate strengths of skew quadrupole magnets to be orthogonal to change only to $\langle xy \rangle, \langle x'y \rangle, \langle xy' \rangle$ and $\langle x'y' \rangle$, we can make the knobs to tune linear optics components of P_{31}, P_{32}, P_{41} and P_{42}. Hence, we have two P_{32} knobs. One is made by changing the sextupole positions in the final focus beamline, and another is made by changing the skew quadrupole strengths in the injection beamline. However, we use the P_{32} knob of sextupole position changes in order to avoid the hysteresis of the magnets. Therefore, we use only P_{31} knob of skew quadrupole magnets in the injection beamline.
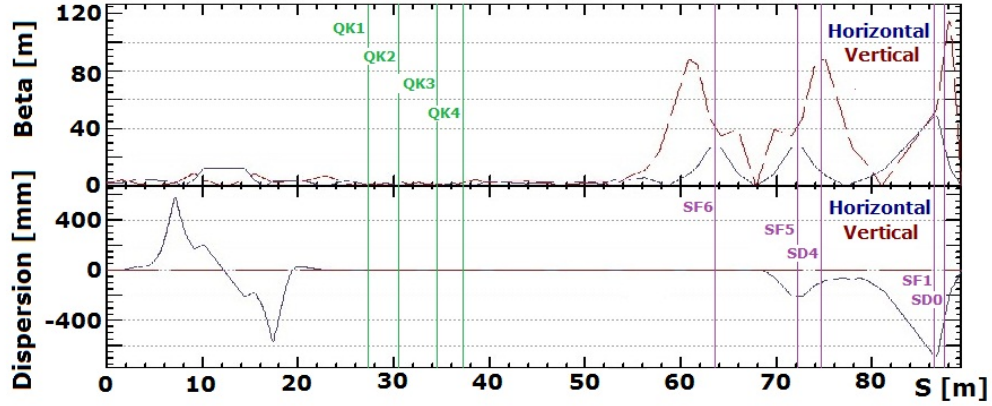
Figure 2: Beam optics of ATF2 beamline. Skew quadrupoles in the injection line and sextupoles in the final focus beamline are shown in the figure.

2.2.4.4 *2nd Order Optics Tuning Method in ATF2 Final Focus Beam Line*

2.2.4.4.1 2nd Order Optics Knob to Correct Normal Sextupole Field Errors

The beamline have possibilities to have 2nd order aberrations by sextupole field errors of magnets, even though we already set the strength of final focus sextupole magnet to be cancelled the aberrations [2]. Therefore, we prepare the tuning knobs to correct the 2nd order aberration by the sextupole field errors in the beamline. When we change a strength of sextupole magnet, IP horizontal and vertical positions are changed as a function of the sextupole positions Δx, Δy and the momentum offset δ by

$$\Delta x_{IP} = \frac{R_{12}\Delta K_{2N}}{2}\left(\Delta x^2 + 2\eta_x \Delta x\delta + \eta_x^2\delta^2 - \Delta y^2\right) \tag{6}$$

$$\Delta y_{IP} = R_{34}\Delta K_{2N}\left(\Delta x\Delta y + \eta_x \Delta y\delta\right) \tag{7}$$

Since the final focus sextupoles are located at the large beta function, the horizontal and vertical sextupole positions Δx and Δy are strongly correlated to the horizontal and vertical IP beam divergences. Therefore, IP horizontal and vertical beam size growths by the sextupole strength change can be express as

$$\Delta\sigma_x^2 = \Delta K_{2N}^2\left(X_{22}^2\left\langle x'^2_{IP}\right\rangle^2 + X_{26}^2\left\langle x'_{IP}\,\delta\right\rangle^2 + X_{66}^2\left\langle\delta^2\right\rangle^2 + X_{44}^2\left\langle y'^2_{IP}\right\rangle^2\right) \tag{8}$$

$$\Delta\sigma_y^2 = \Delta K_{2N}^2\left(Y_{24}^2\left\langle x'_{IP}\,y'_{IP}\right\rangle^2 + Y_{46}^2\left\langle y'_{IP}\,\delta\right\rangle^2\right) \quad . \tag{9}$$

We only have 5 sextupole magnets (*SF6*, *SF5*, *SD4*, *SF1*, *SD0*) in ATF2 final focus beam line (see Fig.2). On the other hand, we have 6 parameters to affect IP horizontal and vertical beam size growths. Therefore, we ignore X_{44} to make the ATF2 IP beam size tuning knobs, because IP horizontal beam size growth of X_{44} is smaller than others. We choose the appropriate strength changes of sextupole magnets to be orthogonal to change only to X_{22}, X_{26}, X_{66}, Y_{24} and Y_{46}, we can make the tuning knobs to correct sextupole field errors. We optimize Y_{24} knob (geometrical aberration knob) and Y_{46} knob (chromaticity knob) to minimize the IP vertical beam size for IP beam size tuning. Fig.3 shows the sextupole field errors of quadrupole magnets by magnetic field measurements. The tolerances of the sextupole field errors with/without the 2nd order knob tuning also shown in Fig.3. The tolerance is defined by 5% of IP vertical beam size growth. You can find that the tolerance of normal sextupole field errors are

increased by using the 2nd order knobs, and the measured sextupole field errors were within the tolerances after the 2nd order knob tuning.
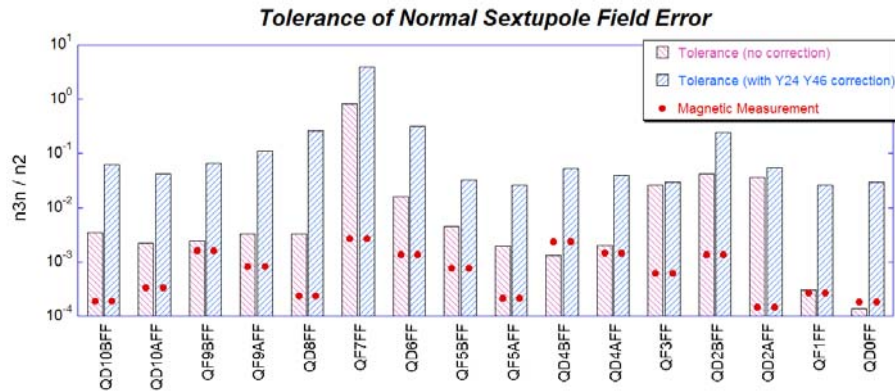
Figure 3: Tolerance of the normal sextupole field errors for the quadrupole magnets in the ATF2 beamline and the measured sextupole field errors.

2.2.4.4.2 2nd Order Optics Knob to Correct Skew Sextupole Field Errors

Since the skew sextupole errors for QF5B, QF5A and QD4B are comparable to those by the magnetic field measurements, we put a skew sextupole magnet in between QF5A and QD4B to compensate the skew sextupole field errors in 2011 [9]. We tried to make the IP beam size small by using the skew sextupole magnet several times at 2012 beam operation. The results are shown in Fig.4. We expected the optimum strength of the skew sextupole magnet should be 1-2A. In actually, however, the magnet strength to make the IP-BSM modulation maximum was around 15A of the maximum magnet strength. It suggested that there were strong unexpected skew sextupole field errors in the beamline. Therefore, we installed 3 more skew sextupole magnets In order to correct the skew sextupole field error at August 2012. We have totally 4 skew sextupole magnets (*SK1-SK4*) in the beam line [10].
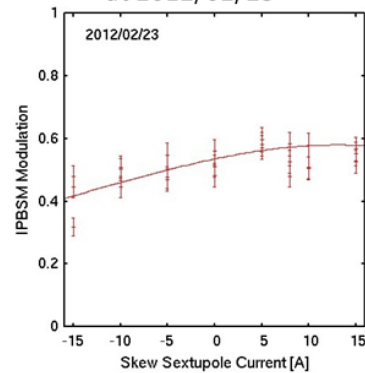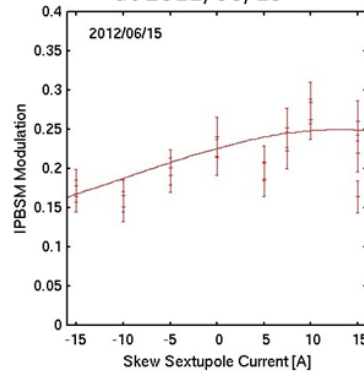
Figure 4: The IPBSM modulation dependence of the strength of the skew sextupole magnet located in the ATF2 beamline.
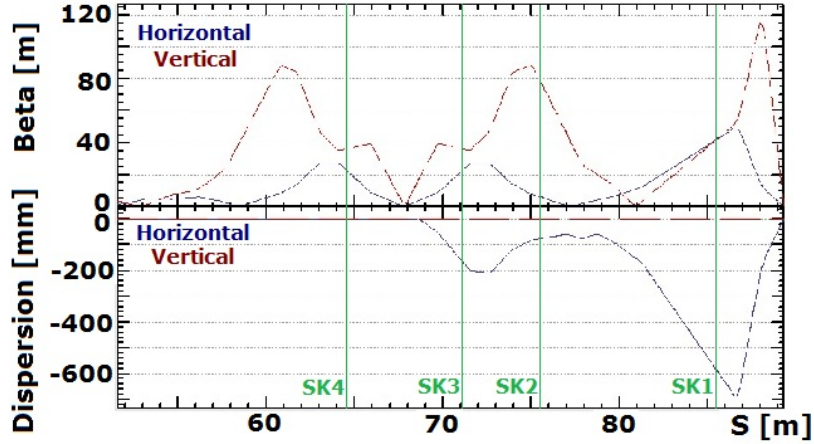
Figure 5: The skew sextupole magnet arrangement in ATF2 beamline.

When we change a strength of skew sextupole magnet, the IP vertical position is changed as a function of the skew sextupole positions Δx, Δy and the momentum offset δ by

$$\Delta y_{IP} = \frac{R_{34}\Delta K_{2S}}{2}\left(\Delta x^2 + 2\eta_x\Delta x\delta + \eta_x^2\delta^2 - \Delta y^2\right) \qquad (10)$$

When we put the skew sextupole magnet to the large beta function in the beam line, the horizontal and vertical positions at the sextupoles Δx and Δy are strongly correlated to the IP divergence. Therefore, the vertical beam size growth by the sextupole strength change can be express as

$$\Delta\sigma_y^{*2} = \Delta K_{2S}^2\left(Y_{22}^2\left\langle x'^2_{IP}\right\rangle^2 + Y_{26}^2\left\langle x'_{IP}\,\delta\right\rangle^2 + Y_{66}^2\left\langle\delta^2\right\rangle^2 + Y_{44}^2\left\langle y'^2_{IP}\right\rangle^2\right) \qquad (11)$$

The arrangement of the skew sextupole magnets is shown in Fig.5. The *SK1* and *SK3* are located to be sensitive to Y_{22}, Y_{26}, Y_{66}. *SK2* is to Y_{44}, and *SK4* is to Y_{22}. When we choose the appropriate strength changes of the skew sextupole magnets to be orthogonal to be changed only to Y_{22}, Y_{26}, Y_{66} and Y_{44}, we can make 4 independent tuning knobs to tune the skew sextupole field errors.

Fig.6 shows the skew sextupole field errors of quadrupole magnets by magnetic field measurements. The tolerances for the skew sextupole field errors 1) without 2nd order knob correction, 2) with the correction by single skew sextupole and 3) with the correction by 4 skew sextupoles are also shown in Fig.6. The tolerance is defined by 5% of IP vertical beam size growth as well as the correction of normal sextupole field errors. You can find that the tolerances of the skew sextupole field errors are increased by using the 4 skew sextupole magnets, especially for the final doublet (*QF1* and *QD0*). Furthermore, we have one more benefit of the skew sextupole magnets in the final focus beamline. We can investigate the source of the skew sextupole field by analyzing the corrected field distribution of 4 skew sextupole magnets.
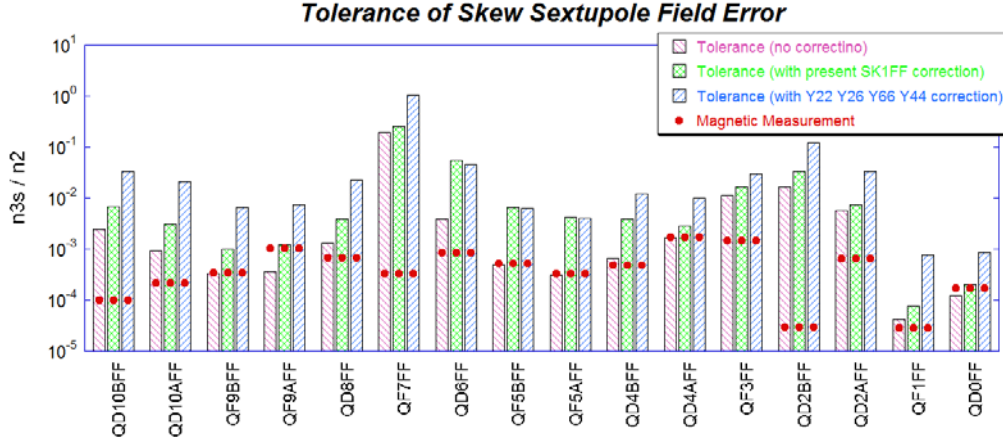
Figure 6: Tolerance of the normal sextupole field errors for the quadrupole magnets in ATF2 final focus beam line and the measured sextupole field errors.

2.2.4.4.3 Simulation of the IP Beam Size Tuning

The performance of IP beam size tuning knobs to correct the linear optics and 2nd order aberrations was simulated by using a particle tracking simulation SAD [11]. In the simulation, the parameters defined by linear optics can be evaluated by the IP particle position and angle distribution to

$$\alpha_y = -\left\langle (y-\langle y \rangle)(y'-\langle y' \rangle) \right\rangle \big/ \varepsilon_y \tag{12}$$

$$\eta_y = \left\langle (y-\langle y \rangle)(\delta-\langle \delta \rangle) \right\rangle \big/ \left\langle (\delta-\langle \delta \rangle)^2 \right\rangle \tag{13}$$

$$R_{31} = \left\langle (y-\langle y \rangle)(x-\langle x \rangle) \right\rangle \big/ \left\langle (x-\langle x \rangle)^2 \right\rangle \tag{14}$$

$$R_{32} = \left\langle (y-\langle y \rangle)(x'-\langle x' \rangle) \right\rangle \big/ \left\langle (x'-\langle x' \rangle)^2 \right\rangle . \tag{15}$$

The 2nd order terms are also evaluated with the particle distributions at IP to

$$Y_{22} = \left\langle (y-\langle y \rangle)(x'-\langle x' \rangle)^2 \right\rangle \big/ \left\langle (x'-\langle x' \rangle)^2 \right\rangle \tag{16}$$

$$Y_{24} = \left\langle (y-\langle y \rangle)(x'-\langle x' \rangle)(y'-\langle y' \rangle) \right\rangle \big/ \sqrt{\left\langle (x'-\langle x' \rangle)^2 \right\rangle \left\langle (y'-\langle y' \rangle)^2 \right\rangle} \tag{17}$$

and so on. The simulation results are shown in Fig.6. Each knob is normalized to 100nm of IP vertical beam size contribution, when we set the knob amplitudes to 1. The vertical axis is the IP vertical beam size contributions when the knob amplitude is changed. We found that the linear and 2nd order knobs work independently from the simulation.
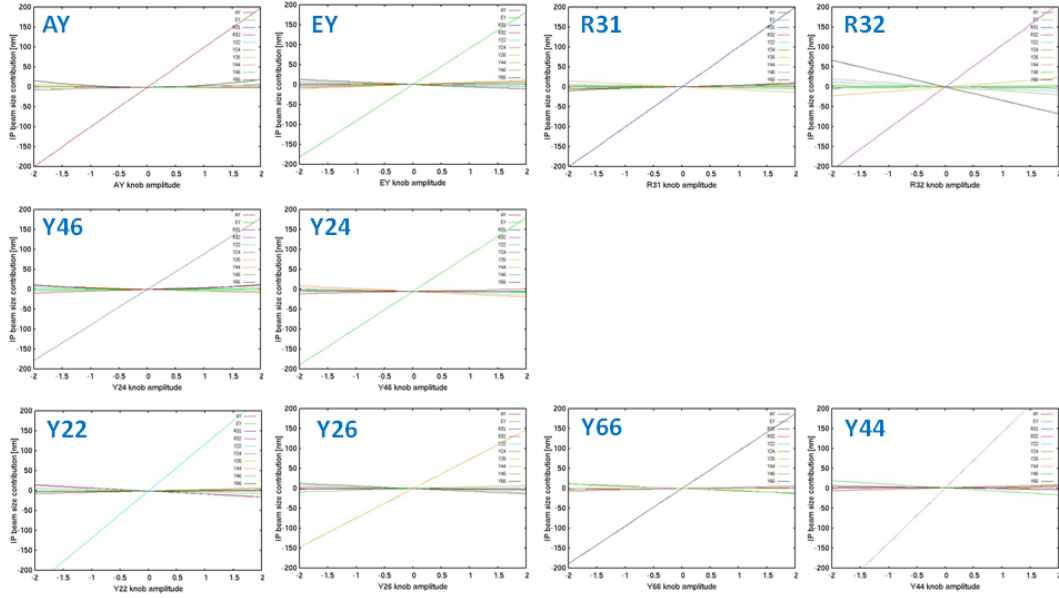
Figure 7: Simulation result of linear and 2nd order knob effect to IP beam size.

2.2.4.5 *Beam Size Tuning in the ATF2 Final Focus Beam Line*

2.2.4.5.1 IP Beam Size Tuning Procedures with Linear and 2nd Order Knobs

In generally, IP vertical beam size can be expanded as

$$
\begin{aligned}
\sigma_y^2 = {} & \varepsilon_y \beta_y^* + C_{AY}^2 P_{AY}^2 + C_{EY}^2 P_{EY}^2 + C_{31}^2 P_{31}^2 + C_{32}^2 P_{32}^2 \\
& + C_{322}^2 Y_{22}^2 + C_{324}^2 Y_{24}^2 + C_{326}^2 Y_{26}^2 + C_{344}^2 Y_{44}^2 + C_{346}^2 Y_{46}^2 + C_{366}^2 Y_{66}^2 \\
& + \sigma_{y,6\,pole}^2 + \sigma_{y,8\,pole}^2 + \sigma_{y,10\,pole}^2 + \sigma_{y,12\,pole}^2 + ...
\end{aligned}
\tag{18}
$$

The IP beam size contribution of 1st line in Eq. (22) can be corrected with the linear knobs, and the contribution of 2nd line can be corrected with the 2nd order aberration knobs. Therefore, we can correct the IP beam size contribution of the 1st and 2nd line in Eq. (22) by using ether linear or 2nd order aberration knobs. However, the 3rd line of Eq. (22) is the IP beam size contribution of more than 3rd order multipole field errors, and we don't have the IP beam size tuning knobs for more than 3rd order multipole field errors. However, we can reduce the effects of the higher order multipole field errors by decreasing the beam sizes at the quadrupole and sextupole magnets. Since the phase advances for most of magnets are separated by $\pi/2$ from IP, we can control the beam size at the quadrupoles by changing β_x^*. In present ATF2 operation, we set to $\beta_x^* = 4$cm (10 times larger than the original design [4]) in order to reduce the effects of the higher order multipole fields.

Furthermore, since we have been observed the strong intensity dependence of IP beam size by corrective effects, the IP beam size tuning has always been done at very low bunch charge of $N = 1 \times 10^9$ [12].

In the present ATF2 IP tuning, we can minimize the IP beam size of P_{AY}, P_{EY} and P_{32} by using the linear knobs. The examples of the linear knob tuning are shown in Fig.8. We scan each linear knob to find the maximum modulation depth as Eq.(5). The

linear knob tunings are carried out frequently in the ATF2 beam operation, *i.e.)* every time when we change the collision angle of IP-BSM.

We can minimize the beam size component of Y_{22} to Y_{66} by using the 2nd order aberration knobs as well as the linear knobs (see Fig.9). The example of the IP beam size tuning by the 2nd order aberration knobs related to the normal skew sextupole fields Y_{24} and Y_{46} are shown in Fig.9. Y_{24} corrects the IP beam size growth by the geometrical aberration, and Y_{46} corrects the IP beam size growth by the chromaticity. Since the effect of IP beam size growth is small dependence to the modulation depth for IP-BSM 2-8 degree mode (dynamic range of IP-BSM 2-8 degree mode is more than 300nm), we did the 2nd order knob tuning at more than 30 degree mode.
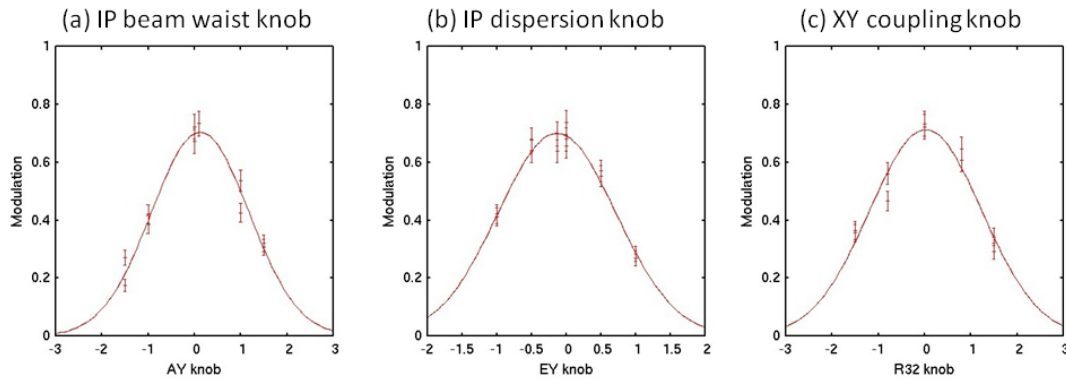
Figure 8: Example of the IP beam size tuning by using linear knobs. We show the results of IP-BSM 2-8degree mode.
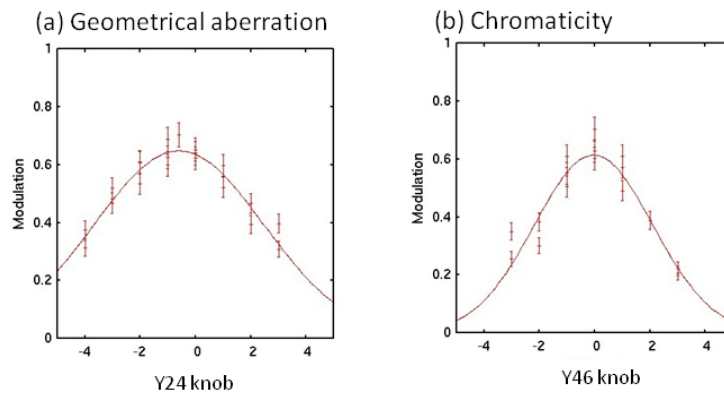
Figure 9: Example of the nolinear knobs by changing the strength of normal sextupole magnets in the final focus beamline. We show the results of IP-BSM 30degree mode.

2.2.4.5.1 First Observation of the Modulation of IP-BSM 174 Degree Mode

We had succeeded to observe the IP-BSM modulation at 174 degree mode at December 2012. Since the IP beam size should be 90nm to observe the IP-BSM modulation at 174 degree mode, this result is one of the largest progress for ATF2 operation. In December 2012, all of the beam time of ATF operation was spent to focus the IP beam size. The trend of the IP-BSM modulation measurement is shown in Fig.10. In the figure, we put the measurement of 3 different laser collision angles of IP-BSM. When the laser collision angle of IP-BSM is changed to larger angle, the laser fringe pitch is changed to be smaller and we can measure the smaller beam size. You can find that we changed the IP-BSM laser collision angle to be larger angle through the IP beam size tuning.

We had the first trial to find the IP-BSM modulation for 174 degree mode at early morning of 12/20. However, we could not find the modulation. Therefore, we optimized the 2nd order aberration knobs related to skew sextupole field errors. The results of the IP beam size optimization with the 2nd order aberration knobs Y_{22}, Y_{26} and Y_{44} are shown in Fig.11. The IP beam size corrections with the 2nd order aberration knobs were done by maximizing the IP-BSM modulation in 30 degree mode. Since the IP beam size contribution of Y_{66} is smaller than others and the dynamic range is small, we always correct the 2nd order aberrations only to Y_{22}, Y_{26} and Y_{44}. After the correction of skew sextupole field errors, we had succeeded to observe almost 22% of the IP-BSM modulation in 174 degree mode. It meant that we could focus the electron beam to less than 73nm.
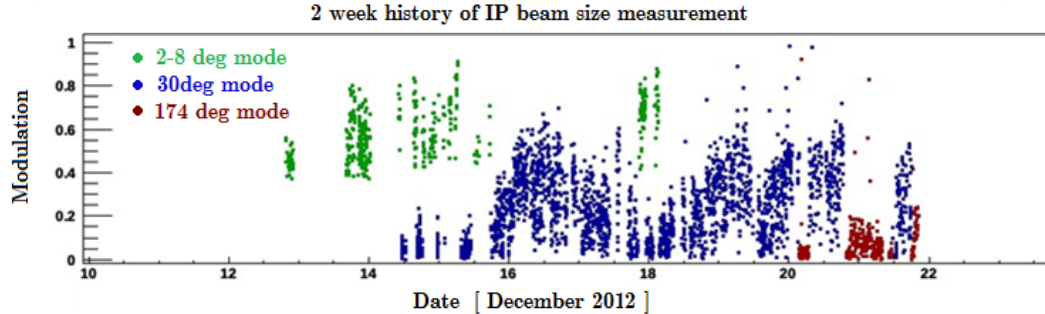
Figure 10: Trend of IP-BSM modulation depth at December 2012 operation. In the figure, we show the measurement with 3 different laser collision angles of IP-BSM. We changed the laser collision angle to larger angle through the IP beam size tuning.
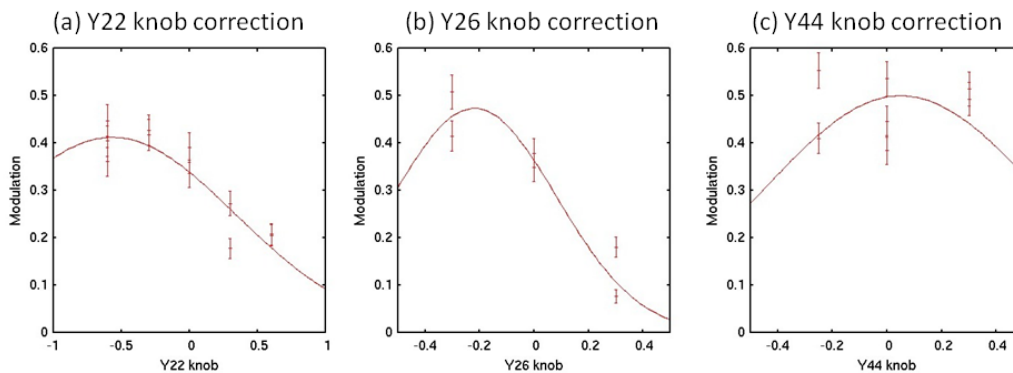
Figure 11: Results of the nolinear knob tunings by changing the strength of skew sextupole magnets in the final focus beamline in 2012 December.

2.2.4.5.2 Present Status of IP Beam Focusing at ATF2 IP

Since the amount of the IP beam size correction by the skew sextupole field errors were also much larger than the expectation from the magnetic measurements at December 2012 operation, we investigated the error source by comparing the skew sextupole field distribution of the correction to the beam tracking simulation with skew sextupole field errors at various beamline locations. The simulation said that one of the candidates for the field error sources is a sextupole magnet. Therefore, we measured the impedances of all coils for the sextupole magnet, and we found the impedance of 1 coil was smaller than others. Since we did not have the spare of sextupole magnet, we swapped the sextupole magnet to the weakest one. After the magnet swapping, the IP beam size was improved to be able to measure the IP-BSM modulation in 174 degree mode without any corrections with skew sextupoles. Fig.12 shows the results of the skew sextupole field correction after the swapping. The optimum settings of the 2nd order aberration knobs Y_{22}, Y_{26} and Y_{44} are set to be almost zero. It means that the skew sextupole field error in the final focus beamline was reduced to be quite small after the magnet swapping.

Furthermore, we applied the optimization of R_{31} knob to correct the beam tilt with respect to the IP-BSM fringe. The result of beam tilt correction with R_{31} knob is shown in Fig. 13. The correction was done with IP-BSM 174 degree mode. We reset the R_{31} knob after we corrected the beam tilt, and we rotated the IP-BSM fringe by changing the laser paths of IP-BSM. The tilt angle evaluated by changing the IP-BSM fringe tilt also is shown in Fig.13. The both tilt angles were almost same to 8-9mrad, and the IP beam size contributions by the fringe tilt were 70-80nm when the tilt angle was not corrected. We realigned the IP-BSM laser paths just after the tilt observation. We had never observed such a large tilt angle after the laser realignment. Therefore, we considered the large tilt angle caused by IP-BSM fringe, not beam. Anyway, we could correct IP-BSM fringe tilt by tilting either the beam with R_{31} knob, or the IP-BSM fringe.

The maximum modulation depth of IP-BSM 174 degree mode was measured just after the tilt angle correction at March 2013. The measured IP-BSM modulations are shown in Fig. 14. The maximum IP-BSM modulations were almost 30% both for the beam tilt correction with R_{31} knob and IP-BSM fringe tilt correction. Since we have not yet evaluate the modulation reduction factor of IP-BSM, we can only say the upper limit of IP beam size from the IP-BSM modulation at present. However, since the 30%

of IP-BSM modulation for 174 degree mode corresponds to 65nm beam size at IP, we did focus the beam to ATF2 IP to less than 65nm. We must evaluate the modulation reduction factor and the contribution of the beam jitter to evaluate the IP beam size not only as the upper limit. The minimum beam size at ATF2 is smaller than FFTB, and we did demonstrate the final focus system based on "*Local Chromaticity Correction Scheme*" at ATF2.
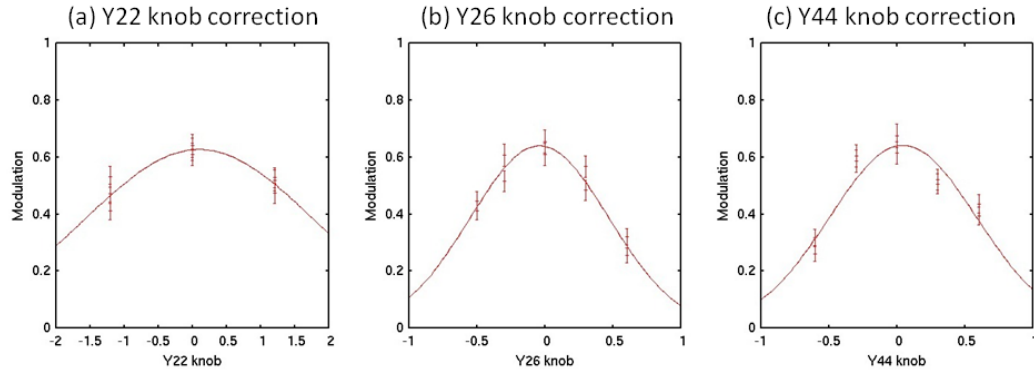
Figure 12: Results of the nolinear knob tunings by changing the strength of skew sextupole magnets in the final focus beamline in 2013 March.

Table 1: Summary table of the ATF2 IP beam size.

Parameters	Design	Achieved
Vertical Emittance	12 pm	
IP beta function	0.1 mm	
IP beam size	37 nm	< 65 nm
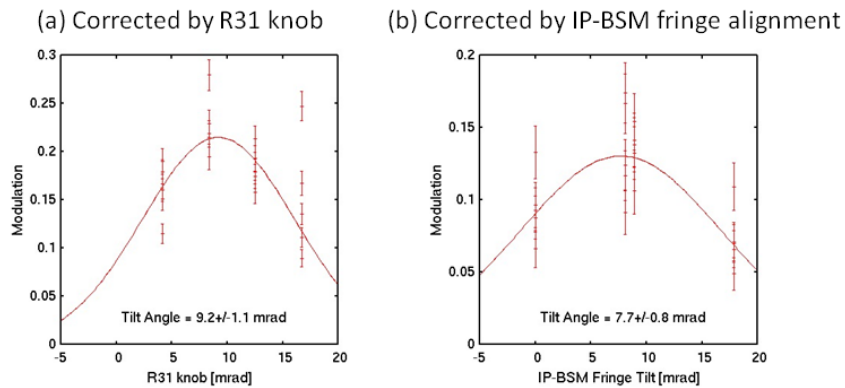
Figure 13: IP-BSM fringe tilt with respect to the beam was corrected (a) by using R_{31} knob, (b) by the IP-BSM fringe tilt angle change.
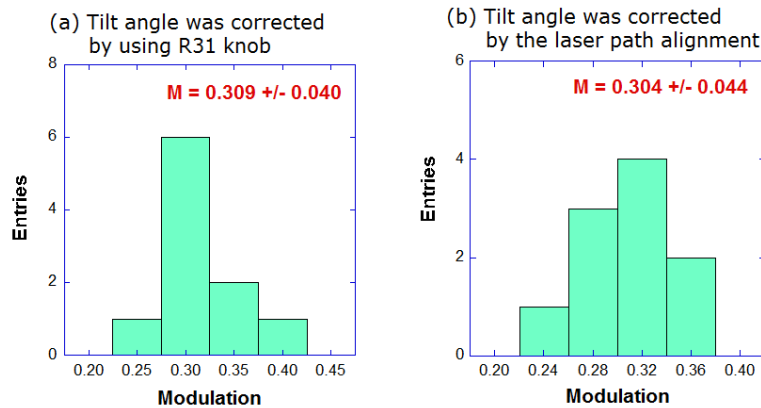
Figure 14: The measured IP-BSM modulation in 174 degree mode. The beam tilt angle corrected (a) by using R_{31} knob, (b) by the IP-BSM fringe tilt angle change. If we assumed that there were no reasons to be reduced the IP-BSM modulation, the 30% of the modulation corresponds to 65nm.

2.2.4.6 *References*

1. ATF2 proposal, KEK-Report 2005- 2 (2005).
2. P. Raimondi and A. Seryi, "Novel Final Focus Design for Future Linear Colliders", Phys. Rev. Lett., **86** 3779 (2001).
3. ILC Global Design Effort, "ILC Technical Design Report", Vol. 1-4, (Volume 3 - Accelerator), 12 June 2013, http://www.linearcollider.org/ILC/Publications /Technical-Design-Report.
4. "CLIC Conceptual Design Report", CERN-2012-007.
5. T. Shintake, "Proposal of a nanometer beam size monitor for e⁺e⁻ linear colliders", Nucl. Instru. Meth., **A311**, 455 (1992).
6. V. Balakin *et al.*," Focusing of Submicron Beams for TeV-Scale e⁺e⁻ Linear Colliders", Phys. Rev. Lett., **74** 2479 (1995).
7. T. Suehara, Doctor Thesis, University of Tokyo (2008).
8. A.Seryi, M.Woodley and P.Raimondi, "A Recipe for Linear Collider Final Focus System Design", SLAC-PUB-9895, Presented at PAC-2003.
9. E. Marin *et al.*, "Status of the ATF2 Lattices", proceedings of 2nd International Particle Accelerator Conference, San Sebastian (2011) TUPC016, CERN-ATS-2011-122.
10. T. Okugi *et al.*, "Linear and 2ⁿᵈ order optics correction of ATF2 final focus beamline", to be submitted to Phys. Rev. ST-AB.
11. KEK SAD homepage, http://acc-physics.kek.jp/SAD/
12. Wakefield, in this newsletter.

2.2.5 **ATF2 Ultra-Low Beta Optics**

Eduardo Marin
SLAC National Accelerator Laboratory, USA
Mail to: emarinla@slac.stanford.edu

2.2.5.1 *Motivation*

The ATF2 nominal lattice is a scaled-down version of the ILC Final Focus System (FFS) [1], which features a value of the horizontal and vertical beta function at the

virtual interaction point (β_x^*, β_y^*) equal to 4 mm and 0.1 mm, respectively. The corresponding beam sizes at this location (σ_x^*, σ_y^*) are 3.2 um and 37 nm[1] respectively, if an error-free lattice is considered in the simulation. The interest of going to ultra-low beta optics lies in the luminosity enhancement due to the smaller beam sizes at the interaction point. However the minimum achievable σ^* defined by the Oide effect, see Ref.[2] is below 37 nm, leaving some room for ultra-low beta configurations.

The ATF2 ultra-low β^* lattice [3] is a proposal for an even more challenging optics with a value of β_y^* a quarter of that of the ATF2 nominal lattice. The expected σ_y^* is equal to 23 nm, assuming an error-free lattice. However when reducing the value of β_y^* the chromaticity (ξ) of the FFS increases inversely proportional to β^*:

$$\xi_{x,y} \approx \frac{L^*}{\beta_{x,y}^*},$$ (1)

if only the Final Double FD is considered in the calculation. L^* is the free distance between the FD and the virtual IP.

Table.1 shows the relevant parameters of the ATF2, CLIC and ILC designs, with special attention to the vertical chromaticity, shown in the last column estimated as Eq.(1).

The goal of the ATF2 ultra-low β^* lattice is to explore the feasibility of a FFS with a higher chromaticity than the ATF2 Nominal lattice, being comparable to that of the CLIC FFS.

Although the Oide limit represents a theoretical limitation, the FFS may be limited by the technological aspects. The ATF2 ultra-low β_y^* lattice is obtained by changing the strength of its magnets, thus we need to make sure that the power supplies that feed the magnets can provide the required magnet currents. Reduced values of β^* imply larger values of $\beta(s)$ throughout the FFS, this become specially important at the high β regions, e.g at the FD.

Table 1: Comparison between relevant parameters of different FF

Project	Beam Energy	$\gamma\varepsilon_y$	σ_y^*	β_y^*	L^*	ξ_y
	[GeV]	[nm]	[nm]	[mm]	[m]	
ATF2 Nominal	1.3	30	37	0.1	1.0	10000
ATF2 Ultra-low β^*	1.3	30	23	0.025	1.0	40000
CLIC L^*=3.5 m	1500	20	1	0.069	3.5	50000
ILC (Low Power)	250	36	3.8	0.2	3.5	17500

The behavior of the $\beta(s)$ along the drift space between the FD and the IP, is described by the known formula:

$$\beta_{x,y}(s) = \beta_{x,y}^* + \frac{(s-s_w)^2}{\beta_{x,y}^*},$$ (2)

where s is the distance along the reference trajectory and s_w refers to the waist location.

Consequently, reducing β^* a factor 4 increases σ at the FD by a factor 2 as:

---

1   A relative energy spread $(\Delta p/p)$ of 0.08% and high order aberrations of the beam are taken into account in the beam size calculation.

$$\sigma_{x,y}(s) \; = \; \sqrt{\epsilon_{x,y}\beta_{x,y}(s)}. \tag{3}$$

It is important that the beam size remains well below the size of the beam pipe, usually a factor 10 smaller is considered as a good practice. In addition, larger beam sizes make the beam more sensitive to magnetic field errors, thus the field quality of the FFS magnets may severely impact the expected IP spot sizes. The tuning of the FFS is the last aspect covered in this study. In Ref.[3] was shown that larger tuning difficulties are expected for lattices with larger chromaticities. In fact the number of required iterations for tuning a lattice (N_{iter}) as a function of the ξ goes as:

$$N_{iter} \; \approx \; \sqrt{\overline{\xi_{x,y}}} \tag{4}$$

In the following, the mentioned aspects are described in detail.

2.2.5.2   *ATF2 Ultra-Low β^* Lattice*

2.2.5.2.1 Design of the ATF2 Ultra-Low β^* Lattice

The values of σ^* presented in Table.1 for the ATF2 and LC projects are evaluated by the MAPCLASS code [4, 5] assuming error-free lattices. The obtained spot size by MAPCLASS refers to the following calculation:

$$\sigma \; = \; \sqrt{\int (u - \bar{u})^2 \; \rho \; dv}, \tag{5}$$

where u stands for x, p_x, y, p_y and ρ is the particle density distribution.

Usually σ^* is larger than the one measured by the Shintake monitor, although rms and Shintake beam sizes coincide when the particle beam distribution can be represented by a Gaussian distribution.

The field quality of the magnets might preclude to reach small beam sizes at the IP, this is of special importance at the FD, where the largest beam sizes throughout the FFS take place. In order to address this issue, the multipole components of the ATF2 FFS magnets have been measured in two different measurement campaigns conducted at IHEP and KEK [6]. Data can be found in Ref.[8]. The multipole component content of the 4Q17 type quadrupole [9], recycled from the PEPII LER accelerator [8], is included in this data. The 4Q17 magnet was installed at ATF2 in November 2012 to replace the focusing quadrupole magnet of the FD (QF1FF) because of its better field quality, see Ref.[10].

The evaluated σ_y^* as a function of the normalized horizontal emittance for the ATF2 ultra-low β^* lattice is shown in Figure 1. σ_y^*=31 nm corresponds to a $\gamma\varepsilon_x$=5 μm. This represents a vertical beam size increase of 35% with respect to the beam size by design, shown in Table 1. In contrast, the impact of the same multipole components is less than 3% for the ATF2 Nominal lattice.
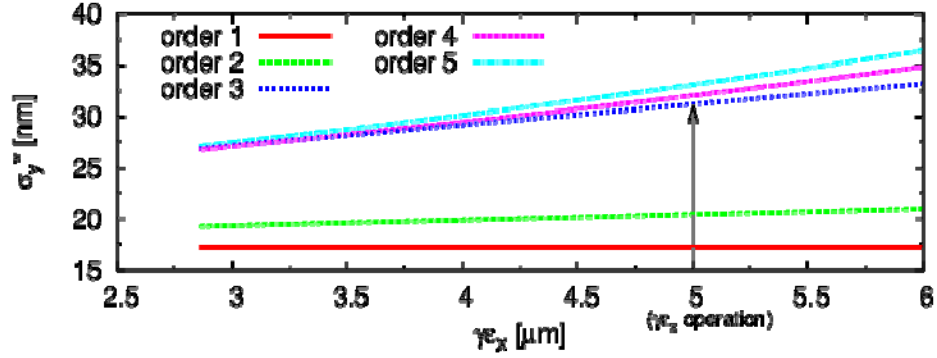
Figure 1: Vertical beam size at the IP as a function of the normalized horizontal emittance for the ATF2 ultra-low β^* lattice when considering all the measured multipole components. Beam size orders 1, 2, 3, 4 and 5 are obtained taking into account up to the quadrupolar, sextupolar, cotupolar, decapolar and dodecapolar components of the ATF2 ultra-low β^* lattice, respectively.

The MAPCLASS code offers convenient tools to understand the observed beam size growth. From the analysis described in Ref.[10], it is inferred that a chromatic octupole component is the main responsible of the evaluated beam size growth, as it is patent in Figure 1, where the 3rd order (blue), that corresponds to an octupole component, increases dramatically with respect to the other orders. Simulations have shown that the inclusion of a pair of octupole lenses would effectively minimize the mentioned aberration, see Ref.[10]. Indeed after optimizing the sextupole magnets and the octupole lenses a σ_y^*=24 nm is achieved for the ATF2 Ultra-low β^* lattice, which represents an impact of the present multipole components smaller than 5%.

A different approach to minimize the detrimental impact of the multipole components consists of modifying the optics by increasing β_x^*. Doing so, the horizontal beta function is lowered along the FFS. Thus, the impact of all the multipole components present in the ATF2 magnets are reduced as well. Although, increasing β_x^* is not the preferred solution, we considered here as an alternative solution to the octupole magnets. The obtained σ_y^* when increasing β_x^* from 4 mm to 4 cm is 23 nm, as described in Ref.[11]. This new lattice design, called ATF2 ultra-low β_y^* can be found in Ref[12].

2.2.5.2.1 Feasibility

In order to determine the feasibility of the new designs we have studied three different aspects; aperture, magnet strength and tuning. In the following these are described in detail.

Figure 2 shows the expected σ_x (solid-green) and σ_y (blue) for the ATF2 ultra-low β^* lattice. The SF1FF, SF5FF and QF9A/BFF magnet apertures are only a factor 7 larger than the expected horizontal spot size. In contrast 10 times σ_x (dashed-green) for the ATF2 ultra-low β_y^* lattice is well below the magnet aperture throughout the FFS.
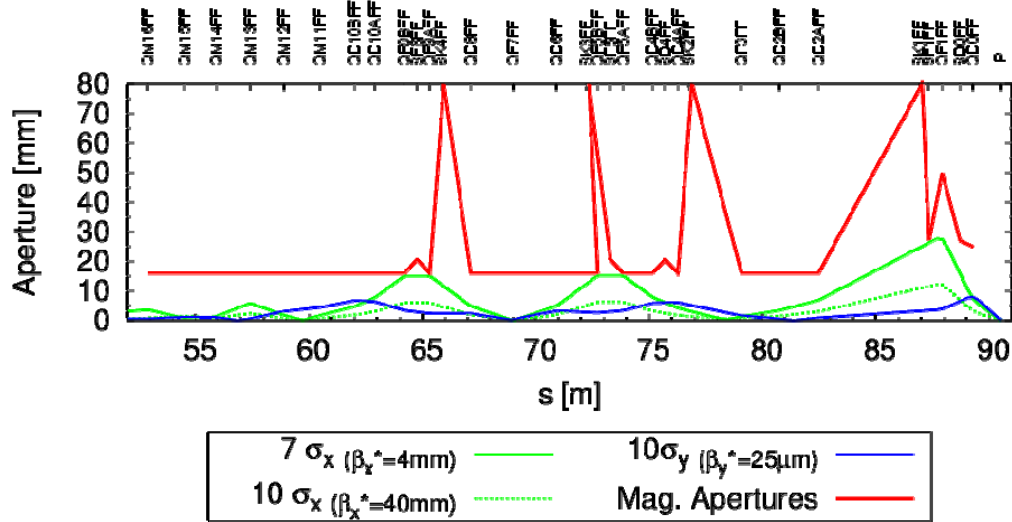
Figure 2: Comparison between beam sizes and the aperture of the magnets (red) along the ATF2 FFS. σ_x (green) is plotted a factor 7 and 10 times larger for the cases when β_x^* is equal to 4 mm (solid line) and 4 cm (dashed line) respectively. σ_y is plotted a factor 10 (blue).

In terms of the magnet strength requirements, the present power supplies of the ATF2 magnets satisfy the required magnet strengths for both new designs, as Figure 3 shows. Except for the FD quadrupoles and sextupoles, practically all the remaining magnets run at a current smaller than half of the maximum current that the power supplies can provide.

We have also studied the tuning performance for the new ATF2 Ultra-low β^* and β_y^* lattices. 100 simulated machines with different initial error configurations are considered to study the tuning feasibility of these lattices.

The measured multipole components and the errors summarized in Table 2. are included in the tuning simulations.

The tuning study is based on pre-computed orthogonal knobs. The response of the most important aberrations of the beam at the virtual IP, namely dispersion (η_x, η_y, η_y'), coupling ($<x,y>$, $<p_x,y>$, $<p_x,p_y>$) and beam waist (α_x, α_y), as a function of the considered knobs is shown in Figure 4. Two additional knobs β_x and β_y, are designed for completeness purposes, however it is not expect a good linear response from them.
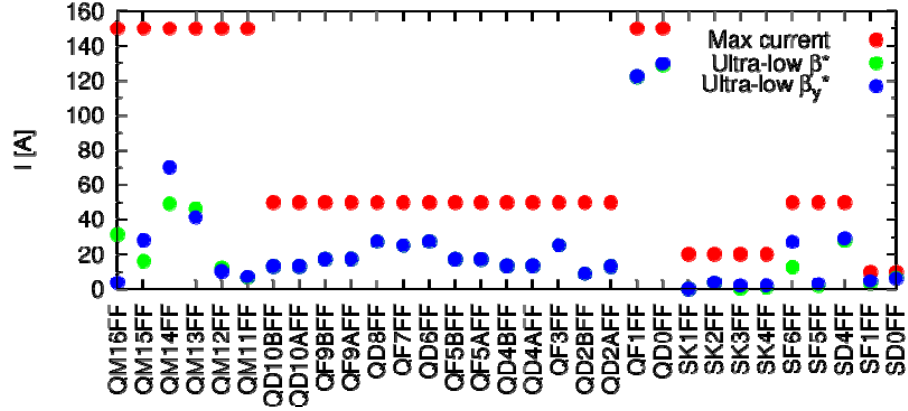
Figure 3: Comparison between the required currents by the ATF2 magnets for the ATF2 ultra-low β^* (green) and ultra-low β_y^* (blue) lattices. The maximum currents that the power supplies can provide are shown in red color.

Table 2: Considered errors in the ATF2 simulation tuning study. σ_{error} refers to the width of the Gaussian distribution which is used to assign the errors for each machine.

Error	σ_{error}
Transverse misalignments	30 μm
Transverse rotations	300 μrad
Relative magnet miss-powering	10^{-4}
Beam size measurement	4%

Almost all the knobs show a good orthogonality except the β_y, $<p_x,p_y>$ and η_y' knobs. A comparable behavior is found for the ATF2 ultra-low β_y^* lattice knobs.

The knobs are scanned iteratively in order to counteract for those ones that are not fully orthogonal. 4 iterations of the η_x, η_y, η_y', $<x,y>$, $<p_x,y>$, $<p_x,p_y>$, α_x, α_y knobs are considered in simulations. The results of the final vertical spot size at the virtual IP are shown in Figure 5.
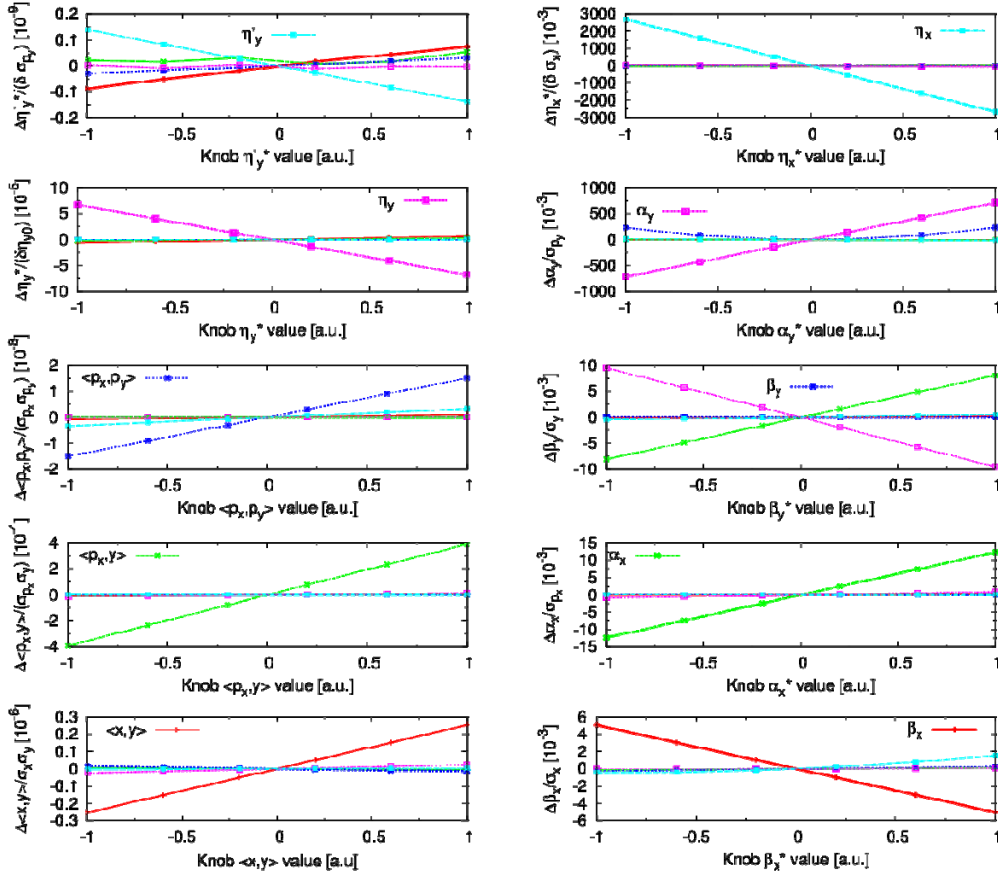
Figure 4: Left plots: Knobs obtained by horizontal sextupole displacements (β_x, β_y, α_x, α_y, η_x) are represented by red, green, blue, magenta and cyan curves respectively. Right plots: Knobs obtained by vertical sextupole displacements ($<p_x,y>$, η_y, η_y, $<p_x,p_y>$, $<x, y>$) are represented by red, green, blue, magenta and cyan curves respectively.
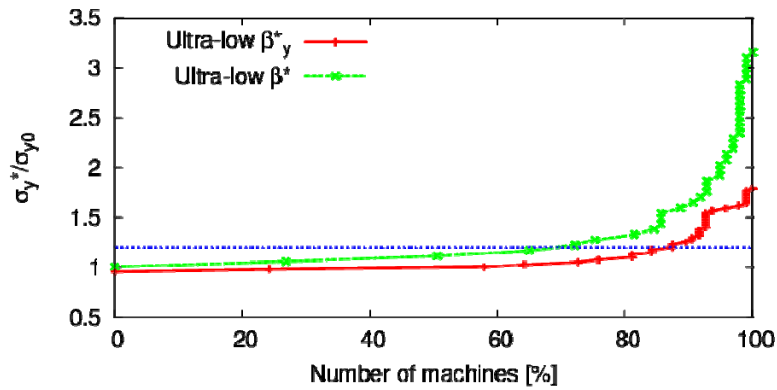
Figure 5: Accumulated histogram of the number of machines that reach a relative σ_y^* a/σ_{y0}^* after scanning the knobs. Blue curve refers to the ATF2 ultra-low β^* and magneta curve refers to the ATF2 ultra-low β_y^* lattice. The grey-dashed horizontal line represents a relative beam size growth of 20% with respect the beam size by design (σ_{y0}^*).

From the results of the simulations for the ATF2 ultra-low β lattice, almost 70% of the machines reach a final spot size <1.2 σ_{y0}^*, being $\sigma_{y0}^* = 24$ nm. In the case of the ATF2 Ultra-low β_y^* lattice, 85% of the machines reach a final spot size <1.2 σ_{y0}^*, being $\sigma_{y0}^* = 23$ nm. Therefore we conclude that tuning based on the knobs presented is capable to recover the design IP vertical beam size under the considered error conditions for both lattices. The different percentage of the number of tunned machines it is due to the different value of β_x^*. Larger tuning difficulties are observed for smaller values of β_x^*, the impact of this parameter on the tuning difficulties needs to be analyzed in further studies.

2.2.5.3 *Conclusions*

By replacing the QF1FF magnet by the 4Q17 magnet, which has a better field quality, the expected beam sizes for the ATF2 ultra-low β^* lattice are noticeable reduced. In order to squeeze the vertical IP beam size beyond 31 nm the insertion of a pair of octupole lenses permits to bring down σ_y^* to 24 nm. Further studies should be conducted to considered a real situation, where a pair of octupoles magnets are inserted in the ATF2 beam line. This studies would permit to fully validate the proposed solution.

Alternatively, the detrimental impact of multipole components is effectively minimized by increasing the value of β_x^* a factor 10. Simulations have shown that this solution fully recovers the σ_y^*, the new design is called ATF2 ultra-low β_y^* lattice. On one hand this is not the desired solution, since this optics do not preserve the transverse beam sizes aspect of the future linear colliders, but on the other hand, this solution eases the operation of ATF2, such as low levels of backgrounds and reduction of tuning difficulties.

Regarding the feasibility of these new lattices, none of them present any limitation in terms of power supply requirements. In terms of apertures, it is worth noticing that the beam size is only a factor 7 smaller than the actual magnet aperture for the ATF2 ultra-low β^* lattice, which may induce higher levels of backgrounds. In terms of tuning, the orthogonal knobs used for tuning both lattices are capable to recover the σ_y^*/σ_{y0}^*<1.2 for 70% and 85% of the number of simulated machines for the ATF2 ultra-low β^* and β_y^* lattices, respectively.

In conclusion, the new ATF2 ultra-low β^* designs minimizes the detrimental impact of the multipole components of the ATF2 magnets. Regarding its feasibility, simulations do not show unbridgeable limitations. The valuable experience acquired by practising with low β^* optics would help to improve the design of the future linear colliders.

2.2.5.4 *References*

1. N. Phinney, N. Toge, and N. Walker. "ILC Reference Design Report Volume 3 Accelerator", arXiv:**0712.2361**, (2007).
2. K. Oide, "Synchrotron-Radiation Limit on the Focusing of Electron Beams", Phys. Rev. Lett., **61** 1713 (1988).
3. P. Bambade *et al*, "ATF2 Ultra-Low IP Betas Proposal", CERN-ATS-2009-092, CLIC-Note-792, (2009).
4. R. Tomás, R, "MAPCLASS: a code to optimize high order aberrations", Note: CERN-AB, AB-Note-2006-017, (2006)".

5. R. Tomás, "Nonlinear optimization of beam lines", Phys. Rev. ST Accel. Beams, **9** 081001 (2006).
6. M. Masuzawa, "QEA Magnet Measurements at KEK and Comparison with IHEP Results",in 11th ATF2 Project meeting (2011). http://ilcagenda.linearcollider.org/conferenceDisplay.py?confId=4904.
7. M. Woodley, "Repository of the multipole component measurements of the ATF2". http://www.slac.stanford.edu/mdw/ATF2/v4.5/.
8. T. Henderson, *et al,* "Design of the PEP-II low-energy ring arc magnets", in Conf.Proc vol. C950501, pg 1322-1324, SLAC-PEP-II-ME-NOTE-95-08, LBL-36473, (1995).
9. M.S. Zisman, *et al*, "Design of the PEP-II Low-Energy Ring", in Proceedings of the Particle Accelerator Conference, 10.1109/PAC.1995.504710, (1995).
10. E. Marin, *et al*, "Design and higer order aberrations of the ATF2 lattices", submitted to Phys. Rev. ST-AB.
11. E. Marin, *et al*, "Status of ATF2 lattices: From Nominal to Ultra-low beta*", in the* European Linear Collider Workshop ECFA LC2013, Desy (Germany), (2003).
12. E Marin, "ATF2 Ultra low betay lattice repository", webpage: http://clicr.web.cern.ch/CLICr/ATF2/New_Multipoles2/ATF2_Ultra_low_beta

2.3   Wakefield Issues for the Linear Colliders

Kiyoshi Kubo[1], Alexey Lyapin[2], Jochem Snuverink[2],
[1]High Energy Accelerator Research Organization (KEK), Japan
[2]John Adams Institute, Royal Holloway University of London, UK
Mail to: kiyoshi.kubo@kek.jp,
Alexey.Lyapin@rhul.ac.uk, Jochem.Snuverink@rhul.ac.uk

The ATF2 [2] is a scaled demonstrator for Raimondi-Seryi final focus systems [3], which are planned for future linear colliders. The aim of the ATF2 is two fold: firstly, to obtain and verify a vertical focus size of 37 nm; secondly, to hold the focus stable to within a few nanometres. The ATF2 collaboration has recently achieved its intermediate goal of a sub-100 nm vertical beam size, measured using an interference pattern Compton scattering beam size diagnostic (Shintake monitor) although only at relatively modest bunch charges of 0.1×10^{10} electrons per bunch [4].

Figure 1: Layout of the ATF2, with the quadrupoles containing cavity BPMs indicated, taken from [1].

2.3.1 **Wakefield Calculations**

Achieving sub-100 nm vertical beam size required lowering the bunch charge from the nominal 1×10^{10} electrons by a factor of 10. Although this had a positive side effect of reducing the Compton signal background of several beam diagnostics, small beam sizes need to be demonstrated at the nominal bunch charge, close to the values required for future linear colliders to achieve their design luminosity. One of the main contributors to the beam size growth is thought to be the effect of wakefields. The extracted bunch length at ATF is relatively large: 7-9 mm, resulting in a wakefield kick of the particles in a bunch by the fields it produces. This has two consequences: the orbit of the bunch as a whole (i.e. centre of mass) alters according to its total charge and position with respect to the wakefield generating elements; and the particles along the length of the bunch arrive at the interaction point (IP), where the beam size is measured, with slightly different offsets, perceived as a beam size increase.

The initial design of the ATF2 beamline did not include a thorough study of the wakefield effects of all the elements. This is normally justified for a single-pass beamline such as ATF2, where collective beam effects do not accumulate. The ATF2 beamline included a number of high impedance elements, such as cavity beam position monitors (CBPMs), unshielded bellows, vacuum ports, step transitions, etc. A study began to identify the major wake kick contributors, understand the wakefield effect on the beam size, and measure the produced kicks.

A number of ATF2 beamline elements have been investigated. The wake potential produced by various geometries was simulated using electromagnetic (EM) simulator GdfidL [5]. GdfidL runs a finite difference loop to numerically propagate the EM fields on a cubic mesh, while the beam is represented by a linear charge with a Gaussian distribution along the *z*-axis, and offsets from the beam axis can be specified in both *x* and *y*.
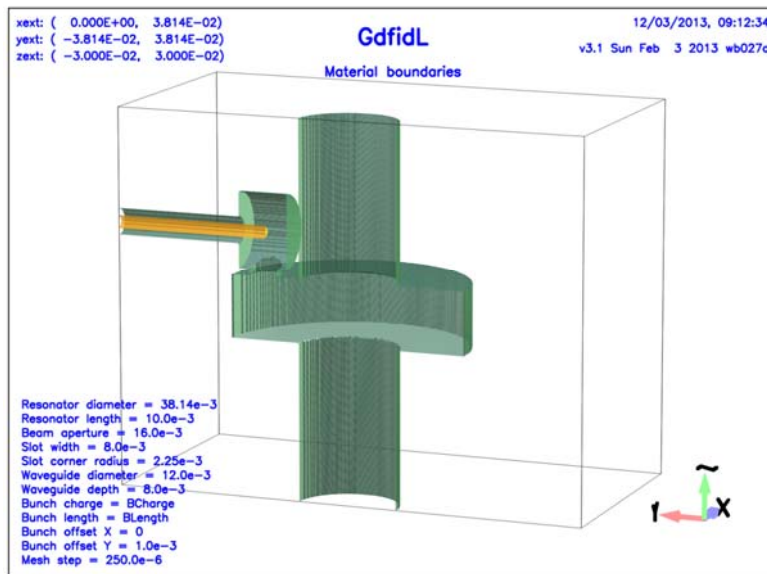
Figure 2: C-band reference cavity model (sliced at the symmetry plane).

Wakefield kick measurements and compensation described in the next sections started with C-band reference cavities, so we consider them here in some detail. The geometry, as meshed by GdfidL, is shown in Fig. 2. It features a cylindrical cavity connected to a cylindrical beam pipe. Although the reference cavity has an asymmetric arrangement for coupling the signals out, the difference of *x* and *y* wakes for the first few oscillations is small (in the order of a few %).

As a computational cross-check, we also calculated the wake potentials for this geometry using a second code, T3P (from ACE3P suite of codes [6]), which uses curved tetrahedral mesh. The transverse wake potential for various beam offsets is shown in Fig. 3, where GdfidL results are plotted in solid and T3P in dashed lines. A very good agreement between the results produced by the two codes has been noted. It is also interesting that the wake potential has a pronounced non-linear behaviour with respect to the beam offset in the first oscillation, during which the excitation still occurs. A third order polynomial has been fitted to the peak values of the wake potential at different offsets (Fig. 4), resulting in $W_{peak}(x) = -0.004 \cdot x^3 - 0.106 \cdot x$.

Fig. 3 also shows the distribution used for the excitation. One can see that the wake potential peaks while the bunch still passes the cavity, meaning an overall kick; and that the wake potential changes substantially on the time scale of the bunch passage meaning a bunch tilt and, as a consequence, a larger perceived transverse bunch size. Both effects are considered in the following sections.
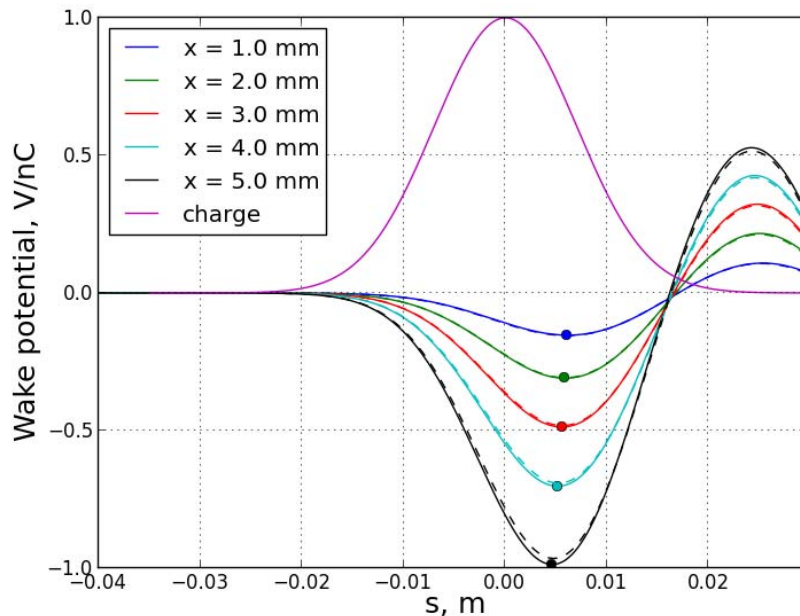
Figure 3: Wakepotential produced by a 1 pC, 7 mm long bunch traveling with different offsets in the C-band reference cavity. The centred Gaussian shape shows the charge distribution.
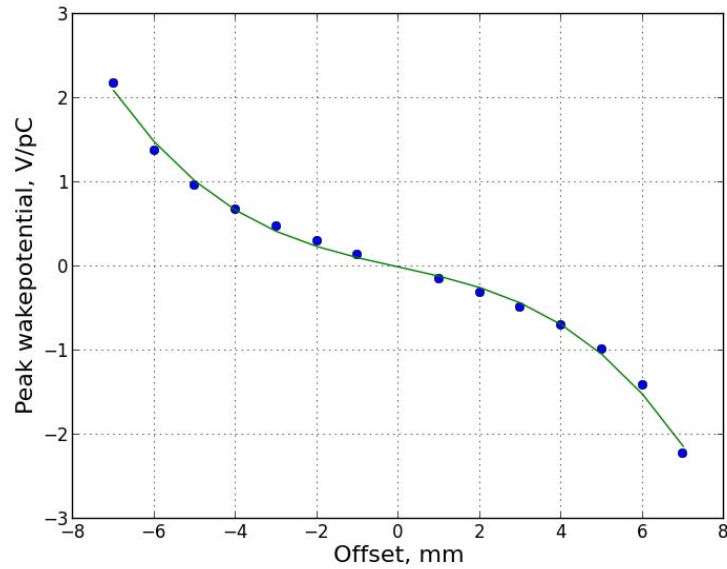
Figure 4: Peak wakepotential of the reference cavity vs. beam offset fitted to a third order polynomial

Table 1 summarizes the peak wake potential $\mathbf{W_{max}}$ for the beamline components that have been studied so far in the order they are most likely to affect the beam, taking into account their quantities (although, strictly speaking, their beamline locations and average misalignment need to be considered). The simulations indicate that shields must be used for the vacuum bellows as their wakefields may reach the level of wakes produced in CBPMs at the same offset, but the alignment is typically much poorer for them. Lower wakes can also be achieved by better alignment of CBPMs to their respective quadrupole magnets. However, the assemblies are not easily accessible as they are already installed in the beamline. Other possible relatively low cost improvements include the removal of unnecessary beampipe aperture transitions and tapering to avoid sudden aperture steps.

Table 1: Summary of the peak wakepotential calculations.

Component	Wmax, V/pC/mm	Quantity
Bellows	0.1	100
C-band position	0.11	40
24-20 mm transitions	0.008	100
C-band reference	0.15	4
Vacuum port (X)	0.07	6

2.3.2 Basics of the Transverse Wakefield Effects

Two important effects of the transverse wakefields on a bunch are changes of the centre of mass orbit and longitudinal position correlated beam distortion. The kick angle of the bunch centre of mass can be expressed as

$$a_\theta = \frac{e\bar{y}q}{E} a_W \tag{1}$$

and

$$a_{\theta^2} = \left(\frac{e\bar{y}q}{E}\right)^2 a_{W^2}, \tag{2}$$

where $\bar{y}$ is the relative transverse offset between the bunch centre of mass and the centre of the wakefield source, q the total bunch charge, and E the beam energy. Here we define the mean wake

$$a_W \equiv \int_{-\infty}^{\infty} W_p(z)\rho(z)dz / q , \tag{3}$$

and the mean square wake

$$a_{W^2} \equiv \int_{-\infty}^{\infty} W_p^2(z)\rho(z)dz / q , \tag{4}$$

where $W_p(z)$ is the wake potential, $\rho(z)$ the charge distribution along the bunch. The spread of the wake potential, σ_W, can be defined as

$$\sigma_W^2 \equiv a_{W^2} - a_W^2 . \tag{5}$$

For the expressions eq. (3) and (4), only dipole wakefields were considered. This assumption is valid while $\bar{y}$ is small compared to the transverse size of the wakefield source. Also, we ignore any differences of transverse position along the bunch, which is a valid approximation in the case of ATF2 beam since the transverse distortion of the bunch is small compared to the considered level of $\bar{y}$.

At a certain location downstream of the wakefield source, position change and beam size increase due to this wakefield:

$$\Delta y = R_{34} a_\theta = \frac{eq\bar{y}}{E} a_W , \tag{6}$$

and

$$\Delta \sigma_y^2 = R_{34}^2 \sigma_\theta^2 = R_{34}^2 \left(\frac{eq\bar{y}}{E}\right)^2 \sigma_W^2 . \tag{7}$$

Note that the beam size squared is expressed as a sum of the beam size squared without the effect of the wakefield and the effect of wakefield,

$$\sigma_y^2 = \sigma_{y,0}^2 + \Delta \sigma_y^2 . \tag{8}$$

Here R_{34} denotes the 3-4 component of the transfer matrix from the wakefield source (a) to the location downstream (b),

$$R_{34} = \sqrt{\beta_a \beta_b} \sin(\varphi_b - \varphi_a) \tag{9}$$

where, $\beta_{a,b}$ are the betafunctions and $\varphi_{a,b}$ betatron phases at locations a and b.

It is obvious that the effects of the wakefield sources in large betafunction regions are significant.

2.3.3 **Wakefield Experiment Setup**

To study the beam distortion and orbit change induced by the wakefields and also to investigate the possibility of compensation of the wakefields generated by other sources (proved to be crucial in achieving sub-100 nm beam size), a wakefield test setup including a two axis mover system with a range of ± 4.5 mm in both the vertical and horizontal directions has been installed in the ATF2 beamline. This system is located in a high betatron location between the quadrupoles QD10BFF and QD10AFF. Various devices in various configurations have been tested with this system. Initially, one C-band reference cavity was installed, and followed by a second cavity of the same type to double the effect. This configuration is shown in Fig. 5. Note that translating the setup also moves the bellows connecting the cavities with the rest of the beamline.
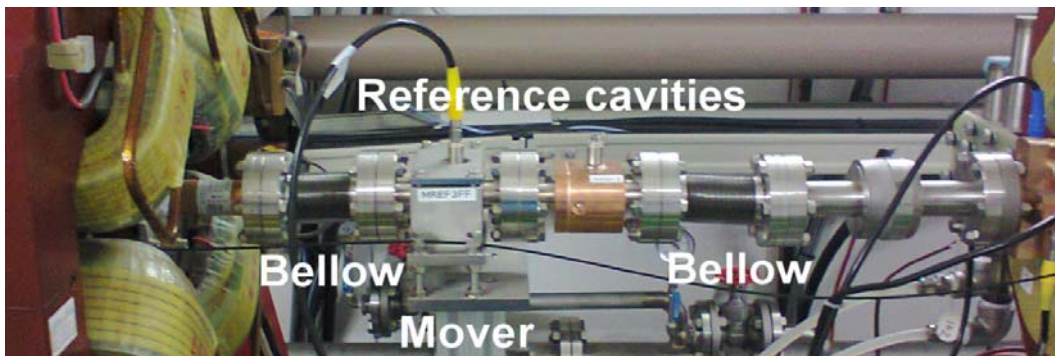
Figure 5: Wakefield experiment installation with two C-band reference cavities and two unmasked bellows.

A total of four different setups will be analysed in this paper, see Fig. 6: (1) one C-band reference cavity with two unmasked bellows at both sides, (2) two C-band reference cavities with two unmasked bellows at both sides, (3) one unmasked bellows with two masked bellows at both sides and (4) one masked bellows with two masked bellows at both sides. The two bellows at both sides are deformed as the mover position changes in all setups, contributing a systematic error in the measurement. It has been assumed that this effect can be approximated by the bellows on the both sides moving by half of the translation of the setup.
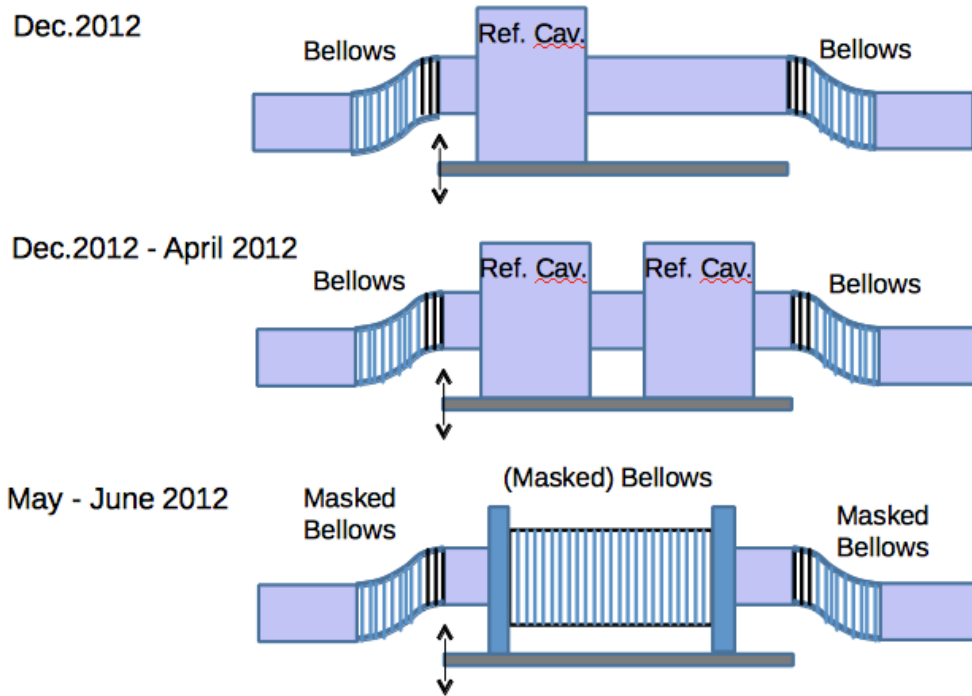
Figure 6: Different setups of the wakefield experiment installation.

Table 2 shows the transverse wakefield potentials calculated for each setup by adding up the results of the numerical simulations.

Table 2: Calculated transverse wake potentials for each setup.

Setup	Wake potential (V/pC/mm)
1 reference cavity + 2 deformed non-masked bellows	0.27
2 reference cavities + 2 deformed non-masked bellows	0.42
1 non-masked bellows + 2 deformed masked bellows	0.12
1 masked bellows + 2 deformed masked bellows	0.02

2.3.4 Orbit Measurement

With several high resolution CBPMs both upstream and downstream of the wakefield experiment, it is ideally placed for studying the orbit change due to the wakefields with a high precision. Since the betatron function is higher in the vertical direction in the downstream beamline, typically a vertical position scan was performed recording about 100-200 pulses for several mover positions.

To analyse the orbit change due to the translation of the wakefield setup, the pulse to pulse orbit jitter, which is up to tens of μm vertically, depending on the beamline location, needs to be subtracted. This is done as follows. The correlation matrix $\mathbf{X}$ of the n_1 upstream BPMs with the n_2 downstream BPMs is defined as:

$$\mathbf{A\,X} = \mathbf{B} \tag{10}$$

with matrix $\mathbf{A}$ ($\mathbf{B}$) the upstream (downstream) containing average subtracted BPM readings for all m pulses recorded at the nominal mover position. The matrix $\mathbf{X}$ is then

determined in a least-square sense by inverting matrix **A**. The remaining residuals **R** (n_2 x m)

$$R = AX - B \tag{11}$$

Indicate the precision of the orbit reconstruction for each of the downstream CBPMs. The jitter subtraction is then applied to the data at different mover positions, and the residuals **R** are averaged for each mover position to extract the systematic offsets.

In Fig. 7 the residuals are plotted with respect to the mover position for a test system of two reference cavities at a downstream location where the orbit response is one of the strongest (QD2BFF). The dependence is very clear and the third order effect as predicted by the numerical calculations can be observed. The statistical error on each point is about 200 nm. A third order fit is performed which describes the data well with about 3.2 μm orbit change per mm reference setup move in the linear regime of up to 2.0 mm.
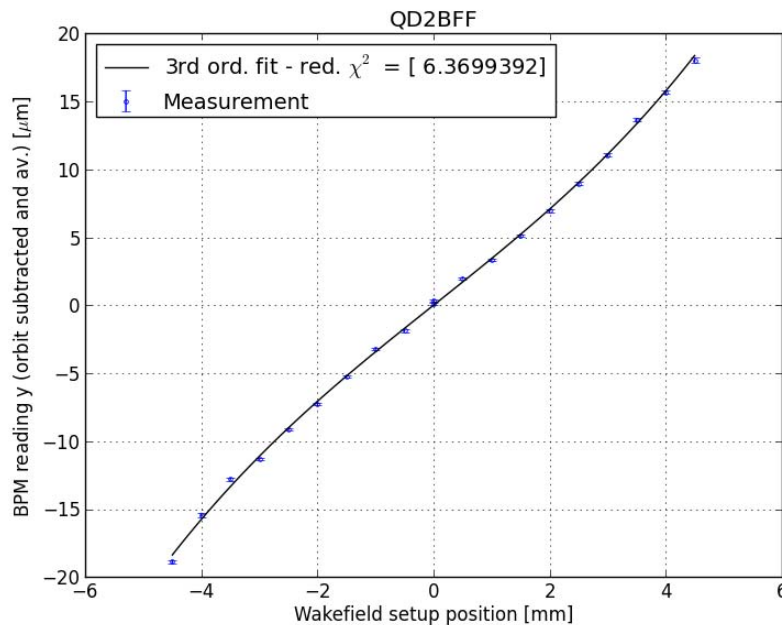
Figure 7: The orbit change with respect to the wakefield setup position for two reference cavities after pulse averaging and jitter subtraction of the CBPM readings in the vertical direction near quadrupole QD2BFF.

The bunch length for these data was monitored with a streak camera located in the ATF damping ring [7]. The bunch length in the turn before extraction was determined to be about 9 mm while the average bunch charge was about 0.75×10^{10} particles.

In order to support the measurement and determine the wakefield potential of the setup from the measurement of the beam displacement, a tracking simulation has been performed with the tracking code PLACET [8]. Especially for this study, realistic geometric wakefield descriptions have been added to the code. For each of the downstream BPMs the linear response with respect to the mover position is determined, which is shown in Fig. 8.
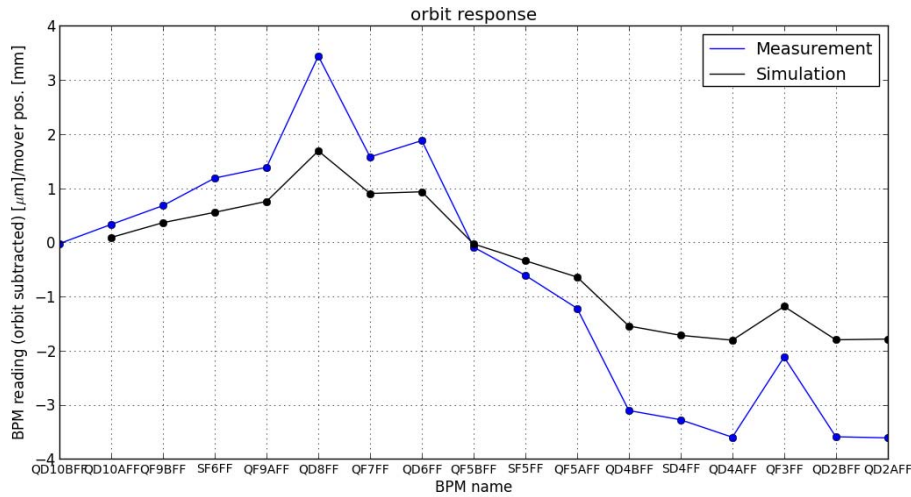
Figure 8: The vertical orbit response for each CBPM with respect to the wakefield setup position for the two reference cavity setup. The measurement and simulation are compared after the pulse averaging and jitter subtraction.

The simulation shows a good agreement with the observed orbit change. However, the measured response appears to be a factor 1.8 higher than the prediction and the measurement for the setup of two reference cavities shows a wakefield potential of about 0.7 V/pC/mm. Further work is underway to understand the difference compared to the estimate of 0.4 V/pC/mm based on numerical calculations.

2.3.4.1.1 Bunch Intensity Dependence

Similar measurements were taken with different bunch intensities. One of the intensity scans for the two reference cavities is shown in Fig. 9. The intensity should be regarded as indicative for the moment. A clear intensity dependence can be seen that is roughly linear as expected. Note that the CBPM resolution and hence the precision of the orbit response measurement, are degraded at lower bunch charges.

Measurements have also been performed at different bunch length settings and different setups. The data is currently being analyzed and a further journal publication is anticipated.

78

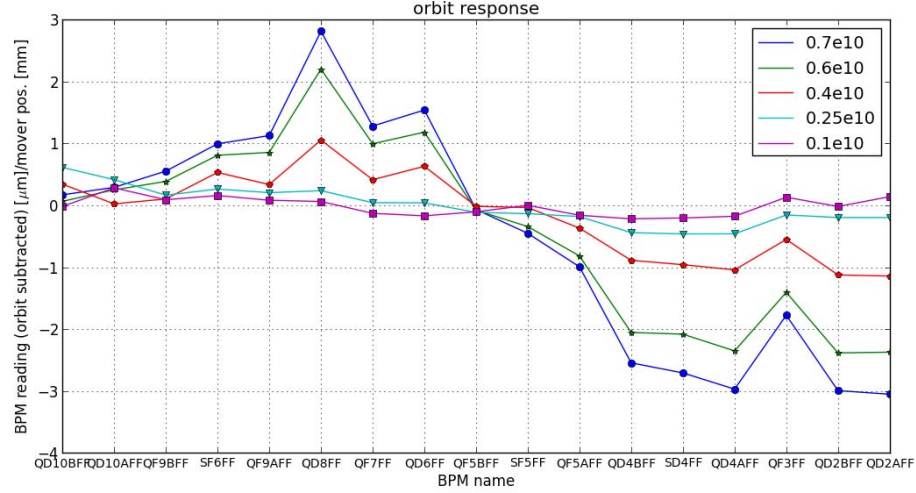**Figure 9:** The vertical orbit response for each BPM with respect to the wakefield setup position with two reference cavities for different bunch intensities after pulse averaging and jitter subtraction.

2.3.5 Beam Size Study Using On-Mover Wakefield Source

As presented in section 2.3.3, four different setups have been investigated: (1) one C-band reference cavity with two non-masked bellows at both sides, (2) two reference cavities with two non-masked bellows at both sides, (3) one non-masked bellows with two masked bellows at both sides and (4) one masked bellows with two masked bellows at both sides. Two bellows at both sides in each setup are deformed as the mover position changed.

We measured the vertical beam size at the IP while changing the vertical position of the on-mover wakefield sources, and also varying the bunch charge in various combinations.

Since the beam size increase produced by a single wakefield source can be expressed as eq. (7), we fitted the data from the measurement with a fixed bunch charge to

$$\sigma_{y,m}^2 = A^2 + B^2(q)(y - y_0)^2,$$
(12)

where y is the mover position. A, B and y_0 are the free parameters in the fitting.

Fig. 10 shows examples of measured modulation of IPBSM with a 30 degree crossing angle as a function of the vertical position of the mover. The curves are the results of fits to a function

$$M(y) = M_0 \exp\left(-2B^2 k_y^2 (y - y_0)^2\right),$$
(13)

with free parameters M_0 and B, where M_0 is the modulation corresponding to the minimum beam size, or the modulation at $y = y_0$.
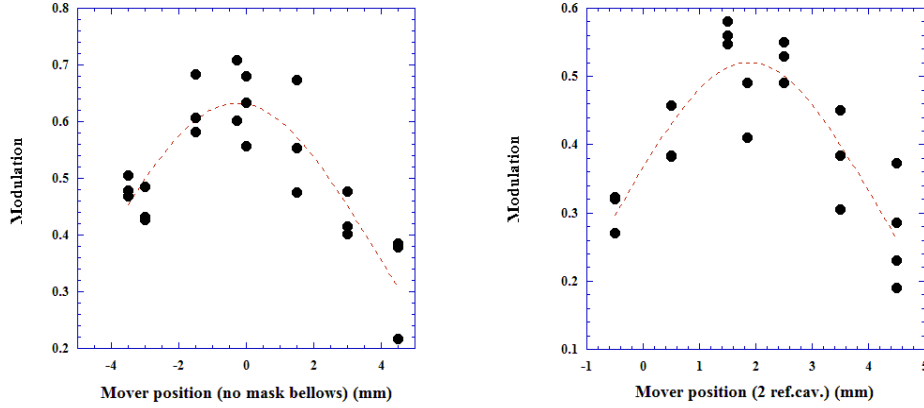
Figure 10: Examples of the beam size measurement vs. vertical position of the mover with wakefield sources. Left: two reference cavity setup, N=5E9, Right: one unmasked bellows setup, N=4E9.

Using the results of these fits for various bunch charge settings, another fit was performed to

$$B(q) = Cq$$.

(14)

A and C respectively correspond to

$$A = \sigma_{y,0}$$,

(15)

$$C = R_{34} \frac{e}{E} \sigma_W$$.

(16)

Using eq. (15), the known R_{34} and beam energy, σ_W was evaluated as in Table 3 from experimental data for 4 cases. Note that the measurement errors have not yet been estimated.

The evaluated σ_W in each case is simply a sum of the σ_W of all moved components. Therefore σ_W of the reference cavity is estimated from the first two data sets as

$$\sigma_W(\text{ref.cav.}) = 0.258 - 0.168 = 0.090 \text{ V/pC/mm}$$

(17)

Assuming the wakefield of one deformed bellows is equivalent to half the wake of fully translated bellows, σ_W of the unmasked bellows can be estimated as

$$\sigma_W(\text{bellows}) = 0.168 \times 2 - 0.258 = 0.078 \text{ V/pC/mm}$$

(18)

Similarly, from the last data set, σ_W of the bellows with the mask is

$$\sigma_W(\text{masked - bellows}) = 0.024/3 = 0.008 \text{ V/pC/mm}$$

(19)

σ_W of the unmasked bellows can also be estimated from the last 2 data sets:

$$\sigma_W(\text{bellows}) = 0.094 - 0.024 \times (2/3) = 0.078 \text{ V/pC/mm}$$

(20)

which is precisely the same result as in eq. (18).

These evaluations from the measured data are compared with calculations for each structure in Table 4. There is a discrepancy of a factor of 1.7 for the reference cavity and a factor of 2.1 for the unmasked bellows. We are planning to continue this work in order to understand the discrepancies, in particular, errors of the beam size measurement need some further analysis. The factor 1.7 obtained for the reference cavity is, however, in a very good agreement a similar factor obtained from the kick measurements in 1.1.5. At the same time, the accuracy of the wakefield calculation for the bellows may not be satisfactory, since it is impossible to provide accurate geometrical input for that structure using manufacturing drawings due to its flexibility. Also, the above assumption on the value of the peak wakefield made for the deformed bellows is not convincing, and eventually the deformation may change non-linearly with the mover position. Also there might be other significant wakefield sources, such as small gaps between flanges connecting the components.

Table 3: Measured σ_W (V/pC/mm) of wakefield sources on mover.

Set up	σ_W
1 reference cavity + 2 deformed non-masked bellows	0.168
2 reference cavities + 2 deformed non-masked bellows	0.258
1 non-masked bellows + 2 deformed masked bellows	0.094
1 masked bellows + 2 deformed masked bellows	0.024

Table 4: Calculated σ_W (V/pC/mm) of 2 components.

Component	Measured σ_W	Calculated σ_W
reference cavity	0.090	0.053
non-masked bellows	0.078	0.037
masked bellows	0.008	-

2.3.6 Beam Size Dependence on Intensity

2.3.6.1 *Measurement*

We observed a strong intensity dependence of the IP beam size, which seems to be attributed to the wakefields. Experimental data to investigate the intensity dependence have been taken in various conditions. Two examples are shown in Fig. 11. They show modulations observed with the IPBSM at the 30 degree crossing angle as function of bunch population. The data in the left figure was taken on April 26, and in the right figure on May 21. The lines are the results of fitting assuming the increase of beam size squared is proportional to the square of the bunch charge.

$$\sigma_y^2(N) = \sigma_y^2(0) + w^2 q^2 \tag{21}$$

Fitted w from the data is 100 nm/nC and 140 nm/nC, respectively.
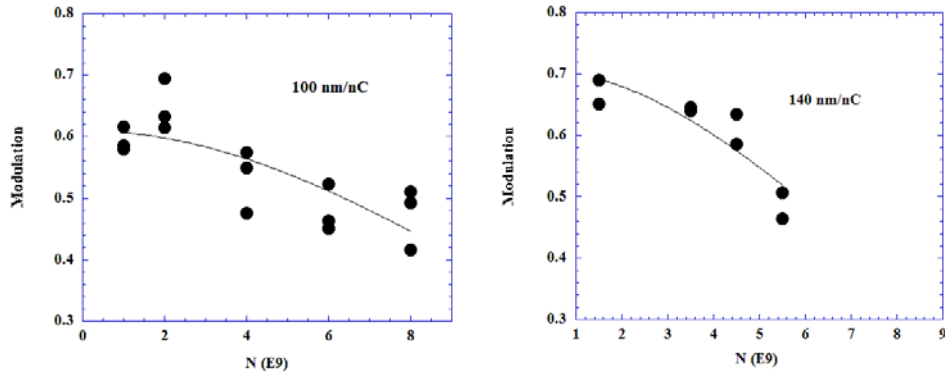
Figure 11: Modulations of IPBSM with 30 degree crossing angle as function of bunch population. Left: taken on April 26; Right: May 21.

We took similar data in various conditions and at different times of the day. The fit parameter w from was typically about 100 nm/nC but experienced wide variations. The reliability of the experimental data is still under investigation.

2.3.6.2 *Effect of Misalignment*

The total effect of many wakefield sources onto the beam size is the sum of the effects produced by each source, as expressed by eq. (7).

We calculated the factor w in eq. (21) assuming there is a wakefield source equivalent to one CBPM plus two bellows at every quadrupole magnet and each source is randomly misaligned according to the normal distribution with an rms of 1 mm. Fig. 12 shows the distribution of simulated w for 400 random seeds.
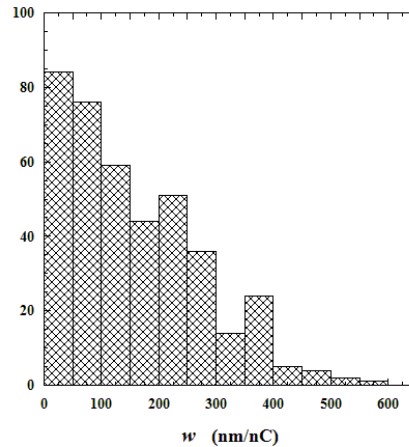
Figure 12: Distribution of calculated parameters w for a random misalignment of CBPMs with 2 bellows at each quadrupole magnet of 1 mm rms.

Most of the seeds gave larger w than typical value of experiments, 100 nm/nC. However, it should be considered that experimental data were taken with optimized position of the on-mover wakefield source system. In the final focus beam line, betatron phase advance from all components at high betafunction locations to IP are almost $(n+1/2)\pi$. In other words, all possibly significant wakefield sources are at the same or

the opposite betatron phase. Therefore if the shape of the wake potential of the misaligned components is similar to the wake potential of the position-adjusted structure, they can be almost cancelled. Fig. 13 shows the results of tracking simulations of the mover scan. Here we set a random misalignment of each wakefield source (CBPM and two bellows) at every quadrupole magnet with an rms of 1 mm, a bunch charge of 1 nC, and scan the vertical mover position. Modulation of the IPBSM signal with a 30 degree crossing angle was simulated for (left figure) 2 reference cavities, and (right figure) 1 bellows on. The peak modulation of each scan corresponds to $w = 19$ nm/nC and $w = 34$ nm/nC respectively. These good compensations are expected from the similarities of the wake potential shapes of the C-band cavity BPM, the C-band reference cavity and the bellows shown in section 2.3.5.

Taking into account the known wakefield sources (CBPMs and bellows) can be well compensated for, it is not probable that their random misalignments are the main source of the experimentally estimated intensity dependence factor $w \sim 100$ nm/nC.
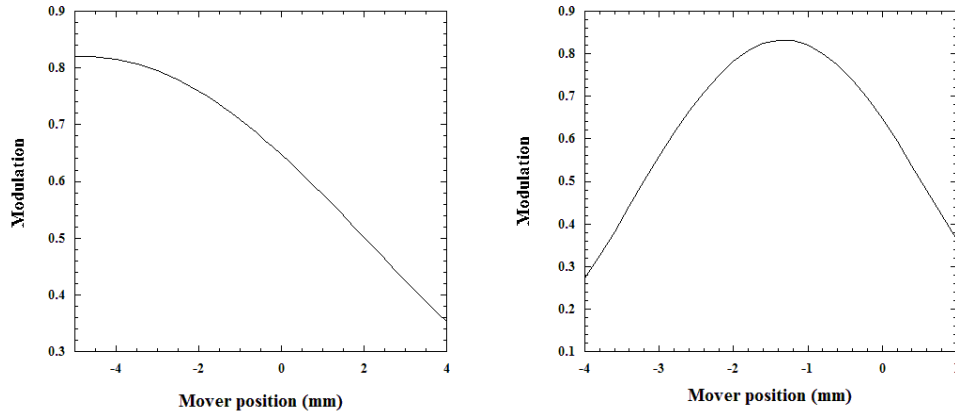
Figure 13: Simulation of the wakefield compensation, IPBSM modulation vs mover position. CBPM + 2 bellows at every quadrupole magnet are randomly misaligned with an rms of 1 mm. (left) 2 reference cavities (right) 1 bellows.

2.3.6.3   *Effect of the Orbit Distortion*

Although the effect of the wakefields produced by sources with static misalignments can be almost fully compensated for, time varying wakefield kicks induced beam orbit distortion cannot be compensated.

The orbit distortion can be divided into two orthogonal phases: "position at the IP" and "angle at the IP" phases. As mentioned before, the betatron phase advance from high betafunction locations to the IP is almost $(n+1/2)\pi$ (where n is integer), which means the "position at the IP" phase orbit has a very small offset at all significant wakefield sources. Therefore, only the "angle at the IP" phase orbit can produce large beam excursions in the high betafunction region and induce significant wakefields.

Fig. 14 shows the "angle at the IP" phase orbit with 1-sigma amplitude along the ATF2 beam line. The maximum vertical position is about 0.3 mm. Fig. 15 shows the calculated factor w, beam size increase due to wakefield defined by eq. (21), as a function of the amplitude of the "angle at the IP" orbit distortion.
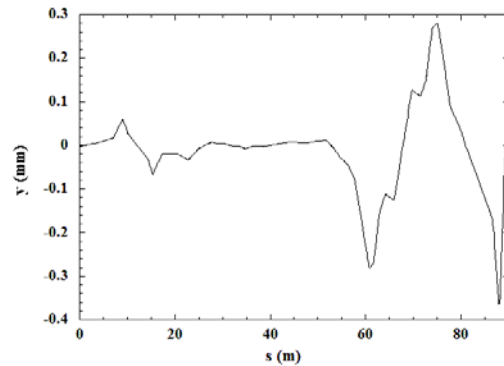
Figure 14: 1-sigma "angle at IP" phase orbit along the ATF2 beam line.
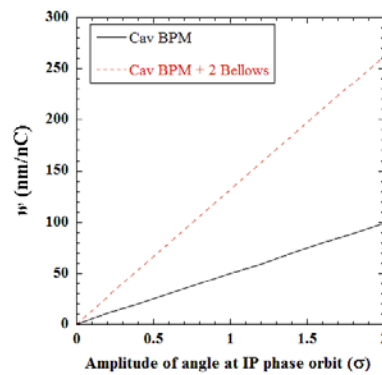
Figure 15: Calculated factor w, beam size increase due to wakefield, as a function of the amplitude of the "angle at the IP" orbit distortion.

In order to explain the experimental observation of $w{\sim}100$ nm/nC, the orbit amplitude has to be larger than 0.7-sigma, assuming there is a wakefield source equivalent to one cavity BPM and two bellows at each quadrupole magnet in the final focus line, and about 2-sigma assuming a wakefield source equivalent to one cavity BPM. Such large orbit variations would have been easily detected by our BPM system in the high betafunction region, therefore this effect can be excluded. The typical observed orbit jitter of the "angle at the IP" phase is about 0.2-sigma in usual operation.

2.3.6.4   *Summary*

Only very large misalignments or very large orbit jitter would explain the experimentally estimated intensity dependence, w~100 nm/nC,. and are inconsistent with our observations. It is possible that wakefields are underestimated in the calculations, or there may be significant wakefield sources which have not yet been considered. For example, wakefield calculations of the bellows may not be accurate enough due to difficulties defining the exact geometry; also, smaller discontinuities, such as narrow gaps between beam pipe flanges may produce significant wakefields, which have not yet been investigated.

2.3.7 **Comparison with ILC and CLIC**

Effect of the transverse wakefield in ILC BDS and CLIC BDS are roughly compared with ATF2 in this section. The effect of the wakefield is proportional to the bunch charge and the inverse of the beam energy. It is roughly proportional to a square root of the betafunction for the same level of misalignment, and proportional to the beta function for the same relative amplitude (relative to the beam size) of the orbit jitter. It is roughly proportional to the inverse of the square root of the emittance for the same level of misalignment. Effect of wakefields also depends on the bunch length (~7 mm, 0.3 mm, and 0.044 mm, in ATF, ILC and CLIC respectively) and the effects relative to the ATF case were roughly estimated to be about 0.3 for ILC and 0.04 for CLIC, with a big assumption of the same wakefield sources as in ATF2 beam line.

The comparison is summarized in Table 5, and the estimated total effects in ILC/CLIC-BDS are 0.1/0.008 and 0.08/0.002 of ATF2 for the same misalignment and for the same orbit jitter (relative to the beam size), respectively. It should be noted that this simplistic scaling does not include the wakefield produced by the collimators etc in ILC and CLIC, while there are no comparably small aperture devices in the ATF2 beam line.

Table 5, Rough comparison of transverse wakefield effect in ATF2, ILC-BDS and CLIC-BDS

	ATF2	ILC BDS	Relative Effect (ILC/ATF) misalignment / orbit jitter	CLIC BDS	Relative Effect (CLIC/ATF) misalignment / orbit jitter
Beam Energy	1.3 GeV	>100 GeV	<0.013	>500 GeV	<0.0026
Bunch Charge	~1nC	~3 nC	~3	~0.6 nC	~0.6
Bunch Length	~7 mm	0.3 mm	~0.3	0.044 mm	~0.04
Physical Emittance	12E-12 m	2E-14 m (100GeV)	4 / 1	2E-14 m (500GeV)	24 / 1
Peak β function	~9000 m	~60000 m	2.6 / 7	~250000 m	5.3 / 28
Total			0.1 / 0.08		0.008 / 0.002

2.3.7.1 *References*

1. Y. I. Kim *et al.*, "Cavity beam position monitor system for the Accelerator Test Facility 2", Phys. Rev. ST: Accelerators and Beams, **15,** 4, (2012), 042801.
2. ATF2 Proposal, KEK Report 2005-2.
3. P. Raimondi, A. Seryi, "Novel Final Focus Design for Future Linear Colliders", Phys. Rev. Lett. **86**, 7, (2001).
4. 15th ATF2 Project Meeting, 2013.
5. W. Bruns, "GdfidL: a finite difference program with reduced memory and CPU usage", PAC97, http://www.gdfidl.de
6. K. Ko *et al*., "Advances in Parallel Electromagnetic Codes for Accelerator Science and Development", SLAC-PUB-14349 (2011).
7. T. Naito *et al*., "Bunch Length measurement in the ATF damping ring", ATF Report, ATF-01-01 (2001).

8. A. Latina *et al.*, "Evolution of the tracking code PLACET", MOPWO053, IPAC13.

2.4   IP Feedback Prototypes for ILC and CLIC

Philip N. Burrows, on behalf of the FONT collaboration
John Adams Institute, UK
Mail to: p.burrows@physics.ox.ac.uk

A number of fast beam-based feedback systems are required at the International Linear Collider (ILC) [1]. At the interaction point (IP) a very fast system, operating on nanosecond timescales within each bunch train, is required to compensate for residual vibration-induced jitter on the final-focus magnets by steering the electron and positron beams into collision. The deflection of the outgoing beam is measured in a beam position monitor (BPM) and a correcting kick applied to the incoming other beam. A pulse-to- pulse feedback system is envisaged for optimising the luminosity on timescales corresponding to 5 Hz. Slower feedbacks, operating in the $0.1 - 1$ Hz range, will control the beam orbit through the Linacs and Beam Delivery System.

The key components of each such system are beam position monitors (BPMs) for registering the beam orbit; fast signal processors to translate the raw BPM pickoff signals into a position output; feedback circuits, including delay loops, for applying gain and taking account of system latency; amplifiers to provide the required output drive signals; and kickers for applying the position (or angle) correction to the beam. A schematic of the IP intra-train feedback is shown in Figure 1, for the case in which the beams cross with a small angle; the current ILC and CLIC designs incorporate crossing angles of 14 and 20 mrad respectively.
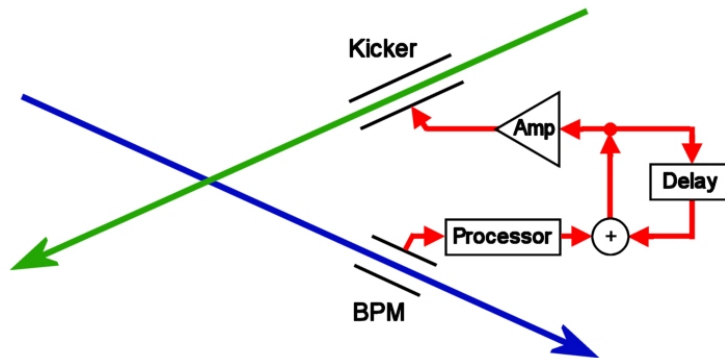
Figure 1: Schematic of IP intra-train feedback system with a crossing angle. The deflection of the outgoing beam is registered in a BPM and a correcting kick applied to the incoming other beam.

Critical issues for the intra-train feedback performance include the latency of the system, as this affects the number of corrections that can be made within the duration of the bunch train, and the feedback algorithm. We report the latest results on the development and beam testing of an ILC prototype system that incorporates a digital feedback processor based on a state-of-the-art Field Programmable Gate Array (FPGA) [2]. The use of a digital processor allows for the implementation of more sophisticated algorithms which can be optimised for possible beam jitter scenarios at ILC. However,

a penalty is paid in terms of a longer signal processing latency due to the time taken for digitisation and digital logic operations. This approach is possible for ILC given the long, multi-bunch train, which includes parameter sets with c. 3000/6000 bunches separated by c. 300/150 ns respectively. Initial results were reported previously in [3] and [4].

The ATF can provide an extracted train that comprises up to 3 bunches separated by an interval that is selectable in the range 140−300 ns. This provides a short ILC-like train which can be used for controlled feedback system tests. FONT5 has been designed as a bunch-by-bunch feedback with a latency goal of around 140 ns, meeting the minimum ILC specification of c. 150 ns bunch spacing. This allows measurement of the first bunch position and correction of both the second and third ATF bunches.

A schematic of the upstream FONT5 feedback system prototype and the experimental configuration in the upgraded ATF extraction beamline, ATF2, is shown in Fig. 2. Two stripline BPMs (P2, P3) are used to provide vertical beam position inputs to the feedback. Two stripline kickers (K1, K2) are used to provide fast vertical beam corrections. A third stripline BPM (P1) is used to witness the incoming beam conditions. Upstream dipole corrector magnets (not shown) can be used to steer the beam so as to introduce a controllable vertical position offset in the BPMs. Each BPM signal is initially processed in a front-end analogue signal processor. The analogue output is then sampled, digitised and processed in the digital feedback board. Analogue output correction signals are sent to a fast amplifier that drives each kicker.
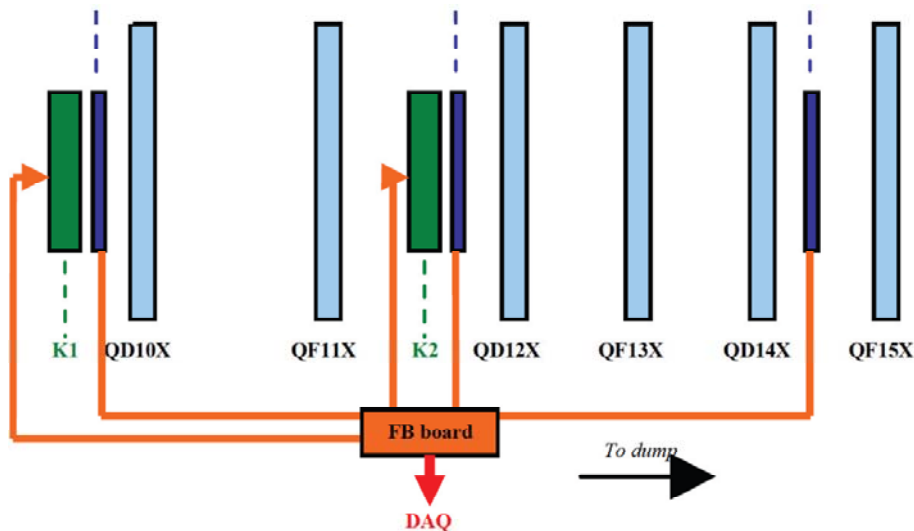
Figure 2: Schematic of FONT5 at the ATF2 extraction beamline showing the relative locations of the kickers, BPMs and the elements of the feedback system.

A schematic of the FONT ATF IP system is shown in Fig. 3. It comprises two C-Band cavity BPMs (IPA, IPB) and a stripline kicker (IPK). The upstream magnet QD0FF (also shown) can be used to steer the beam by introducing a vertical position offset or to move the beam waist up or down the beamline.
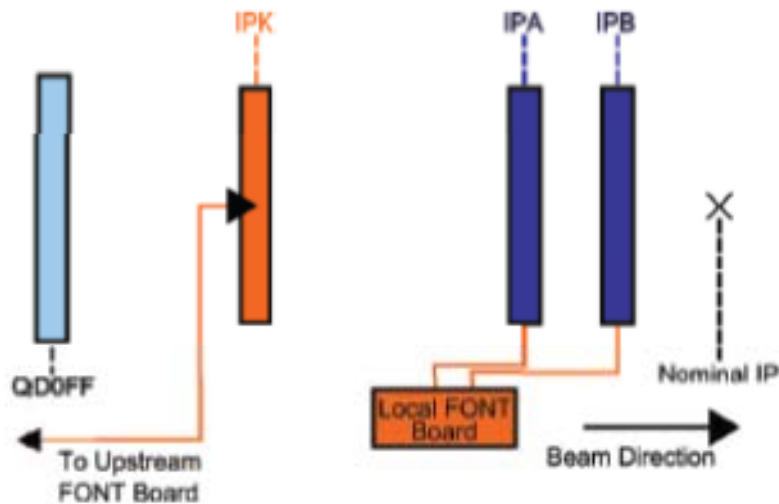
Figure 3: Schematic of IP region at the ATF2 final focus beamline showing the relative locations of the kickers, BPMs and the elements of the feedback system.

The design of the front-end stripline BPM signal processor is described in [5] and [6]. The top and bottom (y) stripline BPM signals are added with a resistive coupler and subtracted using a hybrid, to form a sum and difference signal respectively. The resulting signals are bandpass filtered and down-mixed with a 714 MHz local oscillator signal which is phase-locked to the beam. The resulting baseband signals are low-pass filtered. The hybrid, filters and mixer were selected to have latencies of the order of a few nanoseconds to yield a total processor latency of 10 ns [5,6]. The cavity BPM processing scheme described here [7] consists of a two stage system, the first downmixing the cavity signal to 714 MHz and the second to baseband. The baseband signal is then digitised by a local FONT5 digital board. In addition a high speed cable is strung along the beamline connecting the upstream and downstream systems and allowing a feed-forward signal to be transmitted between the two points.

Two custom digital feedback processing boards are installed at ATF, one upstream and one at the IP. On each board there are 9 analogue signal input channels in which digitisation is performed using ADCs with a maximum conversion rate of 400 MS/s, and 2 analogue output channels formed using DACs, which can be clocked at up to 210 MHz. The digital signal processing is based on a Xilinx Virtex5 FPGA [2]. The FPGA is clocked with a 357 MHz source derived from the ATF master oscillator and hence locked to the beam. The ADCs are clocked at 357 MHz. The analogue BPM processor output signals are sampled on peak to provide the input signals to the feedback. The gain stage is implemented alongside the reciprocal of the sum signal for beam charge normalisation via a lookup table stored in FPGA RAM. The delay loop is implemented as an accumulator in the FPGA. The output is converted back to analogue and used as input to the kicker amplifier. A pre-beam trigger signal is used to enable the amplifier drive output from the digital board.

The driver amplifier was manufactured by TMD Technologies [8] and provides ±30 A of drive current into the kicker. The rise-time is 35 ns from the time of the input signal to reach 90% of peak output. The output pulse length was specified to be up to 10 microseconds.

We report the results of beam tests of the system in 2012/13; earlier results were reported in [3] and [4]. The upstream coupled loop feedback system was recommissioned and its impact on the beam near the IP was measured. For the purpose of obtaining optimal spatial correlation between bunches in the extracted bunch train the ATF damping ring was set up to extract 2 bunches with a separation of 274.4 ns. The upstream system was first set up and the optimal gain was selected using the methods described in [4]. The system was then operated in an interleaved mode with the feedback applied on alternate machine pulses. IPA was then used to measure the effects of the system near the beam waist.

The performance of the system is shown in Fig. 4 which shows vertical beam position (jitter) of the second bunch in the two upstream feedback BPMs and IPA. With the feedback off the second bunch RMS jitter was measured to be $3.6 \pm 0.2 \mu m$ in P2, $3.7 \pm 0.2 \mu m$ in P3 and $3.9 \pm 0.2 \mu m$ in IPA. With feedback on the second bunch RMS jitter was measured to be $1.3 \pm 0.1 \mu m$ in P2, $1.4 \pm 0.1 \mu m$ in P3 and $2.6 \pm 0.1 \mu m$ in IPA. The level of correction upstream is as expected given the bunch to bunch correlations of 94% measured with the same data. Although a correction is seen at IPA it is clear that the level of jitter reduction seen in the upstream system does not propagate downstream fully; work is currently ongoing to improve the propagation of the jitter reduction.
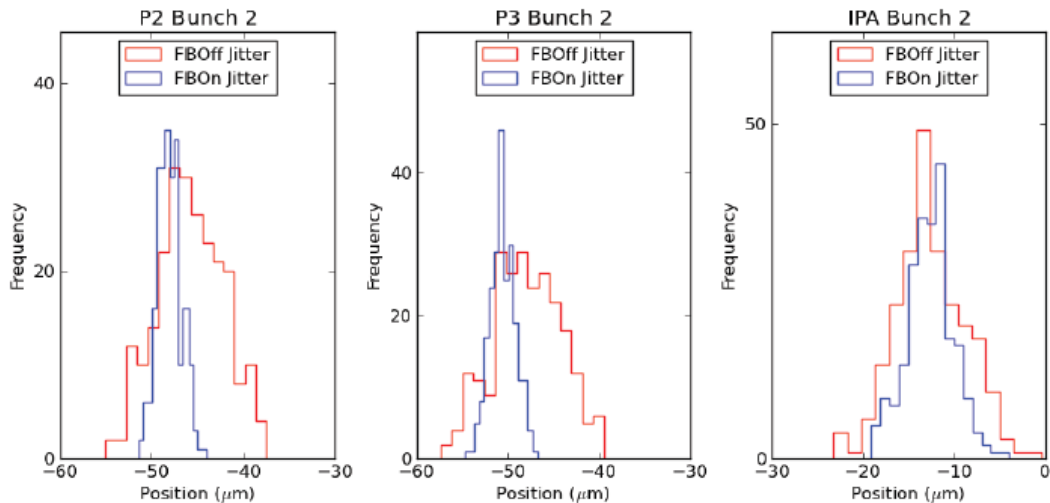
Figure 4: Distribution of vertical beam positions for the 2*nd* bunch for upstream feedback run.

In feed-forward the beam position is measured by the upstream system and the kick required to stabilise the beam calculated and converted to analogue. This signal is then output and sent down the high-speed cable to a kicker amplifier located in the IP region. The signal from this amplifier is then sent to the IP kicker. Via this approach it is possible to stabilise the beam locally near the IP. The accelerator was set up as previously to obtain the best possible bunch to bunch correlations. The beam waist was moved to be close to IPB using the QD0FF magnet. The system was operated in interleaved mode with the feed-forward correction applied on every other machine pulse. The performance of the system in this mode is shown in Fig. 5. With feed-forward off the second bunch jitter was measured to be $4.5 \pm 0.2 \mu m$, with the feed-forward correction applied the second bunch jitter was measured to be $2.9 \pm 0.1 \mu m$. The jitter in the upstream BPMs remained unaffected and IPA was not calibrated for this

experiment. A clear feed-forward correction was observed. Work is currently ongoing to try and improve the level of performance achieved via gain optimisation.
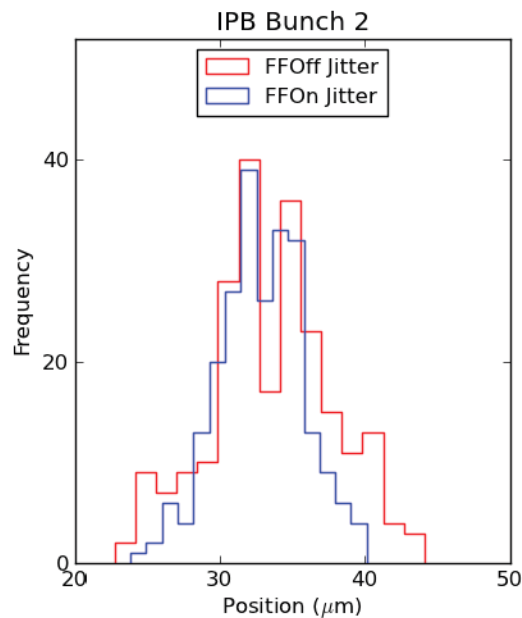
Figure 5: Distribution of vertical beam positions for the 2*nd* bunch in IPB for feed-forward operation.

2.4.1.1 *References*

1. http://www.linearcollider.org/cms/
2. http://www.xilinx.com/products/virtex5/index.htm
3. R. Apsimon *et al.*, Proceedings IPAC11, 2011, MOPO17.
4. D. Bett *et al.*, Proceedings IPAC12, 2012, WEPP068.
5. D. Bett *et al.*, Proceedings IPAC12, 2012, MOPPR065.
6. D. Bett *et al.*, Proceedings IPAC13, 2013, MOPWAO57.
7. Y. I. Kim, PhD thesis, Kyungpook National University, 2012.
8. www.tmdtechnologies.co.uk

2.5 Instrumentation for the LC Final Focus System

2.5.1 ATF2 and LC Cavity Beam Position Monitor Systems

S. T. Boogert, F. Cullinan, A. Lyapin and J. Snuverink
John Adams Institute at Royal Holloway, Department of Physics, RHUL, UK

Y. I. Kim, John Adams Institute at University of Oxford, , UK
A. Aryshev, Y. Honda, T. Tauchi and N. Terunuma
High Energy Accelerator Research Organization (KEK), Japan

G. White, D. J. McCormick, J. Nelson, T. Smith
SLAC National Accelerator Laboratory, USA

Mail to: Stewart.Boogert@rhul.ac.uk

2.5.1.1 *Introduction*

The ATF2 and Linear Colliders (LCs) have strong requirements on the beam position diagnostics to be used, typically sub-micrometer down to few nanometres resolutions are required. Until relatively recently position measurement devices of this resolution have only existed as experimental systems. Cavity Beam Position Monitors (CBPMs) have been successfully tested in numerous experiments, which have consisted of either closely spaced triplets [1, 2] or used with specialized optics configurations, like a ballistic beam in the case of [3, 4]. They have gained traction within the Free Electron Laser (FEL) light source community. Three full-scale production systems have been operating at LCLS [5], FERMI@ELETTRA [6] and SACLA [7].

Among the various types of BPMs, such as the electrostatic BPM using four button-pickups or the strip-line type BPM, only the cavity CBPMs has a potential for achieving resolutions in the nanometre range and the center accuracy at the micrometre level. In order to achieve the ATF2 goal of a small beam size at the focus point the beam must be aligned to within 1 to 100 μm of the magnet centers, depending on the particular magnet. Studies of LC requirements yield a beam to magnet center accuracy 100 nm to 100 μm [4]. All beam based alignment techniques are dependent on the BPM resolution and stability, so a full test of CBPMs with resolutions required for ILC is highly valuable.

The ATF2 CBPM system is of a similar scale as compared with the FEL light sources but differs in two major respects. Firstly, the ATF2 is a challenging test lattice with large beam size variations and often altered optics configurations. This leads to complications in BPM calibration and performance at ATF2. Secondly, the ATF2 environment is not ideally suited for high-resolution radio frequency (rf) phase detectors, unlike the modern FEL installations, which require high degree of thermal stabilization and low phase noise and jitter timing signal distribution. The ATF2 does however provide a unique and flexible facility to test the operation of high performance cavities for a future linear collider where the beam delivery systems are optically complex and require cavity BPMs in the order of thousands of devices.

2.5.1.2 *Principle of Operation*

The allowed modes of a cavity are determined by the geometry of the cavity, with cylindrical and rectangular cavities typically used. The transverse magnetic (TM) cavity modes are excited by the passage of the particle bunch. The lowest frequency monopole mode field magnitude is typically only linearly dependent on the bunch charge q. The next highest frequency mode is dipole in shape and bi-linearly dependent on bunch charge and position d. The cavity is coupled to waveguide couplers that filter the dipole, position sensitive mode, which is subsequently coupled in to a coaxial cable. In general the voltage signal $V_{dipole}(t)$ as a function of time t induced from a cavity is of the form

$$V_{dipole}(t) = q\, e^{-t/\tau_{dipole} - i\omega_{dipole}t}(A_d d + A_{d'} d'\, e^{\pi i/2} + A_\theta \theta e^{-\pi i/2}), \qquad (1)$$

where ω_{dipole} is the dipole mode angular frequency, τ_{dipole} is the exponential decay time of the cavity signal, d is the bunch displacement, d' is the bunch trajectory angle and θ is the bunch tilt, with corresponding constants of proportionality A_d, $A_{d'}$ and A_θ that depend on the coupling of the bunch to cavity mode. From Equation 1 the position

sensitive signal is 90 degrees out of phase compared with the signals excited due to trajectory angle and bunch tilt. The idea of exploiting CBPMs as bunch tilt and trajectory monitors has been envisioned but rarely exploited. This remains the case for CBPMs used at the ATF2 and considered for future LCs. To extract the beam position using Equation 1, an independent measurement of the beam charge and arrival phase is required. This is done using a *reference* cavity with a monopole mode with the same frequency as the position cavity; the output signal has the following form

$$V_{monopole}(t) = qA_q e^{-t/\tau_{monopole} - i\omega_{monopole}t} \ , \tag{2}$$

where $\omega_{monopole}$ is the monopole mode angular frequency $\tau_{monopole}$ is decay time and A_q is a constant of proportionality that depends on the cavity coupling to beam. Typically the monopole and dipole cavities are engineered to have identical as reasonably possible frequencies and decay times. In general there is an arbitrary phase shift between V_{dipole} and $V_{monopole}$ due to different delays in electronics and cables. In general a single phase and proportionality constant is required to convert the ratio of the two voltages from Equations 1 and 2 to a beam position.

2.5.1.3 *ATF2 Cavity BPM system*

The cavities used at ATF2 are based on previous developments with CBPM systems at the ATF [2]. This report is based on and extends the work reported in [9]. The C- and S-band cavity systems are similar enough to be discussed as one system, where differences exist they are highlighted in the relevant section. The BPMs are used for dispersion measurement, optics model verification, beam based alignment and beam feedback and steering applications. Figure 1 shows the layout of the ATF2 with the quadrupoles containing a CBPM marked.
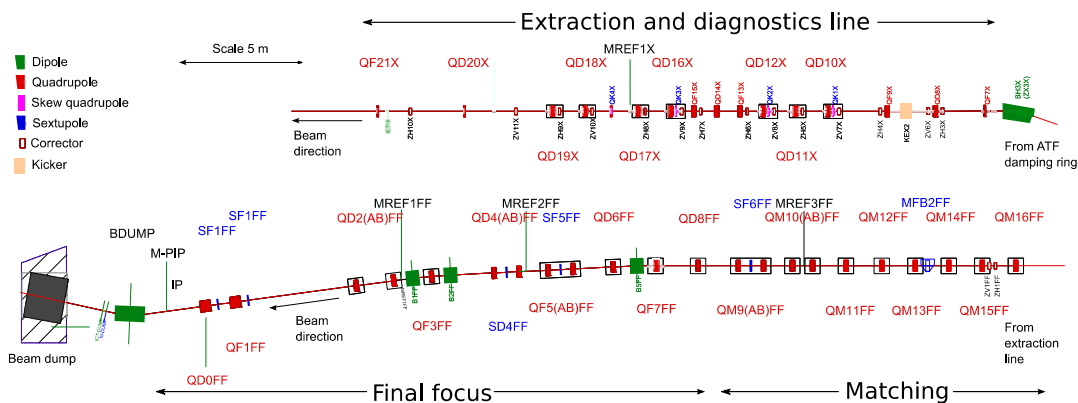
Figure 1: Layout of the ATF2 with quadrupoles with CBPMs highlighted

The ATF2 is instrumented with three types of CBPMs, referred to as C-band, located in most quadrupoles, S-band with large aperture in the final focusing section and finally interaction point (also C-band). Photographs of the C- and S-band cavities are shown in Figure 2. The cavities are cylindrical with monopole suppressing waveguides that extract the position sensitive dipole cavity mode. Some important

parameters of the cavities are given in Table 1. All the CBPMs discussed have rotationally symmetric set of 4 ports, two for each dipole mode polarisation.
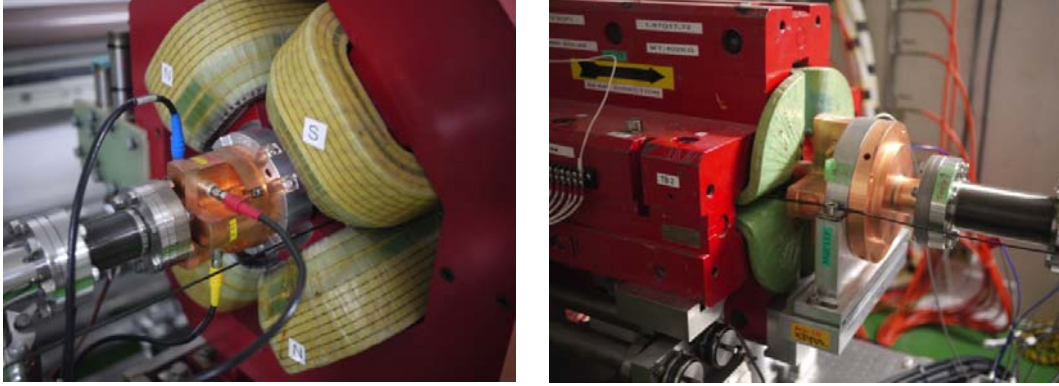
Figure 2: Photographs of the C- (left) and S-band (right) CBPMs installed inside ATF2 quadrupoles.

Table 1: Cavity parameters for C- and S-band devices. Frequencies and isolation measured in air, while Q_L and R/Q are values from electromagnetic simulation.

Parameter	C-band	S-band
Frequency (GHz)	6.423	2.888
Isolation (dB)	45	40
Shunt impedance-Q ratio R/Q at 1 mm (Ω)	1.4	0.15
Sensitivity (V/mm/nC)	0.8	0.3

The ATF2 started with 33 C-band dipole cavities and 4 C-band reference cavities and 4 S-band dipole cavities and a single S-band reference. Over the course of ATF2 operation, three of the C-band reference cavities and two of the S-band BPMs in the final quadrupole doublet were removed and the focus point was instrumented with a special interaction point cavity with low-Q and strong coupling to the beam [8].

The ATF2 CBPM system can be divided into the following sub-systems: cavity, rf signal processing electronics, digital signal processing, local oscillator (LO) and test tone signals, calibration procedure and software controls.

2.5.1.3.1 Electronics and Signal Processing

The signals from the two output ports for a given direction are combined using a hybrid to increase signal amplitude. The electronics for the C and S band CBPMs consist of an amplification stage, single image rejection mixer down-converters and filtering with gains of 25 dB and 10 dB respectively. The other parameters of the rf electronics is given in Table 2.

Table 2: The rf signal processing electronics parameters.

Parameter	C-band	S-band
Frequency (GHz)	6.423	2.888
Noise floor (dBm)	-93	-80
1 dB compression point (dBm)	-20	10
Gain (dB)	25	10
Bandwidth (MHz)	50	50
Noise figure (dB)	11	18
X-Y cross talk (dB)	-59	NA

Most of the C-band CBPM output signals are attenuated by 20 dB, after the hybrid, to avoid saturation of the rf electronics and digitiser system and simplify the digital processing algorithm. The local oscillator (LO) signals for the C-band rf electronics are generated by dedicated phase locked electronics in the case of the C-band system and a low noise (but not phase locked) synthesiser for the S-band system. The intermediate frequency (IF) signals are digitised by 100 MHz Struck 8 channel, 14-bit waveform VME digitisers. The VME processor-controller publishes the waveform data through EPICS.

The digital signal processing is a digital down-conversion algorithm used extensively for cavity BPM signals [2]. The IF signal from the electronics are digitized and then mixed digitally using a complex local oscillator of frequency ω_{DDC} to base-band and filtered using a Gaussian time domain filter, with a bandwidth of approximately 3 MHz to remove the $2\omega_{DDC}$ signal. The down-converted and filtered complex valued signal can be written as

$$y_{DDC}(t_i) = \sum_{j=0}^{n \text{ samples}} g(t_j - t_i)\exp(i\omega_{DDC})y_{dig}(t_j) \tag{3}$$

where $g(t)$ is the Gaussian filter and $y_{dig}(t_i)$ is the digitized waveform signal. For each cavity the DDC LO frequency must be chosen to leave a baseband signal. This is done by taking approximately 20 pulses of waveform data and down-converting the signal until there is no phase variation as a function of sample number, as clearly seen in Figure 3.

The amplitude A and phase ϕ of the signal are measured at a single time t_{sample} so

$$\begin{aligned} A &= |y_{DDC}(t_{sample})| \\ \phi &= \arg\left[y_{DDC}(t_{sample})\right] \end{aligned} \tag{4}$$

The raw IF signal and processing steps are shown in Figure 3. The signal is first pedestal subtracted and the calibration tone removed. Then the signal is down-converted to baseband using Equation 3 and the signal amplitude and phase calculated using Equation 4. The amplitudes and phases are calculated in the same way for all the dipole and monopole cavities.
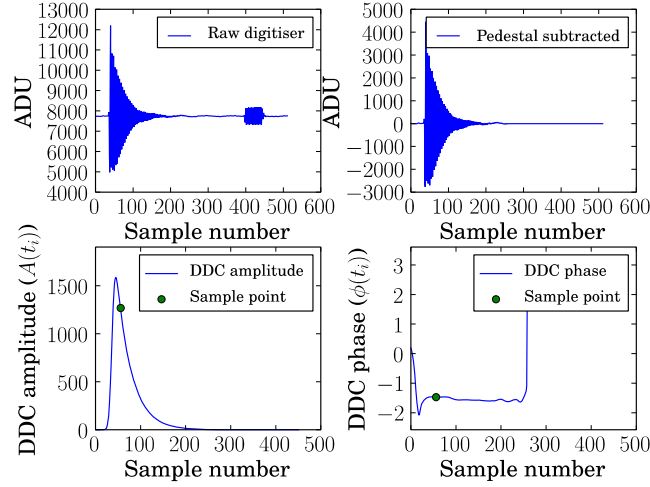
Figure 3: Example signals and signal processing for a single down-converted waveform. Top left is the raw signal, top right is the background subtracted signal, bottom left is the down-converted and filtered amplitude and bottom right is the down-converted and filtered phase.

From Equations 1 and 2, it is clear the bunch charge dependence must be removed and the phase of the dipole signal measured compared to a monopole signal. In-phase I and quadrature Q phase signals are calculated from the dipole and monopole amplitudes and phases as follows

$$I = \frac{A_d}{A_m}\cos(\phi_d - \phi_m)$$
$$Q = \frac{A_d}{A_m}\sin(\phi_d - \phi_m)$$

(5)

Usually the onset of saturation of the rf electronics is set to be at larger signal levels than the saturation of the digitiser system. Even if there is some form of signal saturation, it is still possible to recover beam position information by performing the analysis described but using signals recorded later in time, after the saturation has passed and the signal has decayed somewhat, although at reduced resolution.

2.5.1.3.2 Calibration

There are two methods employed to calibrate the CBPM, firstly the quadruple holding the CBPM can be moved using the magnet mover system or the beam can be kicked using an orbit bump.

Starting from QM16FF, the magnets with the BPMs mounted on their poles are placed on movers. The movers, originally developed and used for the Final Focus Test Beam experiment are fully automated and capable of positioning magnets weighing up to 600 kg to a few microns over a range of several millimetres. There are CBPMs before QM16FF are rigidly fixed inside quadrupoles, the calibration of these devices require a beam bump that is created using upstream corrector magnets. This does have an ambiguity in that ab-initio calibration requires a reasonable understanding of the optics, although the calibration calculations are performed in the same way as for a quadrupole mover.

An example mover calibration is shown in Figure 4. The quadrupole containing the CBPM is typically moved over 500 micrometres in 5 to 10 steps and at each step 10 to 20 machine pulses are recorded, where typically only I and Q values are recorded.
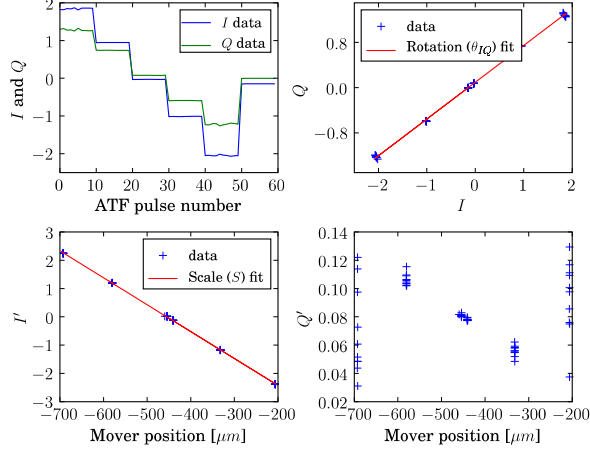
Figure 4: Example mover calibration of a single BPM.

The in-phase and quadrature-phase signals can be related to displacement via

$$d = S\left(I\cos\theta_{IQ} + Q\sin\theta_{IQ}\right)$$
$$d' = S'\left(-I\sin\theta_{IQ} + Q\cos\theta_{IQ}\right)$$

(6)

where S is the scaling to position and θ_{IQ} accounts for the relative phase between the dipole and monopole signals. Assuming the beam is purely moved in position then θ_{IQ} is determined via a fit to Q as a function of I (shown in the top right of Figure 4). Then rotating to $I' = I\cos\theta_{IQ} + Q\sin\theta_{IQ}$ and $Q' = -I\sin\theta_{IQ} + Q\cos\theta_{IQ}$, the position phase is clearly separated from the bunch trajectory and tilt (shown in the bottom two plots of Figure 4). Having obtained the correct rotation, the scale calibration can be identified as the gradient of a linear fit of I' to mover (or beam) position (shown in the bottom left plot of Figure 4). Provided there is no angular motion of the BPM the signal left in the quadrature phase should be small.

2.5.1.3.3 Test Tone and Calibration Stability

With each machine pulse a continuous wave radio frequency tone is injected, after the beam induced signal into the electronics for both the dipole and monopole cavity electronics, which can be seen in the top left hand plot of Figure 3. The test tone data processed in the same way as the CBPM data is used to monitor possible gain and phase variations in the processing electronics. Completely analogously to the CBPM signal, I_{test} and Q_{test} are calculated for each channel. The variations in the test tone amplitude and phase are cancelled in the calculation of I_{test} and Q_{test}, see Equation 5. Furthermore, coherent changes in dipole and reference channel gain and phase are also removed, only leaving the differences between the two channels. Only incoherent changes between dipole and reference channels can affect the position measurement. Analysis of the test

tone data covering 4 days, showed that the electronics drifts did not on average exceed $\pm 0.99\%$ in amplitude and $\pm 0.57^\circ$ in phase, shown for all CBPM channels in Figure 5.
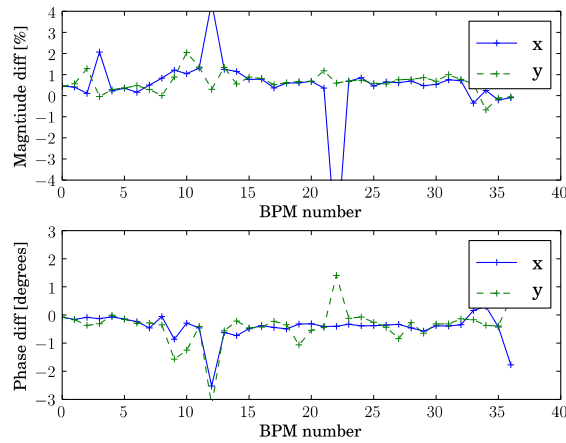
Figure 5: Two measurements of the processing electronics relative amplitude and phase separated by 4 days.

To test the operating system stability, the calibration procedure was repeated as frequently as possible over a two-week period and the calibration constants recorded for all BPMs in both directions shown in Figure 6. The IQ rotation angle does not vary more than 1 degree, whilst the scale factor varied by about 5%, clearly inconsistent with the test tone measurements of Figure 5. This discrepancy can be explained by the beam motion whilst the calibration is being performed, by subtracting the beam jitter using the CBPMs upstream of the CBPM being calibrated the scale factors vary by less than 1%, in agreement with the rf electronics test tone measurement.
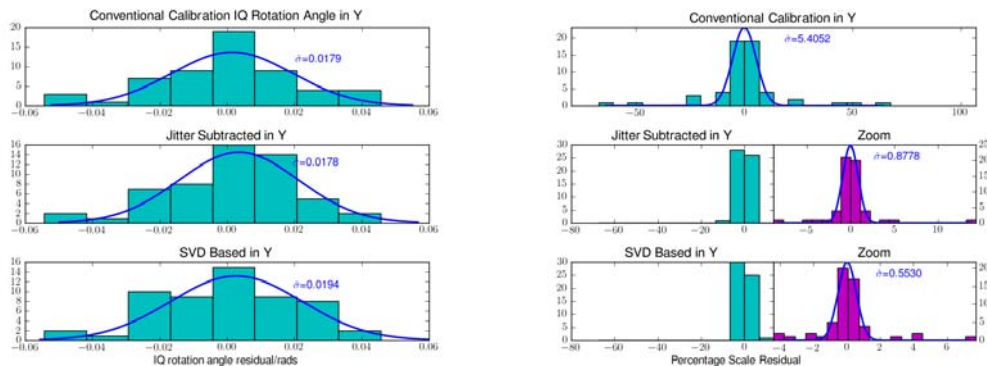
Figure 6: Histograms of the calibration constants for many BPMs over a two week period. Left: is the phase rotation θ_{IQ}. Right: is the scale factor S.

2.5.1.3.4 System Performance

The CBPM system performance is mainly determined via the single device resolution. This cannot be measured independently from CBPMs. The resolution of a BPM was investigated using a model independent analysis (MIA) as the beam motion is typically two or three orders of magnitude larger than the CBPM resolution. After the

calibration procedure is performed for all the CBPM the x and y CBPM positions were recorded for approximately 250 machine pulses. The position data d_{ij} for machine pulse i and BPM k is used to construct a linear system of equations of the form

$$d_{ik} = \sum_{j \neq k} d_{ij} v_j, \qquad (7)$$

where v_j is a set of correlation coefficients relating the positions in all the other CBPMs apart from the kth CBPM to the measured position in the kth BPM d_{ik}. The correlation coefficients are determined by inverting the data matrix d_{ij} using singular value decomposition (SVD). Having determined the correlation coefficients it is straight forward to determine a predicted position in a given BPM given the set of spectator BPM measurements. The values used in the data matrix do not just have to be beam position but could alternatively be in-phase and quadrature-phase signal values and of course include both horizontal and vertical BPM information to remove the effects of device roll around the beam axis. This SVD method is applied for each BPM and the position residual can be calculated for each position measurement so

$$\delta d_i = d_i - \sum_{i \neq j} d_j v_j \quad . \qquad (8)$$

The quoted CBPM resolutions are the root mean square (RMS) of this position residual. This measure is an over-estimate of the CBPM resolution but the error associated with the prediction from the spectator CBPMs is typically smaller than the single device resolution. The resolution of each device is plotted in Figure 7, for two different beam orbit settings, one where the beam is well steered in the entire ATF2 and another where the beam has been steered to the centre of a triplet of CBPMs where the 20 dB attenuators have been removed. The same CBPM resolution data is plotted in Figure 8 as a histogram.
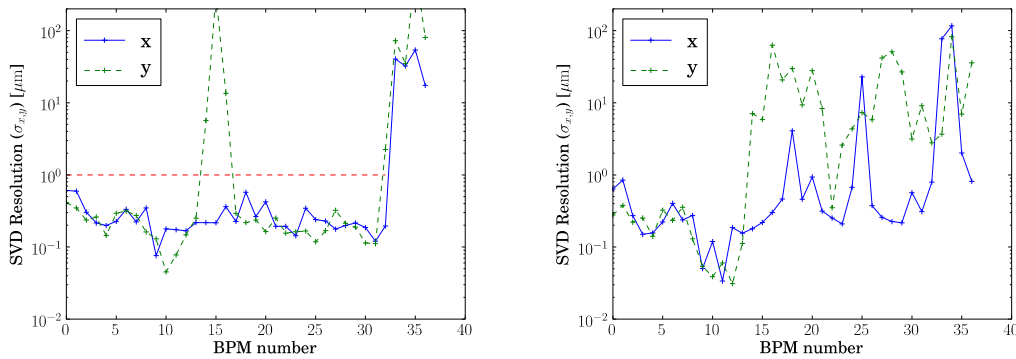
Figure 7: Horizontal and vertical resolution as function of BPM number along the ATF2. Left : with normal orbit, Right : with beam steered to centre of 3 CBPMs without attenuators (9,10,11)
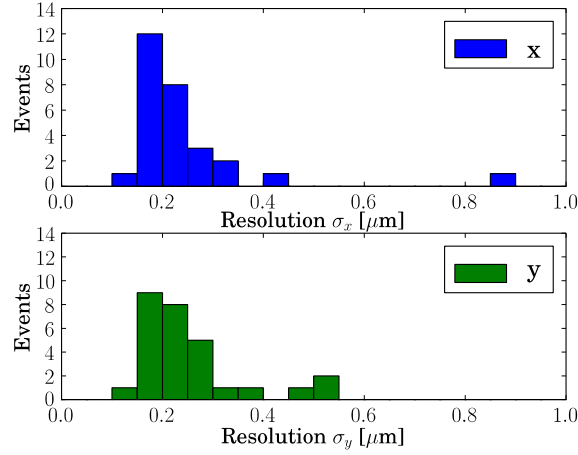
Figure 8: Histogram of horizontal (top) and vertical (bottom) resolution of the C-band CBPMs.

With attenuators the average resolution is 250 nm in both the horizontal and vertical directions, without attenuators the beam recorded resolution is 30 nm, again consistent in both axes.

2.5.1.3.5 Systematic Effects

Although designed to operate at bunch populations of 10^{10} electrons per bunch, the wake-field effects described in Section 2.3 have pushed operation of the CBPM system with lower bunch charges. As the position is calculated as the ratio of two voltages ($V_{dipole}/V_{monopole}$), the statistical uncertainty scales as $\sim 1/q$, including an irreducible constant uncertainty in quadrature gives a charge dependence of the following form

$$\sigma_d = \sqrt{\frac{A}{q^2} + B^2} \, ,$$

where A and B are constants. Figure 9 shows the measured resolution, for a CBPM without attenuation, as function of bunch charge, which was varied by changing the photo-injector laser power. Even at bunch populations of 7.5×10^8 electrons per bunch, the resolution is below 100 nm. At higher charges it asymptotically tends to a value of approximately 27 nm.
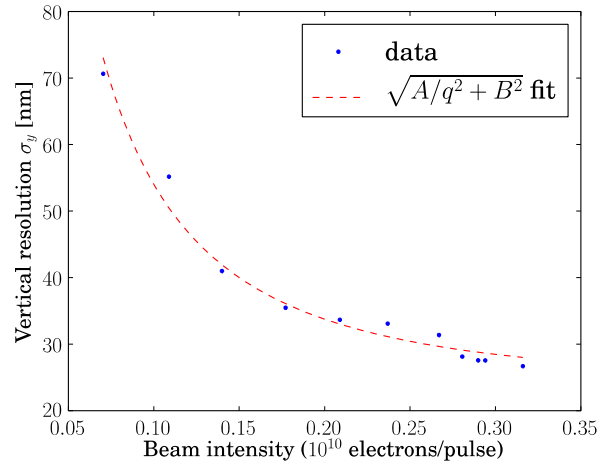
Figure 9: Resolution as a function of bunch charge, for a single CBPM without attenuation.

The bunch length is of central importance to the wake-field studies presented in Section 2.3 as the peak wake potential depends on the bunch length. During wake-field measurement shifts the damping ring (DR) accelerating gap radio voltage was varied between 0.22 and 0.32 MV which corresponded to a bunch length change from 31 ps to 21 ps. The calibration procedure was repeated for a single CBPM at three different voltages and also the resolution was measured, shown in Figure 10. There was no clear systematic effect of bunch length on the calibration constants, as expected and only a weak dependence of the resolution.
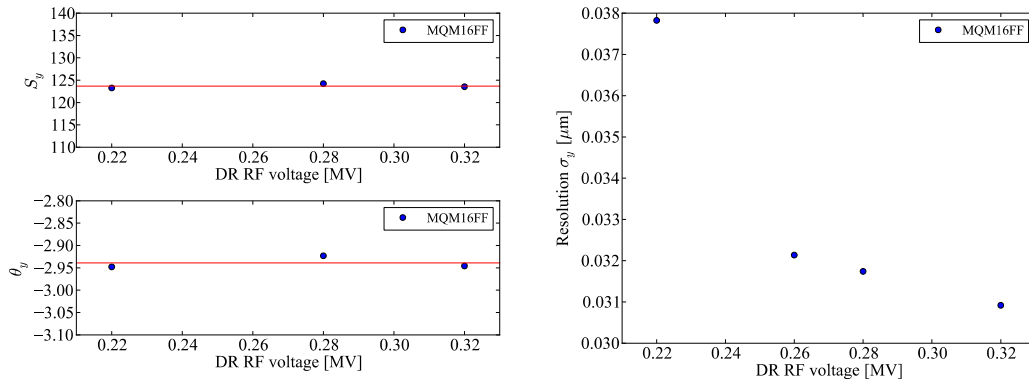
Figure 10: Left: variation of calibration constants as function of damping ring rf voltage. Right: variation of a single BPM resolution as function of damping ring rf voltage.

Still to be investigated is the effect of saturation on the device resolution. It can be seen in Figure 7 that poor steering the beam-line leaves large offsets in some CBPMs and hence poor resolution. This is difficult to quantify as moving a CBPM also causes a downstream orbit change, which effects the resolution of spectator CBPMs.

2.5.1.4 *LC Position Diagnostics*

The requirements for the two proposed LC designs both require CBPMs in large numbers. The resolution requirement for the ILC is typically hundreds of nanometers whilst the requirement for CLIC is more in the tens of nanometres. The CBPM system

as developed for the ATF2 is quite suitable for the ILC, where the bunch spacing is sufficiently large that the signals from subsequent bunches do not interfere in the cavity. The situation is not so clear for CLIC, where it is impossible to separate the cavity signal from each bunch.

2.5.1.5 *Conclusions*

The ATF2 cavity CBPM system is one of the largest installed and operating, with 4 S-band and 33 C-band position sensitive cavities. The C-band cavity system operates well with a resolution of approximately 250 nm and 30 nm in CBPMs with and without attenuators respectively. Figure 7 shows the distribution of vertical and horizontal BPM resolutions for all the attenuated C-band BPMs (with resolutions below $1 \mu m$). At the planned operating single bunch charge of 1×10^{10} electrons per bunch the resolution should be stable at 30 nm without attenuators.

The lessons learned from the development and use of CBPMS at ATF2 and the application at an LC are the following:

1. Independent calibration of BPMs, so multiple BPMs can be calibrated simultaneously. Each CBPMs for example could be placed on its own mover system within each quadrupole.

2. Further specification of the diagnostics requirements are needed for ILC and CLIC as temporal and spatial resolution requirements are not sufficient.

3. CBPMs are not fixed resolution devices and the resolution depends on the beam offset and charge within the device. A CBPM with heterodyne electronics and waveform digitization can still be used to provide position measurement when there is a large beam offset, although at degraded resolution.

4. Identification of common elements to all CBPMs to try and keep as much of the rf electronics and signal processing common between different devices.

5. Mitigate the effect of the optics on diagnostics device calibrations, so CBPMs should be placed upstream of the quadrupole so the magnets strength does not affect the calibration constants.

6. Variable attenuation and phase control would be beneficial as all BPMs could be run with similar performance characteristics.

2.5.1.6 *References*

1. T. Slaton, G. Mazaheri, and T. Shintake, "Development of nanometer resolution c-band radio frequency beam position monitors in the final focus test beam" (1998), SLAC-PUB-7921.
2. S. Walston, S. Boogert, C. Chung, P. Fitsos, J. Frisch, J. Gronberg, H. Hayano, Y. Honda, Y. Kolomensky, A. Lyapin, *et al.*, NUCLEAR INSTRUMENTS A 578, 122 (2007), ISSN 0168-9002.
3. M. Slater, C. Adolphsen, R. Arnold, S. Boogert, G. Boorman, F. Gournaris, M. Hildreth, C. Hlaing, F. Jackson, O. Khainovski, *et al.*, NUCLEAR INSTRUMENTS A 592, 201 (2008), ISSN 0168-9002.
4. A. Lyapin, H. Schreiber, M. Viti, C. Adolphsen, R. Arnold, S. Boogert, G. Boorman, M. Chistiakova, F. Gournaris, V. Duginov, et al., JOURNAL OF INSTRUMENTATION 6, P02002 (2011).
5. A. Young, R. G. Johnson, S. Smith, and R. M. Lill, in Proceedings of BIW10, Santa Fe,

New Mexico, US (2010).

6. R. De Monte, A. O. Borga, P. Craievich, M. Ferianis, G. Gaio, M. Predonzani, and M. Dal Forno, in Proceedings of DIPAC2011, Hamburg, Germany (2011).

7. H. Maesaka, S. Inoue, T. Ohshima, S. Matsubara, A. Higashiya, M. Yabashi, T. Shintake, Y. Otake, H. Ego, K. Yanagida, et al., in Proceedings of DIPAC09, Basel, Switzerland (2009)

8. Y. Inoue, H. Hayano, Y. Honda, T. Takatomi, T. Tauchi, J. Urakawa, S. Komamiya, T. Nakamura *et al.* PHYSICAL REVIEW SPECIAL TOPICS – ACCELERATORS AND BEAMS 11, 062801 (2008)

9. Y. I. Kim *et al*., PHYSICAL REVIEW SPECIAL TOPICS ACCELERATORS AND BEAMS 15 (4) (2012) 042801.

2.5.2 High Resolution Laserwire System for Linear Colliders at the ATF2

L. J. Nevay G. A. Blair, L. C. Deacon, P. Karataev, K. Kruchinin and S. T. Boogert
John Adams Institute at Royal Holloway, UK

L. Corner and R. Walczak
John Adams Institute at University of Oxford, UK

A. Aryshev, J. Urakawa and N. Terunuma
High Energy Accelerator Research Organization (KEK), Japan
Mail to: laurie.nevay@rhul.ac.uk

2.5.2.1 *Introduction*

The extraction line laserwire system at the Accelerator Test Facility 2 (ATF2) at KEK, Japan, is a system developed to achieve a precise transverse beam profile measurement of an electron beam. The development of such a diagnostic capable of measuring mircometre-size beams will be crucial in future linear accelerators such as the ILC and CLIC where the small beam sizes and high charge densities are beyond the operating capabilities of current diagnostic techniques [1,2].

The laserwire at the ATF2 aims to demonstrate a $1\,\mu$m transverse beam profile measured using the Compton-scattered photons from a tightly focussed laser beam. The laser beam is scanned transversely modulating the flux of the Compton-scattered photons, which travel near parallel to the electron beam and are measured in a detector downstream after a bend in the beamline.

A laserwire installation at the ATF2 [3] was upgraded and commissioned in 2010 demonstrating initial transverse beam size measurements of 8.0±0.3 μm [4]. This system was moved to a different point in the ATF2 lattice where a micrometre scale beam could be realised. This paper presents the recent results of this laserwire system demonstrating high-resolution measurements of the electron beam, even with a large aspect ratio beam that is conventionally thought to limit the use of a laserwire.

2.5.2.2 *Experimental Setup*

The laserwire was relocated in summer 2011 to the beginning of the ATF2 final focus section where strong, closely spaced matching quadrupoles allow a vertical electron beam size of ~1 μm to be achieved. The position of the laserwire interaction point in the ATF2 extraction line is shown in Figure 1.
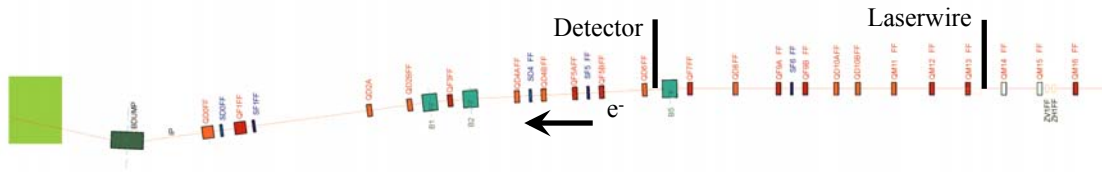
Figure 1: ATF2 extraction line lattice with laserwire and laserwire detector locations.

The laser system consists of a Q-switched Nd:YAG amplifier seeded by a 357 MHz mode-locked oscillator that is locked by external frequency reference to the ATF2 master oscillator. The laser output is frequency-doubled delivering ~150 mJ pulses with a wavelength of 532 nm at the 1.3 Hz repetition rate of the ATF2 1.3 GeV electron bunches. The laser pulses are $\sigma_\tau \approx 77$ ps long and the electron bunches are $\sigma_\tau \approx 30$ ps long. The laser is located outside the accelerator enclosure and transported into it in free-space with mirrors before being focused by an aberration corrected fused silica lens to the laserwire interaction point. A telescope consisting of two lenses is used to manipulate the divergence of the laser beam to control the size of the laser beam on the laserwire lens system to provide the minimum focussed laser beam spot size at the interaction point.

The Compton-scattered photons are detected approximately ten metres downstream immediately after a dipole magnet. The detector consists of a $4\times4\times0.6$ cm lead plate followed by a similarly sized piece of silica Aerogel that acts as a Cherenkov radiator. A light tight pipe guides the Cherenkov light to a shielded photo-multiplier tube out of the horizontal accelerator plane. A data acquisition system based on EPICS is used to synchronously record data from the laserwire experiment as well as the extraction line cavity BPM system [5] and other ATF2 diagnostics.

The laser pulses and electron beam were synchronised for collisions using an optical transition radiation (OTR) screen mounted in the laserwire chamber [6]. The laser beam was directed below this and both the attenuated laser light and the OTR were detected in an avalanche photodiode negating any issues of detector synchronicity. The laser timing was adjusted until both were overlapped. The OTR screen was also used as an alignment tool by comparing the bremsstrahlung radiation as the screen was lowered into the electron beam to the referenced focus spot position of the laser relative to the screen. This method allowed immediately detectable collisions between the laser and the electron bunches, which were subsequently optimised to maximise the Compton signal. The geometry of the laserwire interaction point is shown in Figure 2.
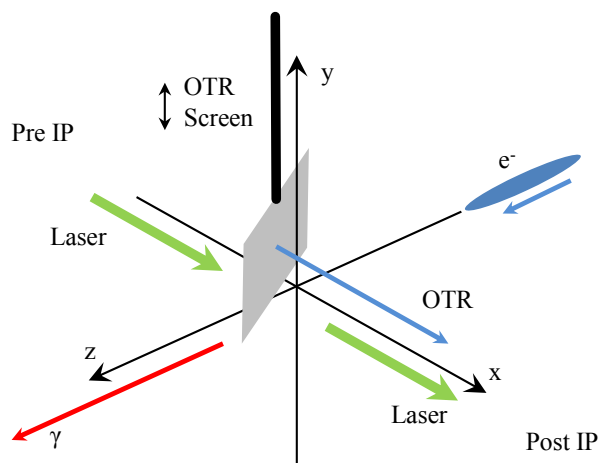
Figure 2 : The axes of the laserwire interaction point showing the electron beam, laser and OTR propagation.

2.5.2.3 *High Aspect Ratio Electron Beam*

The electron beam at the laserwire location in the ATF2 lattice is approximately 100 μm ×1 μm in the horizontal and vertical planes respectively. The laser spot size $\sigma(x)$ about a focus at location $x_{\sigma o}$ of size σ_o is described by

$$\sigma(x) = \sigma_o \sqrt{1 + \left(\frac{(x - x_{\sigma o})}{x_R} \right)^2} \tag{1}$$

where x_R is the Rayleigh range; the distance from the centre for the laser radius to increase by a factor of $\sqrt{2}$. The Rayleigh range is dictated by the wavelength λ of the light and the spatial quality described by a linear scaling factor M^2.

$$x_R = \frac{\pi(2\sigma_o)^2}{M^2 \lambda} \tag{2}$$

In the case where the laser beam size is effectively constant across the electron beam, the laserwire scan is the convolution of the electron beam profile and the Gaussian transverse profile of the laser beam and can be easily deconvolved [7]. However, in the case of the ATF2 laserwire, where a visible wavelength is used to create a focussed laser spot size of $\sim 1 \,\mu\text{m}$, the laser divergence across the electron beam is unavoidable. Figure 3 shows a schematic of the electron beam and the laser diameter depicting that even when the focussed spot of the laser is not overlapping with the electron beam, the divergent laser beam continues to interact with the electron beam. To deconvolve the laserwire scans, the full overlap integral of the laser and electron beams must be used. This requires knowledge of the horizontal electron beam size to ascertain the vertical electron beam size from the laserwire scan.
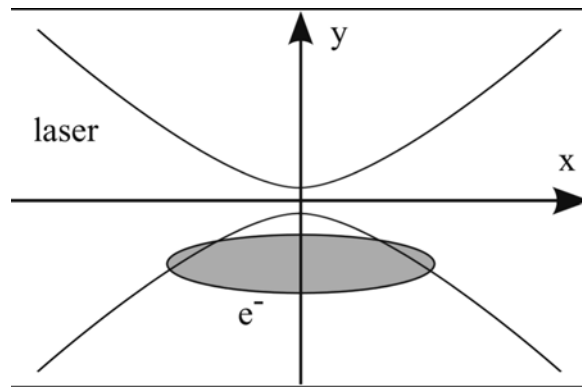
Figure 3: Schematic of laser propagation across a large aspect ratio electron beam.

To accurately deconvolve the laserwire scans using the overlap integral, the laser propagation must be accurately known. The laser propagation was characterised using the M^2 model [8] that describes the laser beam size with reference to the propagation of a laser beam with a Gaussian transverse intensity profile. The transverse laser profile is sampled at various locations throughout the focus region using a laser beam profiler and fitted to Equation 1.

2.5.2.4 *Results*

2.5.2.4.1 Laser Characterisation

The laser propagation was characterised using a larger scale focus created using an $f = 1$ m plano-convex lens. A scaled focus was used as the micrometre size laser focus is beyond the measurement resolution of CCD-based laser beam profilers as well as to avoid contaminating the measurement by the aberrations introduced by strong focussing lenses. Beam profiles of the laser were recorded at various locations throughout the focus and the 4σ diameters used to fit the data to the M^2 model, which was then scaled to the laserwire interaction focus using the measured input beam profile to the laserwire lens. The laser propagation for both axes of the laser beam is shown in Figure 4.
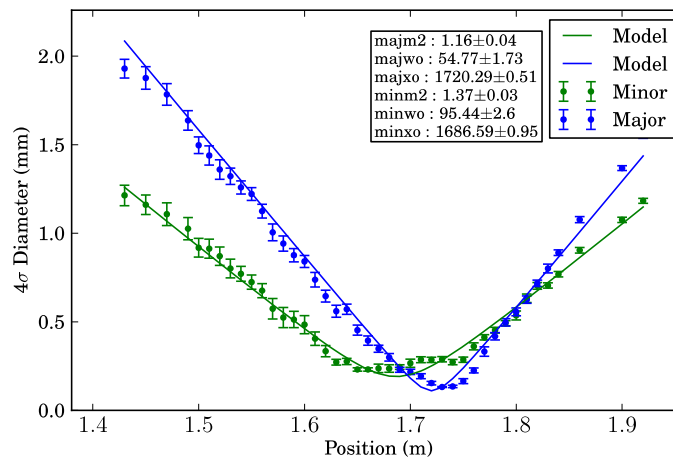
Figure 4: Measured laser propagation in both axes

The laser propagation was found to be astigmatic and the axis of propagation rotated by $17.5 \pm 1.0°$ to the lab frame. The individual propagation models of each axis were used to calculate the projected vertical laser propagation in the lab frame as that is relevant for deconvolving the laserwire scans. The projected size is described by

$$\sigma_l = \sqrt{\left(\sigma_{horizontal} \sin\theta\right)^2 + \left(\sigma_{vertical} \cos\theta\right)^2} \tag{3}$$

2.5.2.4.2 Laserwire Scans

When performing alignment of the laserwire to the electron beam with the OTR screen, a laser machined notch in the edge of the OTR screen was used as it allowed horizontal alignment as well as vertical alignment to be performed. The system was aligned to within $10 \, \mu$m of the optimal vertical position using this method and after this initial alignment, Compton-scattered photons were detectable and the collisions were then optimised to provide the maximum signal.

To achieve an accurate measurement of the electron beam size, the laser focus must be centred on the electron beam, so the laserwire was first coarsely scanned vertically, then horizontally to centre the laser focus before finally performing a detailed vertical scan. The initial coarse vertical scan is shown in Figure 5 with a measured beam size of $2.71 \pm 0.18 \, \mu$m.
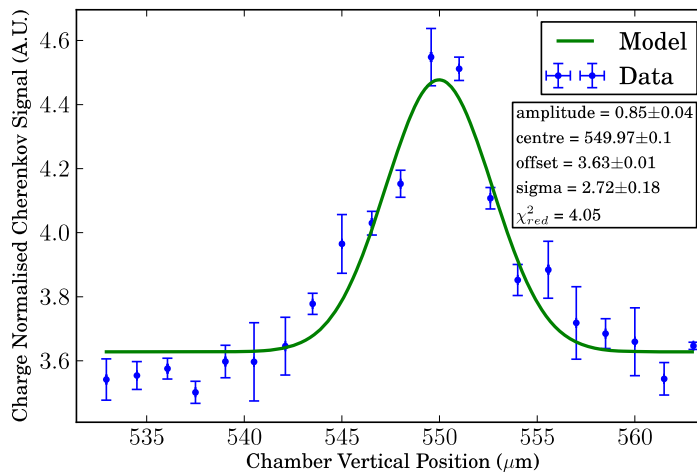
Figure 5: Initial vertical scan of the electron beam.

The initial vertical scan is fitted to a Gaussian function, which although not an accurate description, allows the centre and approximate size to be initially determined. To deconvolve the horizontal scan using the necessary overlap integral model, knowledge of the vertical beam size is need. Similarly, to deconvolve the vertical scan, knowledge of the horizontal is needed. To overcome this circular problem, the two are fitted iteratively together until convergence is reached. The horizontal scan of the electron beam is shown in Figure 6.
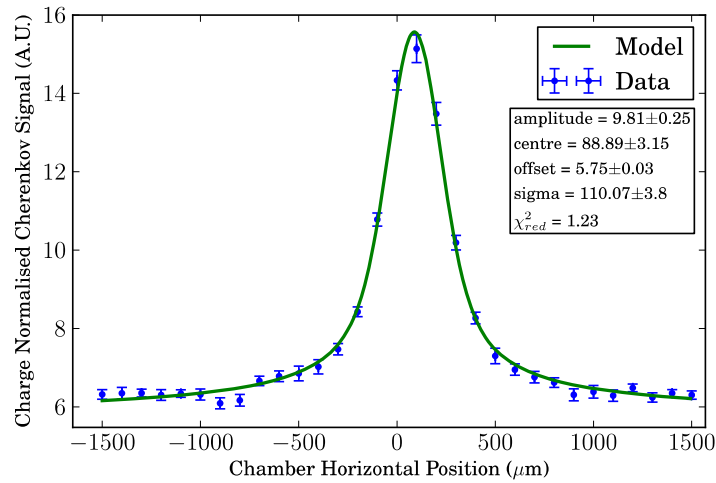
Figure 6: Horizontal scan of the electron beam.

As the divergent laser beam continues to interact with the electron beam even when the laser focus is displaced from the electron beam, the vertical laserwire scans must cover a scan range significantly greater than the vertical size of the electron beam for an accurate measurement. However, the central part of the scan contains a very narrow peak. Therefore, a scan with nonlinear step sizes was crucial in performing accurate laserwire scans as well as minimising the required time per scan. In Figure 7, 61 laser positions were used and 20 machine samples were recorded at each location in the vertical scan.
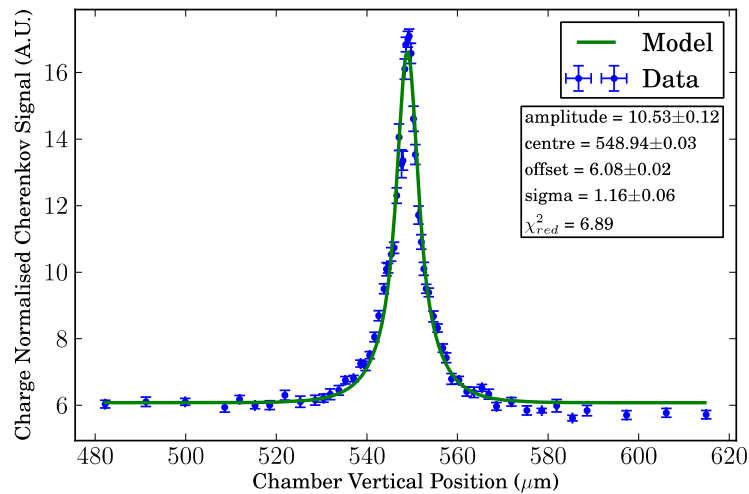
Figure 7: Detailed nonlinear vertical scan of the electron beam.

2.5.2.5   *Conclusions*

Micrometre size electron beam profiles with a resolution of less than $1\,\mu$m have been successfully demonstrated with a visible wavelength laser. The often-cited problem of laser divergence with a laserwire measuring a very large aspect ratio electron beam has been overcome to accurately measure both the horizontal and vertical dimensions.

Precise characterisation of the laser propagation is necessary to deconvolve the non-Gaussian laserwire scans accurately. Furthermore, it has been shown that a laserwire diagnostic with only one laser beam is capable of making a two dimensional profile of the electron beam.

A laserwire diagnostic based on a visible wavelength laser source allows the use of transmissive optics where shorter wavelength lasers would not. Although a shorter wavelength laser allows a smaller focussed spot size to be achieved and therefore a smaller minimum beam size measurement, the necessary use of reflective focussing optics to avoid the absorption of transmissive optics limits the scan range and prevents direct calibration as the focussed laser spot size cannot be measured without interrupting the incoming laser beam. This demonstration of micrometer-size laserwire scans using transmissive optics and a visible wavelength laser will be important in scaling from a single research diagnostic station to a robust multi-station emittance measurement system in a large-scale collider.

The general background level as well as the background encountered due to the horizontal defocussing of the electron beam as a consequence of the necessary strong vertical focussing presents a challenge to successfully operating this laserwire installation. With higher background levels, higher energy laser pulses are required to overcome this as well as a greater number of samples being required to overcome statistical variations. With lower background conditions, a more precise fit to the data could be achieved and future work is under way to develop suitable electron beam optics for this purpose.

The development and demonstration of the laserwire is a significant step forward to achieving a precise and reliable diagnostic for future linear colliders such as the ILC or CLIC. Further to this, there are several considerations for a laserwire system at both CLIC and the ILC for which design studies are underway:

- A more complete simulation of background sources, their transport and effect on detection of the laserwire signal. This is the case for both the low energy scenario at the ATF2 as well as for high energy at a future linear collider.

- With a fuller understanding of background sources and their level, it is possible that the required peak power in the laser pulses could be significantly reduced. If so, this could allow the use of lasers based on optical fibres as well as much more robust and safer transport in optical fibre.

- Reducing the wavelength further to the third harmonic in the soft ultraviolet part of the spectrum. At a wavelength of ~350 nm, the minimum spot size of the laserwire and hence the resolution would be increased as required by CLIC but would still allow the use of transmissive optics.

- A more compact installation using standardised components. To achieve the micrometre-sized focussed spot size, the vacuum window must not introduce optical aberrations. Therefore, it becomes an integrated part of the optical system with the lens placed a precise distance from the window and aligned to optical standards. Because of this constraint, the vacuum chamber with the lense attached must be moved to perform the laserwire scan. Furthermore, with the currently required megawatt to gigawatt peak power levels, damage from back reflections is likely within the lifetime of the diagnostic, in which case an arrangement with an easily replaceable vacuum window is key.

- Integration of an OTR-like screen within the laserwire vacuum chamber as an alignment aid. During the commissioning stages of both the laserwire stations and the accelerator, this will be very important in order to readily achieve collisions between the laser and electron beam.

2.5.2.6 *References*

1. N. Phinney, N. Toge and N. Walker, "International Linear Collider Reference Design Report", Volume 3 (2007).
2. M. Aicheler, P. Burrows, M. Draper, T. Garvey, P. Lebrun, K. Peach and N. Phinney "A Multi-TeV Linear Collider based on CLIC Technology: CLIC Conceptual Design Report" CERN-2012-007.
3. S. T. Boogert *et al.*, Phys. Rev. ST Accel. Beams 13 (12) (2010) 122801.
4. L. J. Nevay *et al.* "Micron-Scale Laser-wire at the ATF-II at KEK Commissioning and Results", IPAC '11, San Sebastian, 2011 TUPC158.
5. Y-I Kim *et al*., Phys. Rev. ST Accel. Beams 15 (4) (2012) 042801.
6. P. Karataev *et al*., Phys. Rev. Lett. 107 (17) (2011) 174801.
7. I. Agapov *et al.*, Phys. Rev. ST Accel. Beams 10 (11) (2007) 112801.
8. T. F. Johnston, Appl. Optics, 38 (21) (1998) 4840.

2.5.3 **Multi OTR System**

Angeles Faus-Golfe, on behalf of the mOTR collaboration
Instituto de Fisica Corpuscular IFIC CSIC-UV, Spain
Mail to: Angeles.Faus-Golfe@uv.es

A multi-Optical Transition Radiation (mOTR) system, consisting of four monitors, is being used routinely since September 2011 for transverse beam size measurement and emittance reconstruction in the extraction (EXT) line of ATF2 (Figure 1). This system has demonstrated to be an excellent diagnostic tool for fast emittance reconstruction, speeding up the beam tuning process in the ATF2 extraction line. A complete description of this system can be found in [1,2,3,4]. The ATF2 OTR results have been several times validated by means of comparisons with Wire-Scanner (WS) measurements, simulations and also with and additional WS wire embedded into the OTR target devices [3].

It is important to mention that the mOTR measurements in the ATF2 EXT line have shown to be reliable and stable, with a resolution of 2 μ m. The best vertical emittance observed in the EXT line during the 2013 running period has been 12 pm at 10^9 electrons per bunch, in agreement with the emittance measured in the Damping Ring.

The mOTR system is being used with good results for cross-plane coupling correction by using four skew quadrupoles to minimise the measured emittance. In addition the mOTR system is also being used for beta matching functions, using quadrupoles in the inflector section, upstream of the mOTR system and to determine the beam energy spread.

Recently a hardware upgrade of the ATF2 mOTR system has been made to avoid wakefields. Due to the compactness of the current design the system has an influence in the increase of the transverse emittance due to wakefield effects [3]. The mechanical structure of the targets and the target holders has been re-designed in order to minimise wakefields. The optical system has been accordingly modified to increase its working distance while preserving the required resolution. The new optical system (with

achromat lens) features a working distance of about 55 mm (the previous working distance was 34 mm) and provides a resolution of 10%. The installation of the optical system and new target holders was made in February 2013.

Although the OTR technique is not new, the complete measurement and correction system of the mOTR system in ATF2 is a significant evolution in the state-of-the art of such solution. Of special note it is the large degree of automation and integration with the online modeling systems.

Similar mOTR system can be deployed at future linear colliders and linac-based synchrotron light sources. For instance, we have studied the feasibility of using mOTR systems in diagnostic sections of the Ring to Main Linac (RTML) of future linear colliders (ILC and CLIC) [5]. mOTR systems can be very suitable for the setup and tuning of the machine in single-bunch or low charge mode operation. This could be very useful during commissioning phases. The key point is the selection of suitable materials to make OTR targets able to survive the impact of the pulses in the RTML environment as well as the optimization of the number and location of the stations [6].
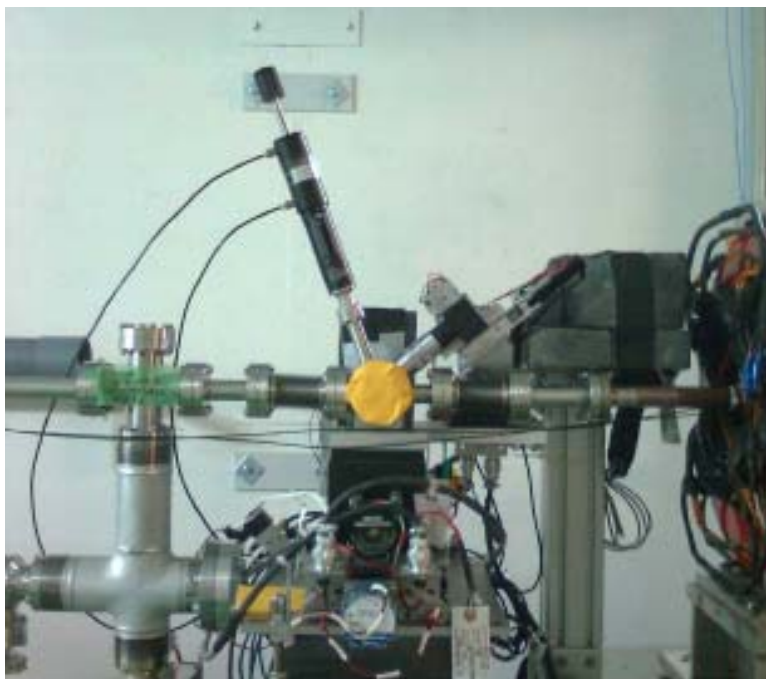
Figure 1: OTR installed in the ATF2 EXT line.

2.5.3.1 *References*

1. J. Alabau-Gonzalvo et al., "Multi Optical Transition Radiation System for ATF2", Proc. of IPAC2010, MOPE050.
2. J. Alabau-Gonzalvo et al.,. "Optical Transition Radiation Optical System for ATF2", Proc. of IPAC2011, TUPC127.
3. J. Alabau-Gonzalvo et al., "Optics and Emittance Studies using ATF2 Multi-OTR System" Proc. of IPAC2012, MOPPR044.
4. A. Faus-Golfe et al., "Upgrade and Systematic Measurement Campaign of the ATF2 muti-OTR System" Proc. of IPAC2013, MOPWO023.

5. J. Resta-Lopez et al., "Multi-OTR System for Future Linear Colliders", Proc. of IPAC2013, MOPME069.
6. A. Faus-Golfe and J. Navarro, "Emittance Reconstruction from measured Beam Sizes", ATF-13-01 report.

3   Workshop and Conference Reports

3.1   ICFA Mini-Workshop on Beam-Beam Effects in Hadron Colliders (BB2013)

Werner Herr for the LHC Beam-Beam Studies Team
CERN, Geneva, Switzerland
Mail to: Werner.Herr@cern.ch

An ICFA Mini-Workshop on Beam-Beam Effects in Hadron Colliders (BB2013) was held March 18th - 22nd at CERN in Geneva, Switzerland. This workshop was a successor and follow up to similar workshops held at CERN in April 1999 and at Fermilab in June 2001 and reviewed the present knowledge and observations on beam-beam effects in hadron colliders. Future research work was discussed with special emphasis on the performance of the LHC after the first long shutdown as well as on studies needed for the planned LHC upgrade projects such as HL-LHC and LHeC.

This workshop was attended by 60 accelerator physicists and consisted of 10 plenary sessions with invited as well as contributed oral presentations. The workshop benefited from a vast amount of beam-beam observations after the successful start of the LHC as well as from the experience from other hadron and lepton colliders.

The workshop was opened with a presentation by Steve Myers, Director for Accelerators and Technology at CERN, with reminiscences of beam-beam observations made at the CERN Intersecting Storage Rings (ISR) 40 years ago. The opening session was concluded by two presentations by the LHC beam-beam team on the observations in the first two years of operation and a comparison with the expectations.

It was followed by reports on the beam-beam experience from other hadron colliders such as the CERN SPS, Tevatron, RHIC and HERA. Topics of growing interest were discussed in a plenary session on experiments in lepton colliders. The experience with crab cavities and novel crossing schemes are highly relevant for the planned luminosity upgrade of the LHC. A full session was dedicated to discuss the existing beam-beam models and tools for beam-beam simulation. New techniques and the available computing power allow a much improved modeling of the beam-beam interaction. The predictive power of both, weak-strong as well as self-consistent strong-strong simulations has reached now a very high level. The simulations are supported by improved analytical models. An important outcome of the discussion was the clear conclusion that beam-beam effects and the interplay with other sources of collective effects such as impedances and electron cloud must be carefully studied and included into the models. The significant contribution to Landau Damping from the non-linear beam-beam interactions was emphasized and will become an important issue in the LHC after the restart.

The highlights of a session on head-on beam-beam interactions were reports on the

very large beam-beam parameters reached in the LHC, twice its nominal value in regular operation, and the interpretation of the observations in the LHC and Tevatron.

Another session was dedicated to discuss parasitic beam-beam interactions. Observations from the LHC and the Tevatron were presented together with the expectations from simulations and models. The complex collision pattern of the LHC leads to strong bunch by bunch differences and these PACMAN effects have been clearly observed as predicted. The analytical and numerical models of these effects have made remarkable progress and the parameter dependence is much better understood and allows reliable predictions for future machines and upgrade scenarios.

A complete session was scheduled to present the studies under way for beam-beam compensation, head-on compensation by means of electron lenses and the compensation of parasitic beam-beam interactions with a wire. Simulation results and the operational experience with beam-beam compensation schemes at Tevatron, RHIC and DAPHNE have been reported. A scheme to minimize the parasitic beam-beam effects in the LHC will be implemented for the restart.

A key topic for a collider is to optimize the physics capabilities of the particle physics experiments. The LHC experiments presented a wish list with their requirements to make optimum use of the luminosity provided by the machine. An unexpected problem occurs in the LHC where the instantaneous luminosity may be too large to be exploited efficiently by the LHC experiments. To avoid loss of efficiency, the luminosity is kept constant during a run by means of luminosity leveling techniques. In two of the experiments this was already done on a regular basis by offsetting the two beams in the transverse plane. The implementation of leveling techniques compatible with the experimental requirements and smooth operation of the LHC is an entirely new aspect of beam-beam studies. Such a mode of operation will be mandatory for the High Luminosity LHC.

The operation of the LHC with two equally strong beams allows observation of strong-strong beam-beam effects, such as coherent modes and non-negligible orbit effects on the beams. The interplay with the machine impedance and possible sources of noise was identified as an important research topic. In this context the need for sufficient diagnostic tools was emphasized and a clear recommendation was given to provide the necessary instrumentation.

In a final session the potential beam-beam issues in future projects such as high luminosity LHC, LHeC and e-RHIC were reviewed and discussed. Additional simulations tools to assess the effect of noise and the use of crab cavities on the beam-beam interactions are needed and being developed.

The outcome of the topical sessions were put together in a summary session at the last day of the workshop. This summary session was chaired by Prof. A. Chao (Stanford University and SLAC). In his personal impressions he mentioned the remarkable progress and large amount of new ideas and concepts developed in recent years.

This short report cannot cover all interesting topics and discussions and the interested readers are encouraged to visit the workshop site at:
https://indico.cern.ch/conferenceDisplay.py?confId=189544

3.2   The Space Charge Workshop 2013 (SC-13)

G. Franchetti (GSI) and F. Schmidt (CERN)
Mail to: g.franchetti@gsi.de, Frank.Schmidt@cern.ch

The Space charge 2013 workshop took place at CERN from April 16thto 19th2013. The scientific program of the workshop has been set up following suggestions by an International advisory committee composed of: Y.Alexahin (FNAL),   O.Boine-Frankenheim (TUD/GSI),   I.Hofmann (GSI/HI-Jena), J.Holmes (SNS), S.Machida (RAL),   E.Metral (CERN),   K.Ohmi (KEK), J.Qiang (LBL) and F.Zimmermann (CERN). The mini workshop was approved by ICFA and sponsored by EUCARD, ACCNET, ICFA, HIC4FAIR and LIU. The program, the presentations and session summaries are available at the indico page:

https://indico.cern.ch/conferenceDisplay.py?confId=221441

There have been 82 registrants distributed over the following countries, laboratories and companies:

Switzerland (CERN) 38
Germany (GSI, Frankfurt University) 13
UK (STFC) 12
USA (Fermilab, SNS, LANL, LBNL, MIT, Tech-X Cor., Muon Inc.) 11
Japan (KEK) 2
Austria (MedAustron) 1
China (IHEP) 1
France (Saclay) 1
Mexico (universidad de sonora) 1
Russia (ITEP) 1
Sweden (ESS) 1

The workshop lasted for 3 and half days and the program has been grouped in the following sessions:

16th of April
Stimulus/Project
Modeling/Theory/Overview
Space Charge Studies

17th of April
Machine model(Theory and Instruments)
Code development

18th of April
High intensity effects
Synergies

19th of April
Mitigation and advanced techniques
Joint Discussion/Outlook.

In each of the3 full days and after the sessions with invited talks there has been 1 hour of contributed talks, followed by another hour for discussions on all the topics being covered during that day. These latter discussion sessions were led by I.Hofmann

(Tuesday 16th), J.Holmes (Wednesday 17th) and E.Metral (Thursday 18th). The joint discussion on Friday 19th was co-convened also by I. Hofmann, J. Holmes and E. Metral.

Summary of the Discussion

It is important to mention that the following scientific secretaries have contributed substantially to this workshop by taking note of all responses to the questions and comments during the discussions:

> H.Bartosik, A.Huschauer, M.Fitterer, V.Forte, J.Wagner, S.Aumon, D.Noll, L.Hein, R.Wasef, C.Hernalsteens, T.Rijoff

The main topics of the workshop have been the following:

1) The workshop as shown a rich activity on space charge related topics at CERN (LIU), GSI (FAIR), and RAL (ISIS upgrade). Several studies have been presented on experimental work and in particular concerning the LIU studies and ISIS upgrade.

2) In the session of code developments, the issue of code benchmarking has found a lot of attention with regards to long-term tracking. The presentation of the status of code benchmarking has been discussed and the issue about the noise created by PIC codes has evoked intense discussions.

   This topic has raised broader interest, in particular by J.Amudson, Eric Stern, J.Holmes, Ji Qiang, and Jean-Luc Vay. The decision has been taken to use the GSI test suite for benchmarking of frozen space charge models also for the benchmarking of PIC codes, both 2.5D and 3D. Firm plans have been made to benchmark Synergia and Orbit and hopefully also IMPACT and WARP.

3) Some discussion has focused on role of GPU in the high intensity beam dynamics. Effort reported by GSI, RAL, FNAL were discussed at a deep technical level, and the present difficulties were highlighted.

4) Interesting from a theoretical standpoint has been a discussion about possibly equating PIC noise with intrabeam-scattering. To this end, previous work by J. Struckmeier has been reviewed on the effect of PIC noise on emittance growth. The audience has expressed the interest to study this topic in some detail.

Discussion/Outlook

The space charge teams at CERN and GSI have had various discussions to set up a list of questions to be addressed by the space charge world community coming to this workshop. This list consists of 7 questions and we have added some responses as a result of the workshop discussions:

DISCUSSION TOPICS

1) What we are really missing at the moment is a better description of our machines WRT to nonlinearities and in particular the variation from magnet to magnet. How can we determine this true non-linear model of the machine and how shall we treat our limited knowledge about it (keywords: sigma of the individual multipolar component, how many seeds). What are the different methods, which can be used to make some progress in this aspect (and time scale)? Which instrumentation do we need to measure "properly" the machine nonlinearities?

What is the meaning of "properly" in a space charge dominated regime that require 10^5 turns of storage time? In particular, the requirements are significantly affected by the physics: there are regimes in which 10% error in the knowledge of nonlinear components is enough for a good description of the machine, but there are other regimes where the concept of "good" or "properly" is difficult to be defined.

Responses:

- What we really need is a better description of the machines; our simulations codes are more or less fine; The question is how we can improve the nonlinear description of our machines? What are the possible methods?
    - linear and nonlinear chromaticity
    - resonance driving terms (correct chromaticity, kick in both planes,)
        - some data in PS, PSB: difficult since only 1 family of sextupoles
    - experience atother labs:
        - chromaticity, DTA
        - ISIS: turn-by-turn
        - octupolar components by local bumps
- There has been a significant amount of work beingdone for the PS in particular. But we still need a reliable magnet by magnet model which would require a more structured effort.

2) For the actual necessity of projects what are the mechanisms for beam loss and emittance growth that are most important => Review of the relevant issue of each project and review of their relevant mechanisms including a comparison with some simple formulae. Do we have good agreement?

Responses:

- There seems to be consensus that resonances due to non-linear fields in conjunction with the tune spread due to space charge seems to lead to both problems: just approaching a resonance leads to emittance blow-up and resonance crossings may lead to losses. On a deeper level the community is split about the questions if these incoherent or also coherent effects are important, as being discussed concerning the half integer resonance crossing in the PSB.

3) Which instrumentation do we need to measure our space charge effects? What has been the progress in instrumentation in the past years and what are the plans for the future?

Responses:

- Concerning instrumentation there has mainly been proposals to provide 1000 turn BPM systems with good resolution and further the developments concerning wire scanners to allow for instance a better resolution of beam halo, i.e. improving existing instrumentation.
- Transverse tomography and collimators to reconstruct the transverse profile have been proposed as possible new tools.
- It was also mentioned that kickers in both planes are important to study coupled resonances.
- There has been a proposal to study coherent effects: A quadrupolar pickup should allow to measure coherent response of the beam to the half integer resonance. In fact, this pickup would allow for the first time the measurement of the real space charge tune spreads in a machine.

4) The numerical aspects of beam physics codes with space charge are very important => In particular when we benchmark codes of either type frozen model or PICtype: which difference is "normal" and which is not.

Responses:

- This issue has been central in the discussion during the workshop.
- On the one hand, benchmarking of several PIC codes have now been pursued and compared with the results of frozen space charge codes. This effort will take the better part of this year.
- On the other hand, renewed interest has been expressed to look into the noise issue of PIC codes in long-term storage ring simulations in more detail by several teams.
- It has been mentioned by PIC code developers that the single particle behavior allows a lot of in-sight into the understanding of the working of PIC codes.

5) There seem to be some beams in the PS with most of the beam below the integer resonance and with not too many losses and emittance growth. Can we explain this?

Responses:

- No clear position from the audience except that the experimental data would have to be well documented to allow for a clarification.

6) What is the maximum space charge tune shift evolution over the past years / decade in the different machines. Did we make progress? Can we dream to reach more than 0.4? What are all the possibilities to push forward the limit? Is the only possibility to fight space charge to increase the injection energy?

7) What can we do from the optics point of view to reduce space charge effects?

Responses:

- Both of the last 2 questions simply would need more studies. In fact, our simulation tools have to be better understood and benchmarked with experiments before a reliable answer can be given.

The final discussion at the workshop has not given definite answers to the list of topics, but has triggered a general consensus that these topics still require further studies. Progress will be presented in the upcoming HB2014workshop or in earlier publications.

3.3   5th **Microbunching Instability Workshop Report**

M. Dohlus[1], J.-H. Han[2], R. Ischebeck[3], K.-J. Kim[4], A. H. Lumpkin[5], S. Di Mitri[6], J. Qiang[7], and J. Wu[8]

[1]Deutsches Elektronen-Synchrotron, Hamburg, Germany
[2]Pohang Accelerator Laboratory, Pohang, Korea
[3]Paul Scherrer Institute, Villigen, Switzerland
[4]Argonne National Laboratory, Argonne, USA
[5] Fermi National Accelerator Laboratory, Batavia, USA
[6]Elettra – Sincrotrone Trieste, Basovizza (TS), Italy
[7]Lawrence Berkeley National Laboratory, Berkeley, USA

[8]SLAC National Accelerator Laboratory, Menro Park, USA

Mail to: J.-H. Han [janghui_han@postech.ac.kr], K.-J. Kim [kwangje@aps.anl.gov]

Introduction

An exceptionally bright electron beam required for present or future X-ray free-electron laser (FEL) facilities suffers from unwanted microbunching instability (μBI). The 5th Microbunching Instability Workshop was hosted by Pohang Accelerator Laboratory on May 8-10, 2013, in POSCO International Center. In this workshop we summarized recent progress on the theories, simulation and experiments on the μBI and discussed how to suppress or even use the instability. Current activities at high brightness beam facilities, where μBI was produced or may take place, were reported. 22 talks were presented in four sessions. Session summaries were presented by the session chairs on the last day. Most of talks are available in the workshop homepage, http://pal.postech.ac.kr/ubi2013/program.jsp.

Overview Session

I.-S. Ko, the director of the PAL-XFEL project, welcomed the participants with briefing the status of the project. He also invited the participants to the PAL-XFEL Groundbreaking Ceremony which the participants subsequently attended on the second day. K.-J. Kim gave opening remark and explained the workshop goal. Overviews on the experiments, theories/simulations and facilities by three experts followed. These overviews provided general introduction and reviewed the recent trend of μBI studies.

Overview and Issues of Experimental Observation of Microbunching Instabilities, A. H. Lumpkin (FNAL)

A. H. Lumpkin overviewed μBI experiments. He started his talk with reviewing the microbunching mechanisms, μBI and its impact to x-ray FELs, and diagnostics for the instability. Then, he showed strong energy modulation observed at LCLS, which could be removed with laser heater. During the last workshop at Maryland, detailed coherent optical transition radiation (COTR) experiment at SCSS (Spring8) was proposed. He showed observations of first COTR at SCSS and strong COTR at SACLA. The COTR spectrum measured at SACLA, which provided an evidence of the microbunching, was shown also. Experimental results from APS using both rf thermionic cathode (TC) and rf photocathode (PC) guns were reported. He showed μBI observations at FLASH, Pegasus/UCLA, BNL, and NLCTA/SLAC, and he concluded that COTR, caused by μBI, appeared regardless of the type of gun and linac. He also showed LSC instability amplifier tests at NLCTA and future test plan at the Advanced Superconducting Test Accelerator (ASTA) facility. He pointed out that μBI observation should be done in infrared, where the gain is strong, and longitudinal details with adequate resolution of time and energy would be required.

Overview of Theory and Simulation of Microbunching Instability, R. Li (Jefferson Lab)

R. Li overviewed the theories and simulations of μBI. She reviewed the mechanism of μBI development and the important factors for the instability. She introduced the 1D μBI, induced by coherent synchrotron radiation (CSR) and longitudinal space charge

(LSC), to explain the microbunching gain and laser heater effect at LCLS. She described the 3D space charge effects on the µBI. Trickled heating at the LCLS laser heater was explained with the 3D effect. The IMPACT code was shown to be capable of high resolution simulation; however challenges remain for fully self-consistent simulation at short wavelength. She then explained the CSR theory and simulation in further detail and concludes both longitudinal and transverse CSR force are needed for understanding the beam dynamics with CSR interaction.

Overview on Facilities. Theory and Experiment of Suppressing Microbunching Instailibty with a Magnetic Chicane at FERMI@Elettra, S. Di Mitri (Elettra – Sincrotrone Trieste)

S. Di Mitri overviewed µBI researches at various facilities. He first reviewed COTR experiments at NLCTA, JLAB, FLASH and SACLA, which cover large ranges of bunch charge and beam energy. Then he introduced laser heater experiments at LCLS and FERMI@Elettra. He explained the phase mixing idea for the control of microbunching gain, by sending a beam though the second bunch compressor without energy chirp. The theory, simulation and experiment of the phase mixing at FERMI@Elettra followed. Finally, he showed the laser heater setup and recent experiments at FERMI@Elettra.

Summary of Theory and Simulations Session I & II

The contributions can be grouped into contributions about the **modeling of effects** (1d/3d space charge effects by J. Wu and transient CSR effects by C. Mitchell), about **noise suppression** (reversible heating by C. Behrens, global longitudinal dispersion by J. Qiang and de-amplification of microbunching by G. Stupakov) and **different applications** (ion cooling by D. Ratner and SC amplifier by S. Weathersby).

Transverse Granularity Effects on Microbunching, J. Wu (SLAC)

This talk discusses the question if space charge effects can be computed in one dimension (weak dependency of longitudinal E-field vs. transverse cross section) or if 3D simulations are required, and it investigates if transverse granularity can drive longitudinal instabilities. Two asymptotic limits are distinguished: in the low frequency limit, if the transverse correlation length is small compared to gamma times the wavelength of longitudinal modulation (lambda), the effect is purely longitudinal. The high frequency limit is reached, if the transverse beam size is large compared to gamma times lambda/(2*pi). In this regime the effect is purely transverse and can be computed by the continuity equation. Some examples for transverse granularities are given, from round Gaussian distributions, round smooth shapes as bagel and donut to rectangular raster of different sizes. For Cartesian raster profiles the transverse field profile is compared with the transverse distribution and the response from one cell. The coupling from transverse granularity to longitudinal slice energy spread is numerically investigated for a Cartesian raster profile and the LCLS laser heater. A slight increase of energy fluctuations is observed in comparison to smooth transverse distribution. It is proposed to calculate the longitudinal impedance of arbitrary distributions (of azimuthal order 'monopole') as function of the radial coordinate by convolution of the general radial distribution with the analytic solution for a ring-charge. Even though analytical

closed form is presented for monopole mode only, the approach is applicable for azimuthal dependent case as well.

Reversible Electron Beam Heating for Suppression of Microbunching Instability, C. Behrens (SLAC)

Microbunching instabilities in bunch compression systems of FELs can be handled by a controlled increase of the slice energy spread with a laser heater. This degradation of phase space density can be avoided by a reversible heater scheme with two transverse deflecting structures (TDS) before and after the bunch compressor. The first TDS couples longitudinal and vertical phase spaces: therefore vertical beam size causes additional slice energy spread and longitudinal size increases vertical divergence. The slice energy spread is converted by longitudinal dispersion into a spread of length. The original slice (before the compressor) is longitudinally smeared and leads to an exponential damping term in the gain equation. The second TDS is used to eliminate the coupling from longitudinal position to divergence. The scheme needs two conditions: the phase advance between the TDS is a multiple of pi, and the transverse deflections are related by the compression factor, the energies and beta functions at the TDSs.

The basics of transverse deflections have been presented and the concept of reversible heating was simulated for a practical example close to the NGLS (LBNL) design. The most critical jitter sources arise from energy jitter upstream of the bunch compressor chicane and from rf phase jitter in the TDSs. Linear accelerators based on superconducting rf technology are preferred to fulfill these requirements (in multi-bunch operation with intra-bunch feedbacks). The reversible beam heater system exhibits integrated options for diagnosis and on-line monitoring of the longitudinal phase space. Proof-of-principle experiments at FERMI in Trieste and ASTA at FNAL are proposed and simulations are started.

Effects of Transient CSR Wakefields on Microbunching in a Bunch Compressor, C. Mitchell (LBNL)

The amplification of microbunching is calculated for a bunch compressor chicane using the integral equation method. This method makes use of a 1D longitudinal impedance to describe the collective effects within the beam, and it implicitly assumes that the longitudinal electric self-field within a slice is independent of the transverse offset. This impedance is calculated from the CSR model described by D. Sagan, and space charge forces are excluded. In previous investigations, a steady-state impedance has been used to compute the microbunching gain. The steady-state model assumes that there is no interaction on straight lines and that the interaction on arcs is approximated by ultra-relativistic circular motion. Here, the CSR wake-function depends on the position of the bunch within the lattice and includes transient effects resulting from bend-drift transitions. It is demonstrated that the transient wakefield depends significantly on the position of the bunch within the lattice, and the transient impedance is strongly affected by oscillations around the steady state solution, which can produce strong enhancement of the CSR electric field at some wavelengths. The period of these oscillations decreases with the distance from the transition. Calculations of the microbunching gain using several models are then compared: 1) the steady-state model, 2) a model including bend-entry transients, 3) a model including both bend-entry and bend-exit transients (the Saldin model), 4) a model including CSR from the nearest upstream bends, and 5) a model including CSR from all upstream bends. For the second

bunch compressor of NGLS it is found that the steady state model underestimates the gain (g ≈ 3) by about 17%. This increase is essentially caused by the CSR that is present in the drifts due to bend-exit transients.

Cooling Hadrons with the Microbunching Instability, D. Ratner (SLAC)

The problems of hadron cooling are addressed together with the disadvantages of earlier proposals. A new scheme is proposed that uses the μBI from LSC. In this cooling scheme, a hadron's Coulomb field produces the initial energy modulation. A dispersive region then converts the energy modulation from each hadron into a single density spike and each spike adjusts the energy of its corresponding hadron in a kicker. Microbunched electron cooling offers two benefits: first, the electron cooling creates only a single spike of large bandwidth for each hadron (in contrast to periodic spices with FEL amplification). Second, the scheme is relatively simple, consisting of drift and dispersive regions. For the modulator process two extremes are discussed: the modulator is long or short compared to the betatron period. In the first case, transverse motion is considered by approximating particles as discs. In the other extreme, electrons rings of high density appear after the dispersive section. The case of long interaction seems to be feasible and is considered. According to a fluid model (without shot noise) one ion creates a current spike of about 0.1 A and 1 nm length in a 100 A electron beam. Shot noise simulations, by particle tracking, with periodic boundary conditions, indicate that the noise per turn is much larger than the effect from the modulation. The shot noise cancels for many revolutions, supposing the gain process remains in the linear regime. To reduce the effect of timing jitter in the amplifier, the total R_{56} should be zero.

An Alternative Method to Suppress the Microbunching Instability in FEL Linacs, J. Qiang (LBNL)

As yet another approach to suppress μBI, J. Qiang et al. proposed to sandwich linac+chicane system between two dipoles. Rather than using slice energy spread to suppress the microbunching via the R_{56} transport matrix element, the authors proposed to use the transverse beam emittance including the dispersive part. They explicitly showed that in a dipole, the transverse smearing can be stronger than the longitudinal smearing. The dispersion is closed by the second dipole after the linac+chicane system. The scheme is proven to be effective via an illustrative example aiming for the NGLS (LBNL) project. To prove the robustness of such a scheme, they studied effects from machine jitter: energy jitter before the first dipole and the second dipole as well as the transverse mismatch between the two dipoles.

Noise Suppression – Can It Help Us with Seeding FELs? G. Stupakov (SLAC)

G. Stupakov first reviewed his former work with D. Ratner on using a chicane to suppress space charge induced microbunching gain. The theory is extended for de-amplification of microbunching with a general wake function instead of the space charge interaction. Requirement on the impedance for optimal suppression is formulated. It is found that the noise can be either reduced or increased depending on the wake function (mostly related to the imaginary part of the impedance) and the R_{56}. The extended theory shows that for a beam with finite energy spread, only partial noise suppression can be achieved. After recognizing the importance of the imaginary part of

the impedance, the speaker posted the question: "What structures can have imaginary impedance (at short wavelength) larger than the space charge?" An answer is proposed, i.e., to use an optical klystron setup with two undulators. With this setup, a numerical example was given to show the effectiveness of such a scheme. It seems that the practically achievable levels of suppression for realistic beam energy spread do not go below ~ 0.1. While the density noise suppression is an important research topic, the energy noise on the SASE FEL startup is also studied and is pointed out to be important.

Generation of Broadband Coherent Photon Pulses with a Cascaded Longitudinal Space-Charge Amplifier, S. Weathersby (SLAC)

Microbunching suppression is the main theme of this workshop, yet there are a few talks about using microbunching in a positive way. This talk is one of those. The micro-bunched electron beam can be used to generate broadband radiation source (e.g., attosecond pulses) in a short undulator. Such a scheme was proposed before in DESY, and was named a longitudinal space-charge amplifier (LSCA). The talk reported the experimental demonstration of a LSCA at NLCTA ECHO beamline at SLAC. The three chicanes in any ECHO scheme can largely amplify the space-charge induced micro-bunching; hence can be turned into a cascaded LSCA. The experiment obtained strong radiation in optical/NIR wavelengths regime, realized single transverse mode and single spectral mode through strong current compression. The experiment demonstrated high-gain (~ 4 orders of magnitude above shot-noise). The cascaded gain through three chicane stages was measured for different partition of a fixed total R_{56}. The experiment measurement agreed with the theoretical prediction and therefore ruled out alternative explanations for the experimentally observed coherent emission.

Summary of Experiments Session I and II

This summary by A.H. Lumpkin (I) and R. Ischebeck (II) concerns experimental results presented in the two sessions at the workshop. In Session I these included aspects of bunch communication modes in rings by R. Warnock; beam imaging principles and coherent optical transition radiation (COTR) mitigation concepts by R. Ischebeck; and the results of PAL-XFEL injector tests by M. Chae. Session II included talks on cancellation of CSR kicks by S. Di Mitri and observations of CSR in an EEX beamline by J. C. T. Thangaraj. We also provide a list of experiments under consideration as collected from talks across the workshop and discussion sessions.

CSR in Whispering Gallery Modes, R. Warnock (SLAC)

R. Warnock introduced the concept of CSR in whispering gallery modes and resonances in storage ring beams. He showed striking agreement between experiments and theory. The resonant modes result in a series of sharp spikes in the CSR spectrum and wakefields that allow interbunch communication such as shown at ANKA and the Canadian Light Source. The amount of charge in the preceding bunch appears to impact the radiation levels from the following bunch. Higher charge in the preceding bunch results in enhanced emission from the following bunch. He presented the theory of modes in a toroidal vacuum chamber as generally found in rings. Data from the BESSY ring in Berlin and the NSLS-VUV ring at Brookhaven support the models. He also discussed aspects of vacuum chamber geometry and how this may be applicable in

single pass systems such as bunch compressors in linacs for x-ray FELs. This appears to be an area for possible future experiments.

A Transverse Profile Imager for Swiss FEL, R. Ischebeck (PSI)

The PSI injector test facility includes the S-band PC rf gun, S-band accelerators, and a series of beam diagnostics stations. R. Ischebeck described detailed aspects of viewing angles for scintillator crystals and the fundamental aspects of using the Scheimpflug principle by tilting the sensor plane to mitigate depth-of-focus aspects with converter screens at 45 degrees. He also reported normalized slice emittance measurements at the very low 80-nm or 0.08-micron level for beam charges of 1.5 pC. These notably low values are needed for the PSI-proposed XFEL project SwissFEL. After a brief review of the complications of COTR in OTR images observed at LCLS, APS, and FLASH/DESY, he described optical configurations using off-axis mirrors at back angles that permit the mitigation of such potential µBI-related COTR by collecting scintillator light at angles outside of the COTR cone angles. The station is also designed with an option to insert an OTR screen at a shallow angle to be imaged by the same optical system and lens as used for the scintillator. The configuration limits depth-of-focus issues related to using OTR screens at 45 degrees to the beam direction. A prototype station is under construction and will be tested when available.

PAL-XFEL Injector Test Facility, M. Chae (PAL)

The PAL-XFEL injector test facility (ITF) includes the S-band PC rf gun, S-band acceleration capability to 139 MeV, and initial diagnostics stations. Typical micropulse charge is 200 pC. There is a low energy spectrometer after the gun, and a high energy spectrometer at the end of the accelerator beamline. M. Chae reported normalized emittance measurements at the sub-1-mm-mrad level based on the quadrupole field scan technique and the tracking of the downstream beam size at an imaging station. The imaging station used a YAG:Ce crystal with its surface normal to the beam direction and a 45 degree mirror to direct the light into the optical transport to the digital CCD camera. Plans to test a laser heater in anticipation of the need to limit the µBI in the XFEL linac (see J-H Han's talk) and to install an rf deflector cavity and a wire scanner to augment their diagnostics capabilities were also described.

Cancellation of CSR Kicks with Optics Balance, S. Di Mitri (Elettra)

CSR in bunch compression schemes has an effect on the transverse distribution of the beams by kicking the beam transversely. This can be seen by an increase in projected emittance in the plane of the deflection. The present work by S. Di Mitri et al. demonstrates that CSR kicks in a multi-bend beam line can be compensated. Theoretical studies as well as an experimental demonstration have been performed, and good agreement has been found. The theoretical studies take into account a simplified 1D model, with steady state emission of synchrotron radiation. It is assumed that the transverse kick in each slice is coherent, such that the slice emittance is not affected. However, different slices feel different kicks. Their displacement in the transverse phase space increases the projected emittance. A simple approach consists of making the beta function small in the magnet where this occurs, in particular in the last magnet of a bunch compressor. In a multi-bend beam line, this is not practical. Thus, an approach where the CSR kicks in the magnets cancel each other has been presented. It consists of

a phase advance of π between identical magnets, and identical beam parameters at the corresponding points. This scheme is used in many transfer line designs. However, the optics symmetry puts stringent requirements on the lattice design. Additional constraints in general require more magnets and more space.

A new approach for a beam transport line is presented. It achieves a horizontal displacement of the beam, energy collimation and optics matching for the subsequent undulator line. The design consists of four dipole magnets, with a phase advance of π in the intermediary drift spaces. But in this case, optics symmetry is replaced by a proper balance of the asymmetric Twiss functions along the lattice. Since the bunch length is constant in this transfer line, the CSR kicks can be made to cancel, and the projected emittance of the beam is preserved. To demonstrate the practical feasibility of this concept, a measurement performed at FERMI is presented. The quadrupole magnet in the middle of the transfer line, which defines the phase advance between the first and the second half, was varied, and the projected horizontal emittance was measured. The increase in emittance was found to be indeed minimum for a phase advance of π, and the measured emittance growth for other phase advances agrees well with the predictions from the 1D model.

Experimental Studies on an Emittance Exchange Beamline at the A0 Photoinjector, J. C. T. Thangaraj (FNAL)

J. C. T. Thangaraj reported studies of the CSR phenomena at the A0 photoinjector at Fermilab. 6D beam emittances generated at state-of-the-art photoinjectors are asymmetric in longitudinal and transverse coordinates. An emittance exchange system such as the beamline installed in the A0 photoinjector allows to swap transverse with longitudinal properties of the beam. In addition to exchanging emittances, a transverse beam shaping can also be transformed into a longitudinal profile. In addition, it has been shown that this method can also be used to suppress microbunching instabilities. He presented experimental studies on an emittance exchange beamline at the A0 photoinjector. A method to characterize the bunch length is CSR that is emitted in the dipole magnet of the dogleg. The CSR power was recorded as a function of rf phase, and this method allowed to optimize the compression. A twin pulse, generated by two spatially separated parts on the cathode, was observed in time domain on a streak camera. An optimized performance of the emittance exchanger was achieved by chirping the electron beam. This minimizes the thick lens effect, allowing for a shorter bunch as witnessed by coherent synchrotron radiation. Possibilities for future emittance exchange systems were presented, consisting of dogleg and chicane style systems. A "flipper" emittance exchanger, making use of a double-chicane system, would allow to compress the bunch at the same time. The deflecting cavity could also be used for diagnostics when the emittance exchange is switched off. Finally, a system consisting of a reversible beam heater plus emittance exchange was presented.

Future Experiments to Consider

We provide a list of experimental investigations that are being considered in the next year or so that might be candidates for updates at the next μBI workshop. These are based on talks throughout the workshop and were presented at the Experiment Summary closeout. These are provided in the context of the successful COTR experiments at SCSS and SACLA reported this. These clearly address the fact of the

µBI's presence in DC TC gun beams under multiple compressions. Further experiments on rf TC gun and rf PC gun beams are encouraged.

Experiments under consideration

- PSI to demonstrate new COTR mitigation configuration with common optics focus for OTR and scintillator.
- Diagnostics COTR mitigation options include:
    - Spectral differences between OTR and COTR can be used to sort photons. (APS/ANL-FNAL)
    - Scintillators can be used to enhance S/B ratio in combination with a bandpass filter. (APS/ANL-FNAL)
    - Temporal gating can sort prompt COTR and delayed scintillator light, both MCP gate and CCD shutter options. (DESY, ANL, and FNAL examples)
    - Angular distributions of COTR and IOTR are displaced in some cases.
    - Specific COTR angles can be spatially filtered versus 4π scintillator light. (DESY and SACLA)
- Continue investigations on APS/ANL linac with TC rf gun beam. COTR data to compare to previous PC rf gun beam on basically same linac. Optimize compressions and then continue tests with new PC gun.
- Pursue reversible heater technique experimentally at FERMI@Elettra and/or ASTA. (longer term)
- Continue longitudinal space charge amplifier (LSCA) experiments: NLCTA and Shanghai? Use existing EEHG configurations that enable the cascaded compressions.
- Perform time resolved COTR test: rf deflector and OTR screen; FLASH, SACLA, NLCTA. How is COTR localized longitudinally?
- Test J. Qiang's µBI-mitigation concept with paired dipoles around linac-chicane. Where?
- Continue µBI studies with laser heater at LCLS as described by Zhou.
- Test Laser heater at PAL-XFEL ITF.
- Evaluate feasibility of experiments related to CSR wakes on second bunch in ASTA chicane vacuum chamber, extend from Warnock's study in rings. Also might be considered at ANL AWA.
- Investigate µBI suppression with EEX at ASTA/FNAL
- Look for µBI at high charge per micropulse at ASTA/FNAL. (long term)
- Note: Need simulation support and guidance in most cases.

Missing experiments

- Source of microbunching: particle distribution on the cathode
    - Thermionic gun
    - Laser gun
        - Comparison of different longitudinal laser profiles
        - Comparison of YAG and Ti:Sa laser
- Slicing techniques:
    - Comparison of measurement methods
        - deflector (t)

- skew quadrupole in dispersive section (E)
- scraper (E)
  - CSR effect on slice emittance measurement

Summary of Facilities Session I & II

This summary concerns electron beam dynamics studies carried on for three linac-driven x-ray free electron laser (FEL) facilities currently under advanced design study: European XFEL, NGLS, SXFEL, LCLS, SACLA & SCSS, PAL-XFEL, and ASTA/FNAL. The aforementioned studies are, as expected, relevant to the modeling of development and suppression of the microbunching instability along the accelerator.

Microbunching Instability Studies at European XFEL, M. Dohlus (DESY)

The machine working point is intended to be the ensemble of electron beam and accelerator parameters (charge, bunch duration, energy, number and strength of the magnetic compressors, linac rf setting, linac sensitivities and so on) that define the transport, time-compression and acceleration of the electron beam until it reaches the undulator. A semi-analytical method has been presented that describes how the working point can be determined while optimizing the final electron beam quality for the FEL process. Special attention is given to the flatness of the final current profile and of the longitudinal phase space, in the presence of nonlinear optics transport elements and collective effects such CSR emission in the bends of the magnetic compressors and linac geometric wakefields.

Optimization of the working point depends on the beam heating process at low energy in that the increase of uncorrelated energy spread may have an impact on the final bunch current shaping through magnetic compression and on the final longitudinal phase space. Beam heating is foreseen to be achieved with a laser heater at 130 MeV. Its impact on the suppression of μBI is shown to be determinant. Detailed numerical simulations show that a final slice energy spread rms of 2.0 MeV can be reached with important suppression of the instability that is with smoothed current and energy distribution. The laser heater system is located before the first magnetic compressor. The beam is thus energy chirped at that location, which is cause of an asymmetric transverse beam profile at the undulator location. This asymmetry may suggest an inefficient beam heating while using nowadays standard beam and external laser overlap conditions in the undulator. To overcome the asymmetry issue, a laser beam vertically displaced respect to the electron beam is considered. It is shown that the electron energy distribution after the undulator resembles a Gaussian more than for the case of two beams overlapping along their longitudinal axis. Such a pseudo-Gaussian energy distribution ensures almost uniform heating along the bunch, if uniform slice beam optics is assumed. In reality, this is not the case but identical considerations hold for perfectly aligned beams, so optics non-uniformity is not an issue strictly dependent on the overlap criterion. The proposed heating scheme shows, in addition, two advantages respect to standard beams overlapping: it is insensitive to a large extent to horizontal displacement of different bunch slices due to energy chirp and gives more freedom with beam optics manipulation. Finally, it is shown that the planned laser heater layout allows reduced trickle heating respect to the LCLS case due to proper arrangement of the laser heater chicane and electron beam parameters.

Simulation and Analysis of Microbunching Instability at NGLS Beam Delivery System, J. Qiang (LBNL)

The NGLS facility plans to implement velocity bunching at very low energy, two magnetic chicanes, usable for one-stage or two-stage compression scheme, and a laser heater right after the injector. To overlap the laser and electron beam in the undulator and obtain an efficient heating level, the electron beam size is shrunk inside the undulator, thus increasing the charge density. This is predicted to enhance short-range space charge forces that disrupt the beam optics laminarity approximation. As a result, the electron beam is mismatched with respect to the no-space charge computation of its transport. To recover the design matching and keep the beam optics well under control, some quadrupole magnets have to be retuned around the laser heater system.

µBI starting form shot noise out of the injector is predicted to develop along the entire line with a gain of the order of 1000 and peaked around 30 µm uncompressed wavelength, in the linear analytical approximation and high gain regime. This case refers to the two chicane case, which is worst in terms of gain development with respect to the one-stage at low energy. Both current and energy profiles are finally strongly modulated, unless beam heating at the level of 15 keV or 10 keV are adopted, for the two-stage and one-stage compression, respectively. As a result, the final minimum slice energy spread is predicted to be around 150 keV and the peak gain is shown to be suppressed by at least one order of magnitude. IMPACT-Z was used to sample the final energy spread-induced energy spread curve, showing a nonlinear behavior for low heating, which is due to the instability growing rate, a point of minimum and then a linear behavior at larger heating due to the preservation of the beam longitudinal emittance during compression. The curve is in agreement with analytical expectations. The one-stage compression, as mentioned, is expected to relax the heating external laser power requirement and allow smoothing of the final longitudinal phase space, as in the two-stage scheme. However, a second compressor is maintained in the layout for flexibility in the compression scheme, presumably for reaching higher peak currents than in the baseline design. A tolerance study was carried out on the initial density modulations to be suppressed with the aforementioned heating level. It is found that current modulations shorter than 2 ps and smaller than 5% in amplitude out of the injector can be kept well under control.

Microbunching Instability Study for Proposed Shanghai Soft X-ray FEL Facility, D. Huang (SINAP)

Analytical evaluation of the µBI gain was done in the high gain, linear approximation. The computation of the instability gain was based on numerical results from ELEGANT tracking code, although this was limited in the number of particles for memory and CPU time restrictions. The gain shows to be strongly dependent on the amount of initial uncorrelated energy spread that is used as an input, when the instability is thought to be started from charge shot noise. As a matter of fact, a smoothed initial particle distribution reveals a much lower local energy spread than that not smoothed one, so suppressing the gain. In spite of that, the FFT of the current distribution out of the first compressor shows similar frequency pattern with the inclusion of a broad spectrum. There are some indications of nonlinear harmonics generation during the instability development, which is a case not treated in the analytical model to date. It was also found that, by turning on the laser heater chicane,

but with no heating active yet, an increased energy modulation, especially at the shortest wavelength is observable for the final beam. The physical meaning of the chicane impact on the μBI is in the author's future plan of study.

Recent LCLS Injector Improvements for Operation, F. Zhou (SLAC)

F. Zhou reported improving photocathode quantum efficiency (QE) by using laser cleaning technology. The QE for the newly installed cathode is about 5x10-6 before any cleaning process. Upon the laser cleaning, the QE was improved by a factor of 8-10. The QE further increases by another factor of 3 in the first 6 months following the laser cleaning, and then stays at 1.1x10-4 from the sixth month till now for two years. The transverse emittance was recovered after a few weeks' operation. He then reported the improvement of the transverse emittance by using a truncated Gaussian spatial laser profile instead of the nominal transverse uniform spatial distribution. This also saves 2-3 times of laser power required from the laser amplifier. He then reported development of the slice emittance measurements at LCLS BC1 and BC2 using collimators with a wire scanner. Those measurements also show that the LCLS slice emittances are preserved from injector, through BC1 and BC2 with 150 pC charge. Finally, he reported about the laser heater operation experience at the LCLS. The COTR effects were observed at OTR2 with laser heater chicane only (no heating). This makes the previous measured LCLS injector emittance underestimated by 30-50%. Also the impact of the laser profile on the final FEL radiation intensity was studied. However, those effects are not stable and a definite conclusion cannot be drawn. One issue is that the laser profiles/position/size cannot be constantly maintained. Identifying the microbunching sources is being planned at the LCLS in the next few weeks.

Coherent OTR Phenomena at the SACLA and the SCSS Test Accelerator, K. Togawa (RIKEN)

K. Togawa reported studies of the COTR phenomena at SACLA and at the SCSS test accelerator. At SACLA, no COTR was observed after BC1 at 30 - 400 MeV with 60 A peak current. No COTR or sometimes weak COTR was observed after BC2 at 0.4 - 1.4 GeV with 600 A current. Strong COTR was observed after BC3 at 1.4 GeV with 3 kA current. The COTR signal can be suppressed with longitudinal mixing by tuning a quadrupole inside the bunch compressor chicane. He also reported the COTR generation experiments at the SCSS test accelerator by using parameter scan. The COTR signal can be generated in a special bunching condition. During the C-band phase scan, the COTR was generated at the phase around -10 degrees. By shifting the phase of 476 MHz booster cavity in the injector, bunch compression in the velocity compression region was strengthened. The COTR did not appear at any C-band phase. By shifting the S-band phase to the crest, the bunch length after the bunch compressor was extended. The C-band phase at which the COTR was generated shifted to the bunching side. In the beam energy dependence study, the COTR was generated beyond 230 MeV at the fixed C-band phase (-10 degrees).

Microbunching Instability Study at PAL-XFEL, J.-H. Han (PAL)

J.-H. Han reported the μBI studies at the PAL-XFEL. The μBI was studied for two photoinjector designs: one based on the side coupling, the other based on the coaxial coupling at front. Without using laser heater, both designs show the strong final phase

space filamentation at 10 GeV due to the µBI with 200 pC charge. For the first nominal design, a 10 keV uncorrelated energy spread from the laser heater helps suppress the µBI. For the second design, a 9 keV uncorrelated energy spread is needed. The nominal design has about a compression factor of 150 through three magnetic chicanes. An initial short bunch at the injector (4 ps instead of 8 ps) was tested to lower the requirement for the compression factor (75 instead of 150) in order to reach the same final current. It turns out that using such a shorter initial does not reduce the effect of the µBI. One still needs to use ~13 keV rms energy spread from the laser heater to avoid the final phase space filamentation.

Mitigation Plans for the Microbunching-Instability-Related COTR at ASTA/FNAL, A. H. Lumpkin (FNAL)

A. Lumpkin reported mitigation plans for the µBI related COTR diagnostics at the ASTA facility. The facility construction and operation will occur in stages. They anticipated that the µBI will occur after the second bunch compressor with a high bunch charge up to 5 to 10 nC. He suggested some diagnostics needed for the µBI study. Those diagnostics include beam bunch length monitors for tuning compression by using CTR, CSR, CER, CDR, streak camera, rf deflector; OTR beam profile screens for COTR imaging for spatial structure, intensity fluctuations, enhancement diagnostics; Optical spectrometers, FIR spectrometers (may add if see COTR); Deflecting mode cavities or streak cameras with fs resolution to see longitudinal structure directly; and energy spectrometer with high resolution to see modulation. He also suggested diagnostic options for COTR mitigation. Those include using spectral differences between OTR and COTR to sort photons; Using scintillators to enhance S/B ratio in combination with a bandpass filter; using temporal gating to sort the prompt COTR and the delayed scintillator light with both MCP gate and CCD shutter options. Making use of angular distributions of the COTR and the IOTR displacement in some cases as proposed by R. Fiorito at the 2008 µBI workshop, Using the specific COTR angle to spatially filter the COTR signal versus 4π scintillator light. He also showed a test example to mitigate the COTR signal by reducing the COTR effects with 400x40 nm BPF and with more sensitive camera than 40 dB analog to see the remaining OTR profile.

4 Recent Doctorial Theses

4.1 Parametric-Resonance Ionization Cooling for Muon Beams in the Twin Helix Channel

James A. Maloney
Mail to: physics_maloney@yahoo.com

Graduation Date: May 10, 2013
Institution: Northern Illinois University, Dekalb, IL, USA
Supervisor: Professor Bela Erdelyi

Abstract:

Muon colliders have been proposed for the next generation of particle accelerators that study high-energy physics at the energy and intensity frontiers. This dissertation examines muon cooling techniques, a critical aspect to the feasibility of these proposed machines. Muon cooling reduces the emittance of muon beams, a measurement of the phase space volume of the beam. Reducing emittance improves the luminosity and physics reach of these machines. Ionization cooling, the basic method for reducing muon beam emittance, is detailed, as well as various cooling channel proposals implementing this method. One particular implementation of ionization cooling is parametric-resonance ionization cooling (PIC). PIC is proposed as the final 6D cooling stage of a high-luminosity muon collider. It can also be used for final cooling in a muon-based Higgs factory. Adding the cooling methods of PIC offers the potential to reduce emittance beyond that achievable with ionization cooling alone. PIC theory is detailed and implemented in a magnetic channel based on the superposition of two helical dipole magnetic harmonics identical in gradient, period, and phase but with opposite helicities. This channel, known as the twin helix, is simulated so that the effects of PIC can be demonstrated.

4.2 Emittance and Energy Diagnostics for Electron Beams with Large Momentum Spread

Maja Olvegård
Mail to: maja.olvegard@physics.uu.se

Graduation Date: May 24, 2013
Institution: Uppsala U., Dept of Phys. & Astro., Box 516, SE-751 20 Uppsala, Sweden
Supervisors: Prof. Volker Ziemann, Uppsala U.
Dr. Thibaut Lefevre, CERN
Dr. Enrico Bravin, CERN

Abstract:

In the Compact Linear Collider, CLIC, the high intensity drive beam will lose 90% of its initial kinetic energy in special structures from which power is extracted and transferred to the main beam acceleration. When the drive beam is decelerated the beam quality deteriorates and the momentum spread increases, which makes the beam transport challenging. Dedicated diagnostics to monitor the momentum profile along each bunch train and transverse profile diagnostics will be needed. The beam quality in the decelerator will be investigated in the test beam line, TBL, at the CLIC Test Facility, CTF3, at CERN, where several power extraction structures reduce the drive beam energy by up to 55%. We report on the design and performance of a segmented beam dump for time-resolved measurements of the momentum profile in TBL. In the view of the large momentum spread, we report on performance studies of optical transition radiation screens, used for transverse and momentum profile diagnostics. As the momentum spread increases, the validity of standard diagnostics methods, such as spectrometry or emittance measurement through quadrupole scans, is lost. We have studied the systematic errors that arise and developed novel algorithms to correctly analyze these measurements for arbitrary momentum distributions. Finally, we provide an outlook towards equivalent beam profile monitors in the CLIC decelerator.

5   Forthcoming Beam Dynamics Events

5.1   The 8th International Accelerator School for Linear colliders

The application process for attending *The Eighth International Accelerator School for Linear Colliders* has begun. (http://www.linearcollider.org/school/2013/) The school will take place from December 4 to 15, at Hotel Rixos Downtown, Antalya, Turkey, and be hosted by the Institute of Accelerator Technologies (IAT) of Ankara University. Each applicant should complete the online registration form (which can be found on the school web site) and submit a curriculum vita as well as a letter of recommendation from his/her supervisor (in electronic form, either PDF or MS WORD). The number of students is limited. Accepted students will receive partial or full scholarship for attending the school including travel. There is no registration fee. The application deadline is September 10, 2013.

This school will provide a 11-day program including 8-1/2 days of lectures, an excursion and a final examination. The first three days will be an introductory course with an overview of future lepton colliders (ILC, CLIC and other advanced colliders) as well as introductions to linac basics and instrumentation basics. This will be followed by two elective courses, one on accelerator physics (electron and positron sources, linacs, damping rings, ring colliders and beam delivery systems) and the other on accelerator technology (room temperature RF, superconducting RF, beam instrumentation, LLRF and high power RF) to run in parallel for 6 days. Each student is required to take the introductory course and one of the two electives. There will be homework assignments and a final examination but no university credits.

The school program and a list of lecturers are listed below.

<u>Lecturers of the 2013 LC Accelerator School</u>

Topic	Lecture	Lecturer
Introduction	I1	Kaoru Yokoya (KEK)
ILC	I2	Kaoru Yokoya (KEK)
CLIC	I3	Frank Tecker (CERN)
Linac basics	AB1	Daniel Schulte (CERN)
Instrumentation basics	AB2	Hermann Schmickler (CERN)
Linac	A1	Daniel Schulte (CERN)
Sources	A2	Masao Kuriki (Hiroshima U.)
Damping rings	A3a	Yannis Papaphillipou (CERN)
Ring colliders	A3b	Yannis Papaphillipou (CERN)
Beam delivery & beam-beam	A4	Andrei Seryi (John Adams Inst.)
Room temperature RF	B1	Walter Wuensch (CERN)
Superconducting RF	B2	Takayuki Saeki (KEK)
Instrumentation	B3	Hermann Schmickler (CERN)
LLRF & high power RF	B4	Stefan Simrock (ITER)

Eighth International Accelerator School for Linear Colliders – Curriculum (v.2, 8/13/2013)

December 4 – 15, 2013, Rixos Hotel, Antalya, Turkey

Hosted by the Institute of Accelerator Technologies (IAT) of Ankara University

Daily Schedule

Breakfast	07:30 – 09:00
Morning	09:00 – 12:30, including ½-hour break
Lunch	12:30 – 14:00
Afternoon	14:00 – 17:30, including ½-hour break
Dinner	18:00 – 19:00
Tutorial & homework	19:00 – 22:00

List of Courses (black: required, red and blue: elective)

	Morning	Afternoon	Evening
December 4		Arrival, registration	Reception
December 5	Introduction to physics & future accelerators	ILC	Tutorial & homework
December 6	CLIC	Joint lecture: Linac basics	Tutorial & homework
December 7	Joint lecture: Instrumentation basics	Course A: Accelerator physics / Course B: Accelerator technology	Tutorial & homework
December 8	Course A: Accelerator physics / Course B: Accelerator technology	Excursion	Tutorial & homework
December 9	Course A: Accelerator physics / Course B: Accelerator technology	Course A: Accelerator physics / Course B: Accelerator technology	Tutorial & homework
December 10	Course A: Accelerator physics / Course B: Accelerator technology	Course A: Accelerator physics / Course B: Accelerator technology	Tutorial & homework
December 11	Course A: Accelerator physics / Course B: Accelerator technology	Excursion	Tutorial & homework
December 12	Course A: Accelerator physics / Course B: Accelerator technology	Course A: Accelerator physics / Course B: Accelerator technology	Tutorial & homework
December 13	Course A: Accelerator physics / Course B: Accelerator technology	Course A: Accelerator physics / Course B: Accelerator technology	Tutorial & homework
December 14	Course A: Accelerator physics / Course B: Accelerator technology	Study time	Study time
December 15	Final exam	Free time	Banquet; Student Award Ceremony
December 16	Departure		

Program

	Thursday, December 5	Friday, December 6	Saturday, December 7	Sunday, December 8
Morning 09:00 – 12:30	**Inauguration** Welcome – *O Yavas (IAT)* Introduction – *W Chou (Fermilab)* **Lecture I1 – Introduction** (3 hrs) *Kaoru Yokoya (KEK)* • Tera scale physics • Overview of future accelerators for Tera scale physics (ILC, CLIC, muon collider, γγ collider, LHeC, TLEP, new acceleration technologies)	**Lecture I3 – CLIC** (3 hrs) *Frank Tecker (CERN)* • Klystron vs. beam driven acceleration • CLIC layout • Parameter choices & optimization • Driver beam stability • Comparison of the CLIC and ILC • Technical challenges	**Joint lecture AB2 –** Instrumentation basics (3 hrs) *Hermann Schmickler (CERN)*	**Course A: Accelerator physics** Lecture A1 – Linac (cont'd) *Daniel Schulte (CERN)* **Course B: Accelerator technology** Lecture B1 – Room temperature RF (cont'd) *Walter Wuensch (CERN)*
Afternoon 14:00 – 1730	**Lecture I2 – ILC** (3 hrs) *Kaoru Yokoya (KEK)* • e- and e+ sources • Bunch compressors and spin rotators • Damping rings • Main linac • Beam delivery system • Civil construction issues	**Joint lecture AB1 – Linac basics** (3 hrs) *Daniel Schulte (CERN)*	**Course A: Accelerator physics** Lecture A1 – Linac (9 hrs) *Daniel Schulte (CERN)* **Course B: Accelerator technology** Lecture B1 – Room temperature RF (12 hrs) *Walter Wuensch (CERN)*	Excursion
Evening 19:00 – 22:00	Tutorial & homework	Tutorial & homework	Tutorial & homework	Tutorial & homework

Program (cont'd)

	Monday, December 9	Tuesday, December 10	Wednesday, December 11	Thursday, December 12
Morning 09:00 – 12:30	**Course A: Accelerator physics Lecture A1 – Linac (cont'd)** *Daniel Schulte (CERN)* **Course B: Accelerator technology Lecture B1 – Room temperature RF (cont'd)** *Walter Wuensch (CERN)*	**Course A: Accelerator physics Lecture A3a – Damping rings (12 hrs)** *Yannis Papaphillipou (CERN)* **Course B: Accelerator technology Lecture B1 – Room temperature RF (cont'd)** *Walter Wuensch (CERN)*	**Course A: Accelerator physics Lecture A3a – Damping rings (cont'd)** *Yannis Papaphillipou (CERN)* **Course B: Accelerator technology Lecture B2 – Superconducting RF (cont'd)** *Takayuki Saeki (KEK)*	**Course A: Accelerator physics Lecture A3a – Damping rings (cont'd)** *Yannis Papaphillipou (CERN)* **Course B: Accelerator technology Lecture B2 – Superconducting RF (cont'd)** *Takayuki Saeki (KEK)*
Afternoon 14:00 – 17:30	**Course A: Accelerator physics Lecture A2 – Sources (6 hrs)** *Masao Kuriki (Hiroshima Univ.)* **Course B: Accelerator technology Lecture B2 – Superconducting RF (12 hrs)** *Takayuki Saeki (KEK)*	**Course A: Accelerator physics Lecture A2 – Sources (cont'd)** *Masao Kuriki (Hiroshima Univ.)* **Course B: Accelerator technology Lecture B2 – Superconducting RF (cont'd)** *Takayuki Saeki (KEK)*	**Excursion**	**Course A: Accelerator physics Lecture A3a – Damping rings (cont'd)** *Yannis Papaphillipou (CERN)* **Course B: Accelerator technology Lecture B3 – Instrumentation (3 hrs)** *Hermann Schmickler (CERN)*
Evening 19:00 – 22:00	Tutorial & homework	Tutorial & homework	Tutorial & homework	Tutorial & homework

	Friday, December 13	Saturday, December 14	Sunday, December 15	Monday, December 16
Morning 09:00 – 12:30	**Course A: Accelerator physics Lecture A3b – Ring colliders (3 hrs)** *Yannis Papaphillipou (CERN)* **Course B: Accelerator technology Lecture B4 – LLRF & high power RF (9 hrs)** *Stefan Simrock (ITER)*	**Course A: Accelerator physics Lecture A4 – Beam delivery system and beam-beam (cont'd)** *Andrei Seryi (John Adams Inst.)* **Course B: Accelerator technology Lecture B4 – LLRF & high power RF (cont'd)** *Stefan Simrock (ITER)*	08:00 – 12:30 Final exam (4.5 hrs)	Departure
Afternoon 14:00 – 17:30	**Course A: Accelerator physics Lecture A4 – Beam delivery system and beam-beam (6 hrs)** *Andrei Seryi (John Adams Inst.)* **Course B: Accelerator technology Lecture B4 – LLRF & high power RF (cont'd)** *Stefan Simrock (ITER)*	Study time	*Free time*	
Evening 19:00 – 22:00	Tutorial & homework	Study time	Banquet at 19:00; Student Award Ceremony	

Notes on the Program:

1. There are a total of 11 school days in this year's program, excluding the arrival day (December 4) and the departure day (December 16). The time is divided as follows: 2-1/2 days for required courses, 6 days for elective courses, two 1/2 day for excursions, 1/2 day for study time and a final examination day.
2. The required course consists of five lectures: introduction, ILC, CLIC, linac basics and instrumentation basics. Every student must take this course.
3. There are two elective courses: Course A (the red course) is accelerator physics, Course B (the blue course) is accelerator technology. They will run in parallel. Each student will choose one of these.
4. The accelerator physics course consists of lectures on four topics: (1) linac, (2) sources, (3) damping rings and ring colliders, and (4) beam delivery system and beam-beam effects.
5. The accelerator technology course also consists of lectures on four topics: (1) room temperature RF, (2) superconducting RF, (3) instrumentation, and (4) LLRF and high power RF.
6. There will be homework assignments, but homework is not counted in the grade. There will be a final examination. Some of the exam problems will be taken from variations of the homework assignments. The exam papers will be graded immediately after the exam and results announced in the evening of December 15 at the student award ceremony.
7. There is a tutorial and homework period every evening. It is part of the curriculum and students are required to attend. Lecturers will be available in the evening of their lecture day during this period.
8. Lecturers have been asked to cover the basics as well as possible. Their teaching material will be made available online to the students ahead of time (a few weeks prior to the school). Students are strongly encouraged to study this material prior to the beginning of the school.
9. Lecturers of the elective courses are required to provide lecture syllabus as soon as possible in order to help students make their selection.
10. All lecturers are responsible for the design of homework and exam problems as well as the answer sheet. They are also responsible for grading the exams.
11. The award ceremony will honor the top (~10) students based on their exam scores.

5.2   The 3rd Low Emittance Ring Workshop

Under the auspices of the EuCARD2 project, we are happy to announce the third Low emittance ring workshop to be held in Oxford in July 8th-10th 2013, hosted by the John Adams Institute for Accelerator Science.

The workshop brings together different accelerator communities working on the design of ultra low emittance lattices such as synchrotron light sources, damping rings and test facilities for linear colliders and HEP circular colliders. The aim of the workshop is to review the present development s in design of ultra low emittance lattices, the experience and the challenges with the operation of low emittance synchrotrons and the main technological problems. The merging of different accelerator communities is expected to foster ideas exchange and the collaboration both on theoretical, experimental and design issues. Areas for common R&D programmes will

be explored. The workshop will profit from the experience of colleagues who have designed, commissioned and operated lepton ring colliders and synchrotron light sources as well as from the ones involved in future low emittance upgrade programmes of existing rings.

The Workshop sessions will include:

Low emittance lattice design and tuning
> Algorithms and optimisation tools
> Nonlinear beam dynamics
> Novel injection schemes
> Beam based tuning techniques and model calibration
> Beam loss management and Top-Up operation

Collective effects
> Intrabeam scattering
> Electron cloud
> Machine impedance effects and minimisation
> Coherent synchrotron radiation

Low emittance ring technology
> IDs and magnets
> Kickers
> Diagnostics and instrumentation
> Vacuum
> Engineering integration

Suggestions for presentations should be sent to one of the organisers:
Riccardo Bartolini, JAI and Diamond Light Source (r.bartolini1@physics.ox.ac.uk)
Susanna Guiducci, INFN (susanna.guiducci@lnf.infn.it)
Yannis Papaphilippou, CERN (ioannis.papaphilippou@cern.ch)

5.3   The 2013 International Workshop on FFAG Accelerators

The 2013 International Workshop on FFAG Accelerators will be held September 21-24 at the TRIUMF Laboratory on the campus of the University of British Columbia. Accommodation has been reserved at the TRIUMF guest house nearby.

The Workshop will follow immediately after the 20th International Conference on Cyclotrons and their Applications (Cyclotrons'13), which is to be held in downtown Vancouver September 16-20. Information about the conference can be found at its Web site: http://cyc13.triumf.ca/

Three invited papers on FFAGs are included in the conference schedule, and contributed papers on FFAGs are also encouraged. Please note the following Cyclotron Conference deadlines:

Abstract submission	May 6
Early registration fee	July 15
Conference hotel reservation	August 15

The Conference Web site has a page with basic information about the Workshop at:
http://cyc13.triumf.ca/FFAG13.html ,

This will be replaced by a dedicated FFAG'13 Workshop Web site with registration and room booking details by the end of April.

Hoping you will be able to join us in the latest of what has become an interesting and productive series of workshops,

Mike Craddock
Chairman FFAG'13

5.4 The 2nd International Beam Instrumentation Conference (IBIC2013)

On behalf of the Organising Committees I would like to welcome you to the 2nd International Beam Instrumentation Conference IBIC2013, to be held in Oxford, UK, 16-19 September 2013. Like its predecessors, BIW and DIPAC, this conference is dedicated to exploring the physics and engineering challenges of beam diagnostics and measurement techniques for charged particle accelerators. IBIC2013 is being hosted by Diamond Light Source, the UK's national synchrotron light facility.

The 3.5 day scientific program will include 11 invited and 21 contributed talks, a public lecture and 3 poster sessions. Following that there will be the opportunity to visit one of Diamond Light Source, ISIS or the Central Laser Facility all at Rutherford Appleton Labs

The conference web site is http://www.ibic2013.org and contains all the necessary information on abstract submission and registration, paper preparation as well as travel and accommodation.

Abstract submission is now open on the following topics:
   * Overview and Commissioning
   * BPMs and Beam Stability
   * Time Resolved Diagnostics and Synchronization
   * Beam Loss Detection
   * Beam Profile Monitors
   * Beam Charge Monitors and General Diagnostics
   * Collider Specific Instrumentation

The conference dinner will be held at the historic Oxford Town Hall and is included in the registration fee as are lunches and refreshments.

PLEASE PLAN TO ATTEND - REGISTRATION IS NOW OPEN

We hope that you enjoy the conference, and find it intellectually stimulating. If there is anything we can do to make your conference experience and stay in Oxford more enjoyable, just ask us at ibic2013@diamond.ac.uk .

Guenther Rehm
Chair of the IBIC2013 Programme Committee

5.5   2013 North American Particle Accelerator Conference

We are delighted to announce the 2013 North American Particle Accelerator Conference, to take place from September 30 to October 4 at the Pasadena Convention Center, Pasadena, California. NA-PAC'13 will bring together scientists, engineers, students, and industrial exhibitors, representing all aspects of accelerators and particle beams, for an information-sharing experience focused on technology.

The local organizers for NA-PAC'13 are Lawrence Berkeley National Laboratory, SLAC National Accelerator Laboratory, and the University of California, Los Angeles. The conference is jointly sponsored by the IEEE Nuclear and Plasma Sciences Society and the APS Division of Physics of Beams. The local organizers are also developing a social program that we hope will match the intellectual rewards of the conference, and will offer some suggestions on what you might wish to explore on your own. Pasadena has a great deal to offer, especially in arts and culture; and within day-trip or evening-out range are all the world-famous attractions of greater Los Angeles, from Hollywood to the theme parks.

The Scientific Program Committee (SPC), is chaired by Alex Chao, SLAC National Accelerator Laboratory. An exciting programme of invited oral presentations has been developed and is now published at the conference website, now on line here:

http://www.napac13.lbl.gov

together with much useful information. Please bookmark the site and check regularly for updates.

A special student poster session will take place during delegate registration on Sunday, September 29. Students are encouraged to find out more about the student grant programme, and to apply to present their work in this special session.

An industrial exhibition will take place during the first three days of the conference. Booth reservation for exhibitors, on a first come first served basis, will be possible from *Wednesday, April 10, 2013 at 10:00, PDT (Pacific Daylight Time)* via JACoW's Scientific Programme Management System (SPMS) at

http://appora.fnal.gov/pls/pac13/profile.html

Prospective participants should take careful note of the deadlines for registration and reservation of accommodation, and in particular for abstract submission on *Wednesday, May 29, 2013 at midnight, PDT (Pacific Daylight Time)* again via JACoW's Scientific Programme Management System (SPMS) at

http://appora.fnal.gov/pls/pac13/profile.html

Guidelines on preparation and submission of abstracts are provided at the conference website under Author Information. Delegate registration will open in the coming months. Please register before *Wednesday, July 26, 2013* to take advantage of early (reduced) registration fees.

Proposals for hotel accommodation will shortly be published at our website. Proceedings will be published at the JACoW site

http://www.jacow.org

shortly after the conference.

We look forward to your joining us in Pasadena for an enjoyable and rewarding week of exploring how accelerator technology and science can be pushed forward in every way.

Steve Gourlay, Lawrence Berkeley National Laboratory
NA-PAC'13 Organizing Committee Chair

Alex Chao, SLAC National Accelerator Laboratory
NA-PAC'13 Scientific Program Coordination Committee Chair

Chan Joshi, University of California, Los Angeles
NA-PAC'13 Local Organizing Committee Chair

5.6 ICFA Mini-Workshop on Commissioning of SuperKEKB and e^+e^- Colliders.

SuperKEKB will be the first high-energy electron-positron collider designed to work with ultra-low emittance beams ("nanobeams") when coming online in 2015/2016. Once fully commissioned, SuperKEKB will be by far the highest-luminosity collider. Beam commissioning of this machine is expected to be challenging but also extremely interesting. The beam dynamics issues to be tackled will range from optics issues, like maintaining a large beam aspect ratio, to collective effects of all kinds, e-cloud and possibly newer effects not yet well understood. Due to its design features, SuperKEKB shares a lot of features with low-emittance light sources presently in operation or under design. At the same time, SuperKEKB will be a test bed for larger circular colliders like the TLEP collider presently under study at CERN and other laboratories.

To encourage involvement of a broad spectrum of accelerator scientists we are planning a workshop, tentatively set for Nov. 11 to 13 at KEK, to bring together the world community of accelerator physicists reviewing the challenges expected at SuperKEKB and other e^+e^- colliders. Issues on the injector linac, sources, and damping rings will be discussed also. The goal is to identify possible responses to these challenges, exchange information with those who have met similar challenges before, and outline where new machine designs will be able to profit from the SuperKEKB experience. The workshop will be open to all interested and be all plenary sessions with ample time for discussion.

Workshop organizers:
Y. Funakoshi, K. Oide, KEK, Y. Cai, U. Wienands, SLAC

A registration website will be setup shortly.

For details please contact:
    K. Oide (Katsunobu.Oide@kek.jp)
    U. Wienands (uli@slac.stanford.edu)

6   Announcements of the Beam Dynamics Panel

6.1 ICFA Beam Dynamics Newsletter

6.1.1 Aim of the Newsletter

The ICFA Beam Dynamics Newsletter is intended as a channel for describing unsolved problems and highlighting important ongoing works, and not as a substitute for journal articles and conference proceedings that usually describe completed work. It is published by the ICFA Beam Dynamics Panel, one of whose missions is to encourage international collaboration in beam dynamics.

Normally it is published every April, August and December. The deadlines are 15 March, 15 July and 15 November, respectively.

6.1.2 Categories of Articles

The categories of articles in the newsletter are the following:
1. Announcements from the panel.
2. Reports of beam dynamics activity of a group.
3. Reports on workshops, meetings and other events related to beam dynamics.
4. Announcements of future beam dynamics-related international workshops and meetings.
5. Those who want to use newsletter to announce their workshops are welcome to do so. Articles should typically fit within half a page and include descriptions of the subject, date, place, Web site and other contact information.
6. Review of beam dynamics problems: This is a place to bring attention to unsolved problems and should not be used to report completed work. Clear and short highlights on the problem are encouraged.
7. Letters to the editor: a forum open to everyone. Anybody can express his/her opinion on the beam dynamics and related activities, by sending it to one of the editors. The editors reserve the right to reject contributions they judge to be inappropriate, although they have rarely had cause to do so.

The editors may request an article following a recommendation by panel members. However anyone who wishes to submit an article is strongly encouraged to contact any Beam Dynamics Panel member before starting to write.

6.1.3 How to Prepare a Manuscript

Before starting to write, authors should download the template in Microsoft Word format from the Beam Dynamics Panel web site:

http://www-bd.fnal.gov/icfabd/news.html

It will be much easier to guarantee acceptance of the article if the template is used and the instructions included in it are respected. The template and instructions are expected to evolve with time so please make sure always to use the latest versions.

The final Microsoft Word file should be sent to one of the editors, preferably the issue editor, by email.

The editors regret that LaTeX files can no longer be accepted: a majority of contributors now prefer Word and we simply do not have the resources to make the conversions that would be needed. Contributions received in LaTeX will now be returned to the authors for re-formatting.

In cases where an article is composed entirely of straightforward prose (no equations, figures, tables, special symbols, etc.) contributions received in the form of plain text files may be accepted at the discretion of the issue editor.

Each article should include the title, authors' names, affiliations and e-mail addresses.

6.1.4 **Distribution**

A complete archive of issues of this newsletter from 1995 to the latest issue is available at

http://icfa-usa.jlab.org/archive/newsletter.shtml.

This is now intended as the primary method of distribution of the newsletter.

Readers are encouraged to sign-up for electronic mailing list to ensure that they will hear immediately when a new issue is published.

The Panel's Web site provides access to the Newsletters, information about future and past workshops, and other information useful to accelerator physicists. There are links to pages of information of local interest for each of the three ICFA areas.

Printed copies of the ICFA Beam Dynamics Newsletters are also distributed (generally some time after the Web edition appears) through the following distributors:

Weiren Chou	chou@fnal.gov	North and South Americas
Rainer Wanzenberg	rainer.wanzenberg@desy.de	Europe[++] and Africa
Toshiyuki Okugi	toshiyuki.okugi@kek.jp	Asia[**]and Pacific

[++] Including former Soviet Union.

[**] For Mainland China, Jiu-Qing Wang (wangjq@mail.ihep.ac.cn) takes care of the distribution with Ms. Su Ping, Secretariat of PASC, P.O. Box 918, Beijing 100039, China.

To keep costs down (remember that the Panel has no budget of its own) readers are encouraged to use the Web as much as possible. In particular, if you receive a paper copy that you no longer require, please inform the appropriate distributor.

6.1.5 **Regular Correspondents**

The Beam Dynamics Newsletter particularly encourages contributions from smaller institutions and countries where the accelerator physics community is small. Since it is impossible for the editors and panel members to survey all beam dynamics activity worldwide, we have some Regular Correspondents. They are expected to find interesting activities and appropriate persons to report them and/or report them by themselves. We hope that we will have a "compact and complete" list covering all over the world eventually. The present Regular Correspondents are as follows:

Liu Lin	Liu@ns.lnls.br	LNLS Brazil
Sameen Ahmed Khan	Rohelakan@yahoo.com	SCOT, Oman
Jacob Rodnizki	Jacob.Rodnizki@gmail.com	Soreq NRC, Israel
Rohan Dowd	Rohan.Dowd@synchrotron.org.au	Australian Synchrotron

We are calling for more volunteers as Regular Correspondents.

6.2   ICFA Beam Dynamics Panel Members

Name	eMail	Institution
Rick Baartman	baartman@lin12.triumf.ca	TRIUMF, 4004 Wesbrook Mall, Vancouver, BC, V6T 2A3, Canada
Marica Biagini	marica.biagini@lnf.infn.it	LNF-INFN, Via E. Fermi 40, C.P. 13, Frascati, Italy
John Byrd	jmbyrd@lbl.gov	Center for Beam Physics, LBL, 1 Cyclotron Road, Berkeley, CA 94720-8211, U.S.A.
Yunhai Cai	yunhai@slac.stanford.edu	SLAC, 2575 Sand Hill Road, MS 26 Menlo Park, CA 94025, U.S.A.
Swapan Chattopadhyay	swapan@cockroft.ac.uk	The Cockcroft Institute, Daresbury, Warrington WA4 4AD, U.K.
Weiren Chou (Chair)	chou@fnal.gov	Fermilab, MS 220, P.O. Box 500, Batavia, IL 60510, U.S.A.
Wolfram Fischer	wfischer@bnl.gov	Brookhaven National Laboratory, Bldg. 911B, Upton, NY 11973, U.S.A.
Yoshihiro Funakoshi	yoshihiro.funakoshi@kek.jp	KEK, 1-1 Oho, Tsukuba-shi, Ibaraki-ken, 305-0801, Japan
Jie Gao	gaoj@ihep.ac.cn	Institute for High Energy Physics, P.O. Box 918, Beijing 100039, China
Ajay Ghodke	ghodke@cat.ernet.in	RRCAT, ADL Bldg. Indore, Madhya Pradesh, 452 013, India
Ingo Hofmann	i.hofmann@gsi.de	High Current Beam Physics, GSI Darmstadt, Planckstr. 1, 64291 Darmstadt, Germany
Sergei Ivanov	sergey.ivanov@ihep.ru	Institute for High Energy Physics, Protvino, Moscow Region, 142281 Russia
In Soo Ko	isko@postech.ac.kr	Pohang Accelerator Lab, San 31, Hyoja-Dong, Pohang 790-784, South Korea
Elias Metral	elias.metral@cern.ch	CERN, CH-1211, Geneva 23, Switzerland
Yoshiharu Mori	mori@rri.kyoto-u.ac.jp	Research Reactor Inst., Kyoto Univ. Kumatori, Osaka, 590-0494, Japan
George Neil	neil@jlab.org	TJNAF, 12000 Jefferson Ave., Suite 21, Newport News, VA 23606, U.S.A.
Toshiyuki Okugi	toshiyuki.okugi@kek.jp	KEK, 1-1 Oho, Tsukuba-shi, Ibaraki-ken, 305-0801, Japan
Mark Palmer	mark.palmer@cornell.edu	Wilson Laboratory, Cornell University, Ithaca, NY 14853-8001, USA
Chris Prior	chris.prior@stfc.ac.uk	ASTeC Intense Beams Group, STFC RAL, Chilton, Didcot, Oxon OX11 0QX, U.K.
Yuri Shatunov	Yu.M.Shatunov@inp.nsk.su	Acad. Lavrentiev, Prospect 11, 630090 Novosibirsk, Russia
Jiu-Qing Wang	wangjq@ihep.ac.cn	Institute for High Energy Physics, P.O. Box 918, 9-1, Beijing 100039, China
Rainer Wanzenberg	rainer.wanzenberg@desy.de	DESY, Notkestrasse 85, 22603 Hamburg, Germany

The views expressed in this newsletter do not necessarily coincide with those of the editors.
The individual authors are responsible for their text.